

Dissertation  
submitted to the  
Combined Faculty of Natural Sciences and Mathematics  
of the Ruperto Carola University Heidelberg, Germany  
for the degree of  
Doctor of Natural Sciences

Presented by  
M.Sc. Carina Beatrice Vibe  
born in: Oslo, Norway.  
Oral examination: 27.03.2020



The temperature response of the medaka  
segmentation clock and its link to robustness in  
embryonic patterning

Referees:  
Prof. Dr. Detlev Arendt  
Prof. Dr. Joachim Wittbrodt



<b>Acknowledgements</b>	9
<b>Summary</b>	11
<b>Zusammenfassung</b>	13
<b>1. Introduction</b>	15
<b>1.1 Phenotypic robustness in developing systems</b>	15
1.1.1 Robust patterning upon variation in size	15
1.1.2 Robust patterning during variation in temperature	16
<b>1.2 Medaka as a model to study robust patterning</b>	18
<b>1.3 Somitogenesis as a model to study robust patterning</b>	20
1.3.1 Somitogenesis patterns vertebrate embryos	20
1.3.2 Mesp regulates somite anterior-posterior identity	21
1.3.3 The role of signaling oscillations in the segmentation clock	22
1.3.4 The dynamics of Notch signaling oscillations	22
1.3.5 The Hes/her family are at the core of Notch signaling oscillations in vertebrates	22
1.3.6 A network of her protein heterodimers regulate oscillatory behaviour in zebrafish and medaka PSM	23
1.3.7 Hes/her transcription factors oscillate by a negative-feedback mechanism	25
1.3.8 Gradients in the PSM regulate the differentiation front	26
1.3.9 Wnt and FGF signaling oscillations in mouse and chick PSM	28
<b>1.4 Live imaging of segmentation clock oscillations</b>	29
1.4.1 Destabilized gene activity reporters	29
1.4.2 Fusion protein reporters	30
<b>1.5 The functional importance of oscillation dynamics</b>	31
1.5.1 The slope of the phase gradient is predictive of segment size during scaling	32
1.5.2 The relative phase-shift between two oscillating pathways can carry positional information	32
<b>2. Aims of the study</b>	35
<b>3. Results - Part I: Establishing medaka as a model to study signaling dynamics</b>	37
<b>3.1 Generation of a medaka Her7 segmentation clock reporter using CRISPR/Cas9</b>	38
3.1.1 Validation of the Her7-Venus line	40
3.1.2 Generation of a her7 knockout line	42
3.1.3 Characterisation of the her7 knockout phenotype at the molecular level	46
3.1.4 Characterisation of her7 expression dynamics in the Her7-Venus line	49
3.1.5 Removal of the integrated donor backbone in the Her7-Venus line	53
<b>3.2 Generation of medaka Wnt and FGF signaling reporters using CRISPR/Cas9</b>	56
3.2.1 Generation of Ctnnb1-Venus and Axin2.1-Venus knock-in lines	56
3.2.2 Generation of a Snai1a-Venus knock-in line	59
<b>4. Results - Part II: Exploring mechanisms of temperature compensation</b>	62

<b>4.1 Quantification of medaka segmentation clock dynamics at 27°C</b>	62
4.1.1 Time-lapse imaging of Her7-Venus oscillations in medaka	62
4.1.2 Quantification of segmentation clock dynamics	65
4.1.3 Comparative analysis of oscillation dynamics in the Her7-Venus1 and Her7-Venus2 lines	67
4.1.5 Quantification of the period and phase gradients in the PSM	68
<b>4.2 Quantification of medaka segmentation clock dynamics between 23-37°C</b>	71
4.2.1 Defining the range of temperature-compensated patterning in medaka	71
4.2.2 Exploring Her7-Venus oscillation dynamics between 23-37°C	73
4.2.3 Quantification of posterior oscillation period between 23-37°C	74
4.2.4 Quantification of period gradient between 23-37°C	75
4.2.5 Quantification of phase gradient between 23-37°C	78
<b>5. Discussion</b>	81
<b>5.1 Exploring mechanisms of robustness during patterning and morphogenesis in medaka</b>	81
5.1.1 Medaka can develop normally across a wide temperature range	81
5.1.2 Defining the criteria for temperature-compensated segment formation	83
5.1.3 The segmentation clock is not temperature-compensated	84
5.1.4 The period gradient changes with temperature	85
5.1.5 What is the functional relevance of a period gradient in the PSM?	86
5.1.6 The phase gradient is temperature-compensated	87
5.1.7 Challenging existing models of somitogenesis to explain temperature-compensated patterning	88
The alpha model	88
The clock and wavefront model	89
5.1.8 Is relative-phase encoding a plausible mechanism in medaka?	90
5.1.9 Looking for a second oscillator in medaka using the Wnt and FGF signaling reporter lines	90
5.1.10 Her7 paralogs could fulfill the requirements of a “second oscillator”	91
<b>5.2 Exploring robustness to variation in levels of Her7</b>	92
5.2.1 Her7 is essential for medaka segmentation	92
5.2.2 Reduced levels of Her7 in the Her7-Venus1 line can sustain normal segmentation in embryos	93
5.2.3 The period of oscillations is robust to changes in her7 levels	94
<b>5.3 A comparative analysis of Hes/Her dynamics and function in medaka, mouse and zebrafish</b>	95
5.3.1 Oscillation dynamics in medaka, zebrafish and mouse	96
5.3.2 Medaka her7 is functionally equivalent to the combination of zebrafish her7 and her1	97
5.3.3 Medaka her1/11 is functionally more related to zebrafish her11 than her1	98
<b>6. Outlook</b>	100
<b>7. Materials and methods</b>	102

<b>7.1 List of genes referenced in this study</b>	102
<b>7.2 Generation of medaka lines by CRISPR/Cas9</b>	102
7.2.1 sgRNA design	103
7.2.2 sgRNA synthesis	105
7.2.3 Testing sgRNA efficiency	106
7.2.4 Donor vector design	107
7.2.5 Cloning of homology arms for donor vectors	107
7.2.6 Site-directed mutagenesis	111
7.2.7 Medaka single-cell injections	111
7.2.8 Removal of the donor backbone for the generation of the Her7-Venus2 line	113
7.2.9 Her7 knockout line	113
7.2.10 Fish husbandry	113
<b>7.3 Genotyping</b>	114
7.3.1 Genotyping strategy	114
7.3.2 Settings for PCR genotyping	114
<b>7.4 Working with medaka embryos</b>	118
7.4.1 Dechoriation of medaka embryos	118
7.4.2 Whole embryo imaging	119
7.4.3 Culture of medaka PSM explants	121
7.4.4 Temperature perturbation experiments	122
7.4.5 Skeletal staining	123
<b>7.5 Molecular biology</b>	124
7.5.1 General cloning	124
7.5.2 Dehydration of medaka embryos for colorimetric in situ hybridisation (ISH) or in situ hybridisation chain reaction (HCR)	125
7.5.3 In situ hybridisation (colorimetric)	133
7.5.4 In situ hybridisation chain reaction (HCR)	133
<b>7.6 Data analysis</b>	133
7.6.1 Image analysis	133
7.6.2 Wavelet analysis	133
7.6.3 Statistics	134
<b>7.7 Solutions</b>	134
<b>8. Appendix</b>	137
8.1 Derivation of a relationship between frequency and $\alpha$ from the Alpha model	137
8.2 Q10 calculation	138
8.3 Abbreviations	138
<b>Bibliography</b>	139



# Acknowledgements

First of all I would like to thank Alexander Aulehla for inspiring scientific discussions. I have learned so much from being in this lab, thank you for this opportunity. To the whole Aulehla lab, current and former members- you have been amazing colleagues. Thank you all for your help and support, you have really made me feel at home.

Special thanks to Silvija Svambaryte, the other half of the medaka team, for making me laugh every day, and to Takehito Tomita for helpful (and fun!) discussions and for introducing me to the alpha model. Thanks to Kristina Stapornwongkul for starting the medaka direction in the lab, and for being encouraging from the start.

Thanks to Jochen Wittbrodt and the whole Wittbrodt lab for always answering questions and kindly facilitating our work with medaka. I would especially like to thank Thomas Thumberger for his enthusiasm when introducing me to CRISPR and teaching me how to microinject, and his collaboration on the design of the knock-in lines.

Thanks to Paul François for helpful discussions.

A big thanks to Sabine Görgens, Sabrina Germoni and LAR for being our backbone and taking care of the medaka. I am also grateful for the support from the Peri, Gilmour and Leptin lab members. Thanks to Kiyoshi Naruse for his expert guidance, and Hiroyo Kaneko for help with ordering medaka from Japan. Also thanks to the Medaka National BioResource Project (NBRP Medaka) for hatching enzyme and expertise. Thanks to Dr. Ai Shinomiya and Professor Takashi Yoshimura for kindly providing temperature data from their outdoor medaka breeding facilities.

To the graduate office, Carolina Garcia Sabate and Matija Grgurinovic, and to all my friends at EMBL- thank you, your support has meant alot.

Thanks to Christoph Winkler, Juan Martines Morales and Daniel Liedtke for sharing their medaka protocols. Thanks to Jonas Hartmann for helping me automate the tail imaging. Thanks to Daniel Krueger, Kevin Nzumbi Mutemi and Luca Santangeli for last-minute discussions.

Thank you to Maria Leptin, Detlev Arendt, Jochen Wittbrodt for serving on my thesis advisory and defense committees. Thanks to Alexis Maizel for agreeing to serve on my defense committee.

None of this would have been possible without my parents and my siblings- I miss you all.

Finally, I want to thank Luca Rappez, I would not have made it without you.



# Summary

Developmental patterning shows remarkable robustness in the face of changing environmental conditions. One particular challenge faced by externally fertilized embryos is how to maintain proper growth and patterning despite temperature variation. In order to address the mechanism behind temperature-invariant patterning, I study somitogenesis in Japanese medaka (*Oryzias latipes*), which has been shown to tolerate a wide range of temperatures. The periodic formation of somites from the presomitic mesoderm (PSM) in vertebrates is under the control of a molecular “clock”, consisting of oscillatory target genes in the Notch, Wnt and FGF signaling pathways. While it is clear that these periodic signals are involved in regulating the timing of somitogenesis, how oscillations encode information, and how this is coordinated in space is still a matter of ongoing research. To study somitogenesis in medaka, I generated endogenous knock-in reporters to visualize signaling activity in the Notch, Wnt and FGF pathways during somite formation. Importantly, an oscillating Notch signaling reporter, Her7-Venus, allows quantification of segmentation clock oscillations in medaka for the first time. Time-lapse imaging of Her7-Venus oscillations revealed coherent waves that follow a period gradient in the PSM, which is reminiscent of dynamics in higher vertebrates. Imaging of this reporter at different temperatures revealed that segmentation clock oscillations are globally faster at higher temperatures. Importantly, while period changes 2.2 fold, average somite size changes 1.15 fold between 23-35°C. A detailed analysis of the period gradient reveals that oscillations change their period differently in the posterior and anterior PSM, resulting in a constant period gradient amplitude. In addition, the phase gradient amplitude is temperature-invariant. These results provide the first quantitative insight into how underlying signaling dynamics respond to temperature changes and allow robust patterning during somitogenesis. Examining these findings in the context of existing models of somitogenesis could provide insight into how robustness is achieved in this complex system.



# Zusammenfassung

Die Embryonalentwicklung weist eine zum Teil erstaunliche Unempfindlichkeit gegenüber wechselnden äußeren Umweltfaktoren auf. Diese Robustheit gegenüber externen Faktoren, insbesondere der Temperatur, ist essentiell für die Entwicklung von Organismen deren Fortpflanzung auf äußerer Befruchtung basiert. In meiner Arbeit habe ich den Einfluss von Temperatur auf die Segmentierung des japanischen Reisfisches Medaka (*Oryzias latipes*) untersucht. Die Segmentierung des presomitischen Mesoderms (PSM) wird durch eine komplexe, kombinatorische, molekulare "Uhr" kontrolliert, welche die periodische Aktivität dreier Signalwege, Notch, Wnt und FGF einschließt. Diese wiederum steuern die oszillierende Expression von Zielgenen. Während der Einfluss dieser molekularen Uhr auf die zeitliche Steuerung der Segmentierung nachgewiesen wurde, bleibt die Frage, wie Zellen diese Oszillationen und dynamischen Signale auswerten, weiterhin Gegenstand aktueller Forschung. Um diese Frage im Kontext äußerer Einflüsse beantworten zu können, habe ich Medaka-Reporterlinien zur Visualisierung der dynamischen Signalaktivität von Notch, Wnt und FGF Signalwegen mithilfe von CRISPR-Cas9 generiert. Dadurch konnte zum ersten Mal die oszillierende Expression von Her7-Venus in Medaka gezeigt und quantifiziert werden. Die quantitative Analyse von Her7-Venus-Oszillationen offenbarte kohärente Wellen, die einem Periodengradienten im PSM folgen und somit denen in höheren Wirbeltieren ähnlich sind. Die Visualisierung dieses Reporters bei verschiedenen Temperaturen ergab, dass der Takt der Segmentierungsozillationen allgemein schneller bei höheren Temperaturen ist. Während sich die Periodendauer um das 2,2-fache erhöht, ändert sich die durchschnittliche Somitengröße um das 1,15-fache im Temperaturbereich zwischen 23 und 37°C. Eine detaillierte Analyse des Periodengradienten zeigte, dass Oszillationen ihre Periodendauer positionsspezifisch entlang der anterior-posterioren Achse unterschiedlich ändern, was zu einer konstanten Amplitude des Periodengradienten im PSM führt. Währenddessen bleibt die Phasenverschiebung dieser Oszillationen, unabhängig von der Umgebungstemperatur, konstant. Die Ergebnisse dieser Arbeit erlauben erstmals quantitative Einblicke in die Frage, wie wechselnde Temperaturbedingungen sich auf die Dynamiken der relevanten Signalwege auswirken und wie diese eine fehlerfreie Embryonalentwicklung sicherstellen.



# 1. Introduction

## 1.1 Phenotypic robustness in developing systems

In 1942, Waddington first described the concept of “canalization”, or the fact that the biochemical reactions which underlie development evolve to be inherently buffered. In other words, natural selection favours those paths where, despite some variation in the initial conditions, the developmental outcome will always be roughly the same [1]. Thus, even when light, temperature, humidity, oxygen levels or nutrient availability are constantly fluctuating, embryos will grow and pattern according to defined developmental trajectories. Such developmental stability in the face of variable conditions is known as phenotypic robustness [2]. Implicit in this definition is the idea that there exists a ground truth for what developmental outcome is supposed to look like, regardless of the initial conditions. On the contrary, external influence can in some cases have a strong impact on the developmental outcome of genetically identical embryos, resulting in developmental plasticity. For example, the wing pattern of the African butterfly (*Bicyclus anynana*) depends on the temperature it experiences as a larvae, and is important for regulating cycles of mating behaviour [3]. In fact, sex-determination itself is a temperature-dependent process in several reptile and fish species [4, 5]. Thus, we need to carefully distinguish between those traits which are phenotypically robust and those which are plastic. Importantly, robust patterning is one way of ensuring that the proportions of tissues and organs are maintained during environmental variation so that they can fulfill their intended function in the embryo.

### 1.1.1 Robust patterning upon variation in size

To achieve robust embryonic development, one important aspect is to ensure correct size control and patterning of tissues and organs. Classical experiments in salamander where prospective leg tissue was grafted from a small to a big species showed that the resulting leg grew to the expected smaller size of the donor, not the larger host [6]. This demonstrated that size control is an intrinsic property of tissue, although extrinsic factors are also known to play a role in this process [7]. In *Drosophila*, nutrient availability and rearing temperatures have a measurable effect on the final size of adult flies. Consequently, organs and tissues have to scale accordingly. Interestingly, while body and organ size is a relatively plastic trait, organ patterning tends to be highly robust in that the relative proportions, and therefore function, is maintained [8, 9]. [10]. Furthermore, robustness of size control also plays a part in the

regulation of bilateral symmetry within the same individual. This is illustrated in zebrafish embryos, where an injury to one of the two optic vesicles is followed by compensatory growth exclusive to the injured side, so that both eyes grow to the same final size [11].

A dramatic example of robust patterning at the whole body level has been demonstrated by size reduction of early stage vertebrate embryos. Surgical size reduction was first carried out by Cooke in 1975 in *Xenopus* embryos at the blastula stage. Following the observation that embryos form the same number of somites despite minor variations in available egg material, Cooke tested how many somites would form following the removal of a significant part of the blastula stage embryo. Interestingly, size reduced embryos were smaller overall, but formed the correct number of proportionally smaller somites at the right time [12]. This experiment has recently been replicated in zebrafish, where surgical size-reduction lead to the development of smaller embryos with proportionally smaller organs. Again, the authors observed that size-reduced embryos formed a normal number of smaller somites, with the same temporal progression and axial growth rate as in full-sized controls [13]. Similar findings were reported in genetic mouse mutant with reduced embryo size [14], indicating that whole-body scaling is a common feature of embryonic development in multiple organisms.

### 1.1.2 Robust patterning during variation in temperature

Environmental temperature is arguably the factor with the most ubiquitous influence on all biological processes. Considering the fact that biochemical reactions and basic cellular behaviours, including cell cycle timing and motility, are temperature-dependent [15, 16], seasonal and daily cycles of temperature fluctuation will inevitably influence the progression of externally developing embryos. In fact, several species, including fish, amphibians, insects, nematodes and cnidarians undergo embryonic patterning, growth and morphogenesis at a wide range of temperatures [17-22]. In some cases, temperature has a dramatic effect on the outcome, such as in *Hydra* polyps, which are not strictly embryonic, but exhibit continual growth and patterning. Interestingly, the maximum body size reached by *Hydra* polyps before budding is highly temperature dependent, with a larger body size correlating to lower temperature [21]. In this case temperature induces differences in cell number and size, but also in the number of tentacles [23]. In contrast, while temperature affects both body size and rate of development in *Drosophila* embryos, patterning follows a stereotypical order of events which terminate at specific milestones [10, 20]. For example, temperature-induced changes to drosophila wing disk size still results in normal expression of patterning markers at certain

developmental milestones, although the temporal order of appearance does not always scale linearly with size [9]. This implies the existence of an active temperature-compensation mechanism controlling patterning in *Drosophila*, but perhaps not in *Hydra*.

For an embryo to develop normally across temperatures, this has to be coordinated with patterning of tissues and organs. This is not trivial given that the underlying biochemical reactions may respond differently to temperature. In support of this, tissues in *Drosophila* differ in their extent of phenotypic plasticity with respect to temperature [24]. In particular, between 17-25°C the size of the wing is more plastic than the size of the leg with respect to body size. Interestingly, this was related to tissue-specific thermosensitivity of cell proliferation rate. The relationship between tissue size and temperature was also explored in zebrafish, where the rate of embryonic development shows a strong temperature-dependence [19, 25]. To investigate patterning in embryos grown at different temperatures in more detail, Schroter et al. quantified how somite size would change between 20-30°C. Intriguingly, although somitogenesis period was strongly correlated with temperature, they found that somite size was temperature-invariant. This was true throughout somitogenesis, where somite size also changes as a function of axial position [26].

Another influence of temperature on development involves the fact that expression noise is also temperature-dependent. For example, in *Drosophila* gene expression noise is increased in individuals reared at 13°C or 29°C relative to the baseline at 18°C [27]. Thus, robustness to temperature would be expected to include mechanisms to deal with increased expression noise. In *Drosophila*, the Bicoid gradient is a major determinant of anterior-posterior polarity, and would therefore be expected to be highly robust. On the contrary, detailed studies of the Bicoid protein gradient revealed that it is highly variable between individuals, and that variability is even increased when temperature is changed between 9-29°C. Despite this, downstream Hunchback expression is always very tightly regulated, indicating some hitherto unknown mechanism reduces the noise in the Bicoid gradient in a temperature-independent manner [28].

Surprisingly, developing embryos can even overcome extreme temperature perturbations. For example, *Xenopus* embryos developing in a temperature gradient spanning 14°C caused a 15 minute desynchronization of cell division time on either side of the embryo, which resulted in differences in the cell number and size on either half [29]. While this desynchronization resulted asymmetric expression of the mesodermal marker Xbra, this was corrected later in development and led to normal, viable tadpoles. Similar experiments were carried out in *Drosophila* where, in contrast to *Xenopus*, the early embryo is not cellularized.

In these experiments, embryos were subjected to a sharp temperature step by using a microfluidic setup to create a 10°C difference between the posterior and anterior half of the embryo [30]. Interestingly, this caused the warmer half of the embryo to be advanced in its cell cycle progression relative to the colder half, regardless of anterior-posterior orientation. Remarkably, downstream patterning events such as the expression of even-skipped stripes and hunchback appeared at the expected positioning, although temporal progression was slightly different. While embryos are unlikely to encounter this type of situation in nature, these examples highlight the presence of a compensatory mechanism (or an emergent property of the system) that allows the embryo to deal with this type of challenges. Thus, while we have multiple examples of phenotypic robustness in biology, comparatively little is known about the underlying molecular mechanisms.

## 1.2 Medaka as a model to study robust patterning

Medaka (*Oryzias latipes*), also known as the Japanese ricefish, is a fresh-water fish found predominantly in East Asia (**figure 1**). In Japan, where it has been used as a research model since the early 1900's, medaka can often be found swimming in shallow rice fields [22, 31, 32]. As a research model, medaka is often taken to be similar to zebrafish, and while both of these are Teleost fish, they are in fact separated by at least 110 million years of evolution [32, 33]. In most aspects the medaka model does offer the same advantages as the zebrafish, including its small size and continuous production of rapidly developing embryos [33]. On the other hand, there are several differences between the two species, in terms of both genetics and morphology. For example, the medaka genome is relatively small at 700 Mb, which is roughly half the size of the zebrafish genome [34, 35]. Although all Teleost fish have a large number of duplicated genes due to an additional round of whole genome duplication in this lineage, the large evolutionary distance between zebrafish and medaka has resulted in differential retention of various genes [33]. Unlike zebrafish, medaka also has a high tolerance for inbreeding, resulting in several inbred lines which greatly facilitate genetic manipulations and comparative studies. Broadly, wild Japanese medaka split into two groups, the Northern and Southern population, each with its own defined genetic differences, which have been used to create inbred lines [32]. Medaka's tolerance to inbreeding has also enabled the creation of a panel of 200 inbred lines derived from wild medaka of the Southern population [36]. These lines represent an exciting opportunity to explore the interplay between genotypic and phenotypic variability, which ultimately could expand our knowledge about mechanisms of robustness. Together, the availability of inbred lines and established tools for generating transgenic and endogenous knock-in lines makes medaka a powerful model [37-39].

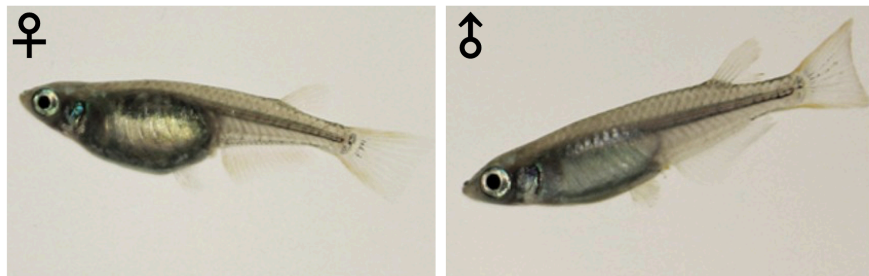


**Figure 1:** Medaka adult female (left) and adult male (right). Adapted from Hilgers et al. [40], reproduced under the terms of the Creative Commons attribution license (CC-BY 4.0).

In several aspects, medaka is a particularly interesting model to study robustness, as it has been reported to tolerate great variation to temperature and salinity [32, 40]. In particular, temperature has a strong effect on growth dynamics, and development can be easily sped up or slowed down with no obvious effects on patterning [22]. Medaka are highly tolerant in this respect, and embryos have been reported to develop at 4-35°C until the heart starts beating, and at 18-35°C after. Zebrafish are much less robust, tolerating a range of about 25-33°C [19, 25, 31, 33]. Adult medaka have an even more impressive temperature tolerance than embryos, and can survive between 4-40°C, or even below as long as the water does not freeze [31]. However, post-embryonic growth, in particular the size and age at maturity, is highly temperature dependent [41]. Furthermore, spawning does not occur along this full temperature range, and sharply decreases when temperature is lowered from 25°C to 15°C [42]. Interestingly, medaka cell-lines also have the ability to proliferate with temperature-dependent growth kinetics between 15-33°C, although this ability depends on the geographical origin of the medaka strain from which they were derived (Hirayama J comp physiol B, 2006). While there are several studies reporting the temperature-dependence on the rate of embryonic development in medaka, the effect of this on embryonic patterning has not been addressed in detail, except possibly an increased level of abnormalities above 34°C [5]. Furthermore, despite this impressive temperature tolerance, there are no studies which look closer at the mechanisms behind this phenomenon during development.

The influence of temperature on medaka development has been given more attention in the context of phenotypic plasticity during sex-determination. Sex is genetically determined in medaka, with XY males and XX females, as first described by Aida in 1921 [43]. Despite this, phenotypic sex-reversal can be induced by temperature or hormones [5, 44, 45]. In particular, temperatures above 27°C cause the reversal of XX females to XX males, with 24-40% efficiency at 32°C, and 100% efficiency at 34°C [5, 45]. Interestingly, while XX males grown at 32°C are fertile, XX males grown at 34°C are not, despite the fact that they form

morphologically normal testes and mature spermatozoa [5]. In contrast, XY males do not undergo sex reversal between 17-34°C, unless estradiol is added to the water, a phenomenon which is made more efficient at low temperature [5, 44]. Thus, although they can tolerate a wide range of temperatures with no obvious effects on patterning, medaka development is strongly influenced by temperature when it comes to sex determination.

The wide range of temperatures which are permissible for embryonic development in medaka, together with the feasibility of genetic manipulation, make this model organism well suited for studies on robustness. Therefore, in this thesis I focus on medaka somitogenesis as a paradigm to study robust patterning.

## 1.3 Somitogenesis as a model to study robust patterning

### 1.3.1 Somitogenesis patterns vertebrate embryos

During early vertebrate development, patterning of the anterior-posterior axis is closely linked to the process of somite formation, known as somitogenesis. Somites are transient mesoderm-derived precursors of the axial skeleton, including the vertebrae, skeletal muscle and some dermis. The formation of somites is a conserved feature of vertebrate development, although the period of somitogenesis and total number of somites is species-specific [46]. The presomitic mesoderm (PSM) provides the material for the formation of somites, which separate in pairs at regular intervals on either side of the neural tube, in an anterior to posterior order (**figure 2**). As the tissue is progressively patterned, the PSM also elongates from the tailbud, located at the posterior tip of the tail, which provides new tissue for segmentation (reviewed in [47]).

As somites separate out of the PSM, they continue to differentiate, resulting in a gradient of maturity from anterior-posterior. In addition to the visible somite boundaries, somites are further subdivided into two distinct compartments through the influence of surrounding tissue. Specifically, the dorsal somite compartment will eventually contribute to dermis and muscle, and is therefore known as the dermomyotome. The ventral somite compartment is fated to form the bones and tendons of the axial skeleton (ribs and vertebrae) and is referred to as the sclerotome (reviewed in [48]).

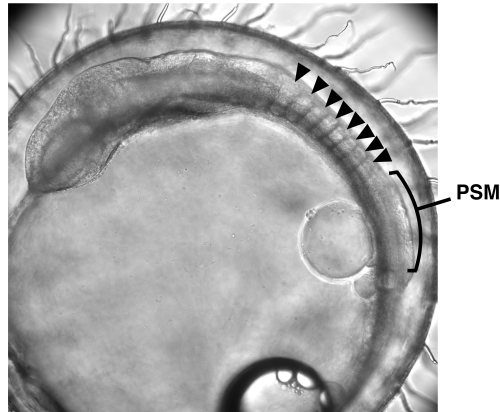


**Figure 2:** Medaka embryo at the 8-9 somite stage (corresponding to Iwamatsu stage 22, [49]) undergoing somitogenesis, a process during which somites (labeled with black arrowheads) periodically form from the unsegmented presomitic mesoderm (PSM).

### 1.3.2 *Mesp* regulates somite anterior-posterior identity

An additional layer of anterior-posterior molecular patterning is established in each somite even before somite boundaries are formed, and is important for downstream fate decisions, such as polarity of neuronal growth in the peripheral nervous system [50], as well as proper patterning of vertebrae, which form from the fusion of each anterior compartment with the posterior compartment of the preceding somite during a process called re-segmentation (reviewed in [48]).

The initiation of somite anterior-posterior polarity can be traced back to the *Mesp* family of bHLH transcription factors. In mouse, *Mesp2* is under the positive regulation of Notch signaling which marks the expression domain of the next forming somite, adjacent to the last formed boundary in the anterior PSM. The expression of *Mesp2* is dynamic, starting at one somite width, which is then gradually restricted to the anterior domain of the next forming somite. The refined stripe disappears as expression starts to come up in the next block of differentiating cells. As a consequence, occasionally two stripes of expression can be seen, one thin anterior stripe which is fading out as the somite boundary is forming, and a thicker stripe further down where the next somite is being specified [51, {Morimoto, 2005 #374}. *Mesp2* expression is crucial to proper anterior-posterior somite polarity, as shown by genetic knockouts which do not form somites and express posterior markers in the region corresponding to segmented PSM in wildtype [51] (also reviewed in [52]). Conversely, *Mesp2* overexpression causes a downregulation of the posterior somite marker *Uncx4.1* [53].

In zebrafish and medaka there are two *mesp* orthologs, *mesp-a* and *mesp-b* [54-57]. As in mouse, these genes are expressed in the region just below the last formed somite, and

in zebrafish overexpression of *mesp-b* was found to cause somite defects and promote the anterior somite fate [54]. Despite the fact that the expression patterns of these overlap in the PSM, only *mesp-b* was found to be essential to proper somite formation in zebrafish [54].

### 1.3.3 The role of signaling oscillations in the segmentation clock

The rhythmic process of somite formation was proposed to be temporally controlled by repetitive, oscillatory signals even before we had molecular evidence of this kind of regulation [58, 59]. In the last decades, experimental evidence has linked the timing of somitogenesis to a system of oscillating genes in the PSM of a wide range of vertebrates, including chick [60], corn snake [46], mouse [61], *Xenopus* [62], zebrafish [63, 64], and medaka [57, 65]. Interestingly, oscillatory expression of pair-rule genes has also been identified during segmentation in the arthropod *Tribolium castaneum* [66-68]. While the specific genes involved vary depending on the species, these signaling oscillations are part of a conserved strategy in segmenting animals, and have been termed the “segmentation clock” (reviewed in [47]).

### 1.3.4 The dynamics of Notch signaling oscillations

A striking feature of Notch signaling oscillations in the PSM is that they appear coordinated across the tissue. Live imaging studies have revealed that Notch signaling oscillations in single cells along the PSM are phase-shifted relative to each other which gives the impression of a travelling phase wave that moves from posterior to anterior, in sync with the formation of each segment pair [69-77]. In turn, the phase shift between PSM cells is caused by the presence of a period gradient, where cells in the posterior oscillate faster than cells in the anterior [60, 74, 77]. As a rule, the period of morphological segmentation matches the period of oscillations in the posterior PSM. Interestingly, the presence of a period gradient appears to be a conserved feature in all systems employing segmentation clock oscillations, as evidence supporting its presence has also been found in arthropods [67]. The conceptual implications of this dynamic feature are discussed further in **section 1.5**.

### 1.3.5 The Hes/*her* family are at the core of Notch signaling oscillations in vertebrates

Canonical Notch signaling involves the interaction between the transmembrane receptor Notch1 and the Delta ligands Delta-like1 and 3 (Dll-1 and Dll-3 [78, 79]). Upon ligand

binding, the Notch intracellular domain (NICD) is cleaved by the gamma-secretase complex, located in the cell membrane, which consists of four different protein subunits. Among these, Presenilin (either one of two paralogs in mammals) is responsible for mediating this proteolytic cleavage. Cleaved NICD then travels into the nucleus where it activates Notch target genes. Signaling through the Notch receptor can be further modulated by one of several glycosyltransferases (reviewed in [80, 81]). The expression of several of these genes downstream of Notch signaling are known to oscillate in vertebrate PSM. Notably, Lunatic fringe (*Lfng*), a secreted glycosyltransferase that negatively regulates Notch-Delta signaling, is an important component of Notch signaling oscillations in chick and mouse, but not in zebrafish or medaka [57, 61, 82, 83]. Other oscillatory components include the Notch1 receptor, the Dll-1 ligand and the NICD itself in mouse and chick, and the Notch ligand DeltaC in fish [78, 84, 85].

Notable among the Notch signaling components involved in the segmentation clock is the Hairy and enhancer of split related (*Hes/her*) family. Members of this transcription factor family have been found to oscillate in the PSM of every vertebrate species where they have been studied [57, 60, 62-65, 86]. The *Hes/her* family is characterised by the presence of a basic helix-loop-helix (bHLH) domain which mediates dimerisation and DNA binding to enable transcription factor function (reviewed in [87]). In mouse, three members of the *Hes/her* transcription factor family are known to oscillate in the PSM : *Hes7* [88, 89], *Hes1* [90] and *Hes5* [91]. Among these, *Hes7* is the only one which is exclusively present in the PSM and is essential for somite morphology and polarity [87, 89]. In mouse, the loss of *Hes7*, but not *Lfng*, leads to absence of all oscillatory Notch signaling in the PSM, suggesting that *Hes7* is upstream of *Lfng*, and at the core of Notch signaling in the segmentation clock [92]. Similarly, combined loss of the *Hes7* orthologs (*her1* and *her7*, described in **section 1.3.6**) in zebrafish also leads to a loss of proper somite formation and the loss of *deltaC* oscillations [64, 93].

### 1.3.6 A network of her protein heterodimers regulate oscillatory behaviour in zebrafish and medaka PSM

A whole genome duplication early in the teleost fish lineage is responsible for the presence of multiple paralogs in these species compared to their mouse counterparts [33]. Thus, for the mouse *Hes7* gene, four orthologs have been identified in zebrafish: *her7*, *her1*, *her5* and *her11* [65]. Of these genes, the expression patterns of *her7* [64], *her1* [63], and *her11* [94] are all oscillatory, but *her5* is not expressed in the zebrafish PSM [65]. In medaka there are three corresponding *Hes7* orthologs, *her7*, *her5* and *her1/11*, which are all expressed in

the PSM in an oscillatory fashion [57, 65]. The medaka *her1/11* gene is named in this way because it exhibits the combined expression patterns of zebrafish *her1* and *her11* [65, 94].

In zebrafish, the core mechanism underlying Notch signaling oscillations is thought to be mediated by *her7* and *her1* [95], where they regulate posterior and anterior somite formation and patterning, respectively [64, 93, 96]. Although these genes appear complementary, it is clear that they negatively regulate each other. Specifically, upregulation of either results in increased inhibition of both, although *her7* appears to play a dominant role in the interaction [97]. In contrast, knockdown or overexpression of the other oscillatory paralog *her11* alone has no effect on somite boundary formation or the expression of *her7* or *her1* [94, 98].

From *in situ* hybridisation studies of the medaka *her* genes, it is clear that these are more similar in their expression to higher vertebrates than zebrafish [65]. Specifically, in medaka, mouse and chick, expression of *Hes7* and its orthologs is characterized by a posterior U-shaped domain and a single wave that travels anteriorly during wave propagation [57, 60, 89, 99]. In zebrafish, on the other hand, this expression domain is extended by up to two discrete anterior waves in addition to the U-shaped domain, indicating the presence of multiple traveling waves (**figure 3**) [64, 65]. However, unlike zebrafish there are very few studies looking at the role of *her* genes in medaka PSM, and these are mostly limited to descriptive observations [57, 65, 100, 101]. Although there are multiple mutants of somitogenesis which show interesting phenotypes and perturbed *her7* expression in the PSM, the genes involved are as yet unknown [100]. The only functional study of *Her* genes in medaka to date reported morpholino knockdown of *her1/11*, which did not cause any significant phenotype alone, but caused a loss of somite formation when combined with knockdown of *her13.2* [101].

Beyond the mouse *Hes7* orthologs, there are also orthologs of *Hes1*, *Hes5* and *Hes6* which are expressed in the PSM of zebrafish and medaka, indicating a role for these in somitogenesis (summarised in **Table 1**) [65, 98].

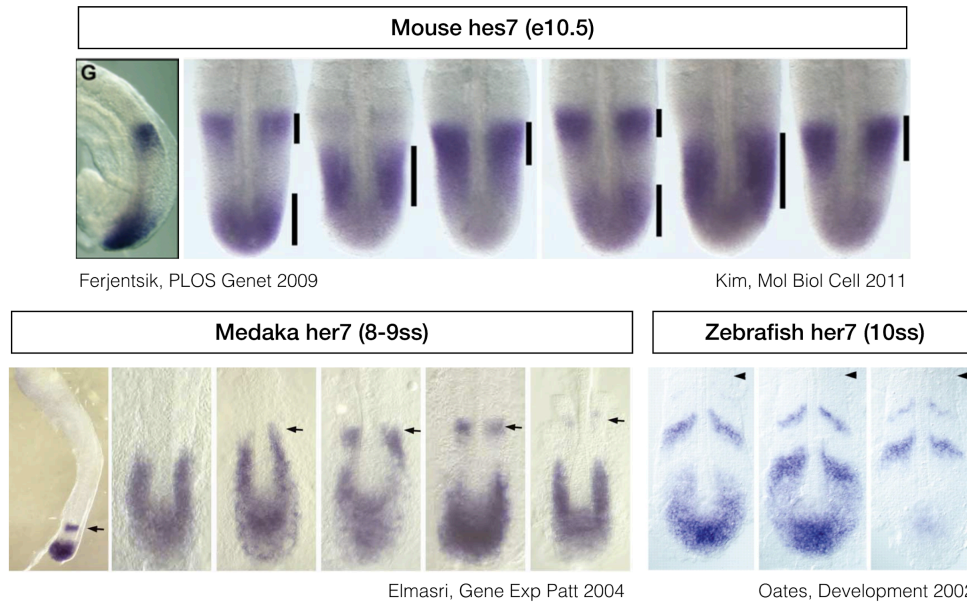


**Figure 3:** Comparison of *Hes7* expression in mouse at e10.5 (reproduced from Ferjentsik et al. [92, 102]), and *her7* expression in medaka at the 9 somite stage (reproduced from Elmasri et al. [57]) and zebrafish at the 10 somite stage (reproduced from Oates et al. [64]). Note the presence of multiple stripes of expression in the anterior PSM of zebrafish. Reproduced under the terms of the Creative Commons attribution license (CC-BY 4.0) or with permission from the specified journals.

**Table 1:** Summary of *Hes/her* orthologs in mouse, medaka and zebrafish which are expressed in PSM. Genes which show oscillatory activity in the PSM are marked with an asterisk, those which are not clearly oscillating but seem to be variable are in parenthesis. (Adapted from [65, 98])

Mouse ortholog	Medaka	Zebrafish
<i>Hes1</i> *	<i>her6.1</i>	<i>her6.1</i>
<i>Hes5</i> *	( <i>her4</i> ), <i>her12</i> *	( <i>her4.1</i> ), <i>her4.2</i> , <i>her12</i> *, <i>her15</i> *
<i>Hes6</i> (not expressed in mouse PSM)	<i>her13.1,her13.2</i>	<i>her13.1, her13.2</i>
<i>Hes7</i> *	<i>her7</i> *, <i>her5</i> *, <i>her1/11</i> *	<i>her7</i> *, <i>her1</i> *, <i>her5</i> , <i>her11</i> *

### 1.3.7 Hes/her transcription factors oscillate by a negative-feedback mechanism

In mouse, *Hes7* is oscillatory both at the RNA level [89, 99], and at the protein level [88]. The fact that HES7 is a transcriptional repressor [89, 99] led to the hypothesis that HES/Her family transcription factors autonomously generate oscillations by delayed autoregulatory negative feedback loops [103, 104]. In support of this, it has been shown that HES7 protein can bind to its own promoter and periodically represses expression of *Hes7* RNA in mouse [88]. Similarly, overexpression studies of both *her7* and *her1* in zebrafish result in reduced expression and loss of oscillations in both genes, indicating that these two inhibit their own and each others cyclic expression [97]. Mathematical modeling that builds on this

hypothesis has shown that a critical parameter in the determination of oscillation period is the delay in the autoregulatory negative feedback loop generated by HES/Her proteins [103, 104]. In support of these models, it has been shown that removing two of three introns shortens the period of oscillations, resulting in the formation of more somites [71].

In zebrafish, the Her proteins can only carry out their auto-repressive function as dimers. Biochemical studies have identified that while Her1 functions as a homodimer, Her7 requires heterodimerization with Her13.2 to bind DNA. Analysis of the Her network topology suggests that Her13.2 functions as a network hub, and that Her7 plays a dominant role in regulating the network output [95]. In support of a central role for Her13.2, although it is not oscillatory in the PSM, this gene is required for *her7/her1* oscillations and proper somite polarization in zebrafish [101, 105]. In addition, *her13.2* has previously been implicated in changing the period of the segmentation clock: a zebrafish *her13.2* hypomorph caused a 6.5% lengthening of segmentation period, leading to the formation of fewer segments in mutants relative to wildtype [106]. The other oscillating *her* genes in zebrafish, Her12 and Her15 also have the ability to bind DNA as homo- or heterodimers with Her13.2, and overexpression of either disrupts the formation of somite boundaries and disrupt oscillatory expression of *her1* and *her7* [95, 98].

### 1.3.8 Gradients in the PSM regulate the differentiation front

In addition to the clock, a system of posterior to anterior Wnt and FGF signaling gradients is involved in the regulation of somite formation (**figure 4**) [69, 107-110]. These gradients exhibit dynamic behavior in that the anterior edge of the gradient moves posteriorly as the body axis elongates. As cells come progressively closer to this anterior edge they cease to oscillate and start expressing markers characteristic of differentiation, including *Mesp2*, which marks the next forming somites [51, 111]. Therefore, these gradients are often collectively referred to as the “differentiation front”. In addition to the Wnt and FGF gradient, there is a retinoic acid (RA) gradient that acts in the opposite direction [112, 113]. This gradient is involved in regulating the anterior reach of the FGF gradient [114]. In addition, RA is involved in regulating the left/right symmetry of somite formation in chick, mouse and *Xenopus* [115-117].

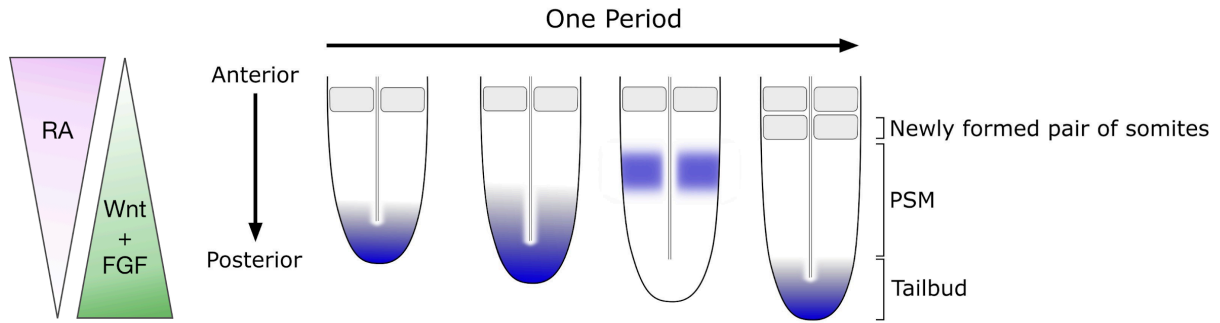


**Figure 4:** Schematic of the gradients and clock genes involved in the regulation of somite formation. The Wnt and FGF signaling gradients (green) are high in the posterior, and low in the anterior. The RA gradient (pink) is high in the anterior, and low in the posterior. With each cycle of oscillatory gene activity (shaded blue), one pair of somites forms from the unsegmented PSM.

Canonical Wnt signaling is mediated by signaling activity of  $\beta$ -catenin, which is also involved in cell-cell adhesion on cell membranes. In the absence of Wnt signaling,  $\beta$ -catenin is phosphorylated and targeted for degradation by the destruction complex, which (among other proteins) contains the scaffolding protein Axin2, a negative regulator of Wnt signaling. On the other hand, active Wnt signaling leads to the sequestration of the destruction complex so that  $\beta$ -catenin is no longer degraded. In these circumstances,  $\beta$ -catenin can enter the nucleus and relieves TCF/LEF mediated repression of Wnt target genes (Reviewed in [118, 119]). The role of Wnt gradients in the establishment of the anterior-posterior axis is a highly conserved feature of bilaterians [120]. In mouse embryos, a Wnt signaling gradient mediated through a gradient of Wnt3a ligand and the action of  $\beta$ -catenin (Ctnnb1) plays an important role in maintaining the anterior-posterior identity of the PSM [69, 121]. Loss of  $\beta$ -catenin causes axial truncation and failure to form normal somites, whereas gain of function caused an upregulation in the PSM with a loss of the gradient. Strikingly, mutants with stabilized  $\beta$ -catenin had expanded, fgf signaling and oscillatory domains with multiple waves of Lunatic fringe expression [69] suggesting that Wnt acts through  $\beta$ -catenin to regulate the extent of the oscillatory domain. In Zebrafish PSM, a posterior to anterior Wnt signaling gradient is also present like in mouse, and is similarly reflected in a nuclear  $\beta$ -catenin gradient [107].

In addition to the Wnt signaling gradient, an anterior-posterior FGF signaling gradient is based on de novo expression of Fgf8 ligand localized to the tailbud. As cells move anteriorly, fgf8 RNA is progressively degraded [109]. This leads to the graded activation of the MAPK/Erk pathway, and has been identified in mouse, chicken and zebrafish embryos [108-110, 122]. Like the Wnt signaling gradient, the FGF signaling gradient maintains oscillatory activity in the PSM, and is also believed to regulate the size and position of the next somite [108].

It is hypothesized that the anterior front of the Wnt and FGF signaling gradients determines the position and size of the next forming somite, labeled by the expression of *Mesp*. In support of this, inhibition of Wnt signaling by the overexpression of *Dkk1* results in a backwards shift of the anterior  $\beta$ -catenin gradient front and *mesp* expression, and the formation of larger somites [107]. Similarly, the expression of *mesp2* is also posteriorly shifted upon FGF inhibition [123]. On the other hand, overexpression of Wnt8 ligand has the opposite effect, resulting in the formation of smaller somites [107]. The formation of locally smaller somites has also been seen in chick following the implantation of Wnt3a-expressing cells or FGF8-soaked beads [108, 121]. Together, these results indicate that the Wnt and FGF signaling gradients play an important role in regulating somite size.

### 1.3.9 Wnt and FGF signaling oscillations in mouse and chick PSM

In addition to being part of the gradients that are believed to impart positional information to the PSM, members of both FGF and Wnt signaling pathways have been shown to oscillate in the context of segmentation [86, 121, 124]. Outside of the Notch pathway, the first gene with oscillatory expression in mouse PSM was discovered to be *Axin2*, which is downstream of Wnt3a signaling [121]. *Axin2* has also been predicted to be oscillatory in chicken [86]. Replacing oscillatory expression of *Axin2* with continuous expression disrupts morphology and polarity of somites, highlighting the importance of dynamic expression in this process [121]. Later studies in mouse, including a large-scale microarray screen later identified multiple genes responsive to Wnt and FGF signaling, including including *Nkd* (Naked cuticle), *Dkk1* (Dickopf 1), *Dusp4* (Dual specificity phosphatase 4.), *Spry2* (Sprouty homolog 2), and the FGF effector pERK [124-128]. In addition, members of the Snail family of transcription factors oscillate in the PSM of mouse and chick [129]. Despite the fact that Wnt and FGF signaling oscillations are found in both mouse and chick, only Notch signaling oscillations have been identified in lower vertebrates, including zebrafish and medaka, so far [47, 86].

In mouse, FGF and Notch signaling oscillations are expressed in phase with each other in the PSM, whereas Wnt signaling oscillations are expressed out of phase with both [78, 86, 121, 124]. The link between the FGF and Notch signaling oscillations is believed to be mediated by *Hes7*, which directly regulates *Dusp4* oscillations in mouse PSM [127]. Unlike Notch oscillatory signaling, Wnt and FGF oscillatory signaling is left intact after *Hes7* knockout [92, 121, 130]. The persistence of oscillations in other pathways have been brought up as a possible explanation how *Hes7* null embryos form some epithelialized somites, although these

are severely mispatterned [89, 92, 131, 132]. In contrast, when all Notch signaling is abolished, such as in a double genetic knockout of presenilin (1 and 2) activity, or during pharmacological inhibition with DAPT, somite boundaries do not form and all cyclic activity (Wnt, Notch and FGF) is lost [92].

## 1.4 Live imaging of segmentation clock oscillations

In order to investigate the role of signaling oscillations it is essential to establish a quantitative and dynamic readout based on live imaging. Live imaging strategies, in turn, need to be tailored to capture the specific requirements of the underlying dynamics that are being analyzed. In particular, the visualization of ultradian oscillations necessitates reporters that match the time scale at which dynamic behaviour is taking place. Generally, two different strategies can be distinguished. First, for the generation of gene activity reporters, RNA and protein can be artificially destabilized by the incorporation of degradation signals [133]. A second strategy rather involves creating a fusion protein, so that introns and endogenous regulatory features of RNA and protein are preserved. To illustrate this, I will shortly outline previously established reporter strategies below.

### 1.4.1 Destabilized gene activity reporters

The generation of transgenic gene activity reporters is the most commonly used strategy for live imaging of dynamics. Often, the promoter of interest is used to drive the expression of a reporter gene. One bottleneck of this approach is to make both the protein and RNA sufficiently unstable to be able to resolve oscillation dynamics, while still producing enough signal for reliable quantification [134]. To this end, the first transgenic live reporter of the segmentation clock in mouse used the *Hes1* promoter sequence to drive a destabilized luciferase protein that was also destabilized at the mRNA level by inclusion of of the *Hes1* 3'UTR [135].

Beyond bioluminescent reporters, destabilized fluorescent proteins have also been used to visualize gene activity oscillations in the PSM, with the added advantage of an increased temporal and spatial resolution. For example, Lunatic fringe oscillations were imaged using a transcriptional reporter expressing the fast-folding YFP-variant Venus (Luvelu) [69]. In this case, the Lunatic fringe promoter was used to drive the expression of Venus fused to a PEST domain, which destabilizes the protein (1 hour half-life, [136]), followed by the Lunatic fringe 3'UTR, which regulates RNA turnover. This reporter line has enabled

quantitative insights into the role of Wnt/ $\beta$ -catenin in the regulation of the Notch oscillatory domain [69], as well as addressing how oscillations can convey spatial information [72, 137] and how oscillating cells can self-organize and re-gain synchrony following randomization of PSM tissue [77, 138].

A major disadvantage of this approach is that the available destabilizing elements may not be sufficient to capture dynamics at fast time scales. For example, in zebrafish, the first segmentation clock reporter carried a GFP which was destabilized to a 1 hour half-life, driven by the Her1 presumed promoter region. However, because oscillation period in zebrafish is only 30 minutes, the protein was still too stable to produce oscillations [139]. To be able to visualize segmentation clock oscillations in the rapidly developing zebrafish, subsequent strategies employed fusion protein reporters.

## 1.4.2 Fusion protein reporters

Fusion protein reporters are generated by the direct merging of the coding sequence with a reporter gene, usually with a linker in between. This approach has the advantage of preserving the endogenous regulation of the RNA and protein, as long as the fusion does not interfere with these mechanisms. An important distinction here is that a fusion protein reporter can be generated as a transgenic, thus adding an additional copy of the gene to the genome, or as an endogenous knock-in.

In mouse, a *Hes7* fusion protein was created by using a ubiquitinated luciferase reporter inserted into a transgene carrying the *Hes7* locus [76]. One advantage of using a transgenic fusion protein reporter is the ability to recapitulate endogenous RNA turnover. In particular, the delay caused by RNA splicing and processing time has been implicated as a possible working mechanism of negative-feedback oscillators [103, 104]. The importance of introns for the oscillatory dynamics of *Hes7* has been explored by their selective removal in the transgenic luciferase-*Hes7* fusion protein [71, 76]. Interestingly, the loss of introns caused phenotypes ranging from expression delays to severe morphological disruptions which phenocopied the *Hes7* knockout, depending on which introns were removed.

In zebrafish, two transgenic Her1 fusion protein reporters have been made by fusing a Yellow fluorescent protein (YFP) to the coding sequence of Her1, under the control of flanking regulatory sequences [70, 75]. Unlike previous reporters, oscillations at both the RNA and protein level were observed in zebrafish PSM. Despite this, none of the Her1 transgenic fusion

protein lines could entirely recapitulate wildtype expression. In the first reporter, oscillations were only detected in the anterior PSM region, in addition to ectopic expression in the notochord [70]. In a second version of this reporter, where the flanking sequence was extended by more than 10 Kbp, oscillations could be detected along the whole PSM, but multiple insertions of the transgene caused a phenotype with 10% slower segmentation and 4-5 missing segments [75]. To date, there are no published fusion protein reporters in the endogenous locus of any of the oscillating segmentation clock genes in the PSM.

## 1.5 The functional importance of oscillation dynamics

Both oscillating “clock” genes and gradient signals are clearly linked to somite formation and integrity, but how cells interpret these dynamic signals is still an open question. While static methods such as *in situ* hybridisation can indicate to some extent the dynamic nature of segmentation clock genes [60], live oscillating reporters have been essential to recent advances in our understanding of the functional importance of dynamics itself [69-77, 137, 138, 140].

This is also because access to the characteristics of oscillation dynamics, such as period and phase information, is only reliably possible through live imaging and quantification of these dynamic signals. The oscillation period describes the time that passes between consecutive oscillation peaks. This term is used interchangeably with frequency, which is the inverse of the period. To describe the progression of an oscillatory signal within one period, each position along the oscillation is assigned a phase. Phase values are often expressed as multiples of  $\pi$ , such that one full oscillation will progress from  $-\pi$  to  $\pi$ , resulting in a total amplitude of  $2\pi$  [141]. Getting direct measures of period and phase is of particular importance in the context of segmentation clock oscillations in the PSM, as both period and oscillation phases change along the PSM. Specifically, oscillation periods are graded along the PSM, where the oscillations within a given cell are faster in the posterior, and gradually slow down as cells approach the anterior where segmentation occurs [74, 77]. The period gradient underlies a gradual phase-shift along the PSM, forming a phase-shift gradient from posterior to anterior [72]. To introduce the current view on the role of the phase and period gradient, I will present two examples of previous work from the lab.

### 1.5.1 The slope of the phase gradient is predictive of segment size during scaling

The dynamic behaviour of oscillations during scaling of segment size in mouse embryos was explored using the *Luv* Notch signaling reporter [72]. To recapitulate segment scaling, the posterior tip of the tail was cultured on a fibronectin-coated glass slide in a 2D-assay. In this context, there is no growth of the tissue, but segment boundaries eventually start forming around the periphery of the tissue. Therefore, the amount of available PSM gradually shrinks as somite boundaries form. Interestingly, this leads to the formation of progressively smaller somites, but always at a fixed percentage of available PSM. This is reminiscent of the segment scaling which occurs in size reduced embryos as discussed in **section 1.1.1** [12, 13]. To explore how Notch signaling oscillations adapt during segment scaling, period and phase was extracted from live imaging of the *Luv* reporter in segmenting 2D-assays [72]. Oscillations first manifest themselves as a few pulses before the characteristic phase-shifted waves appear. Interestingly, the formation of segment boundaries was only initiated by the time a full wave was present in the PSM. In other words, segmentation coincided with a phase-gradient amplitude of  $2\pi$  along the PSM. Importantly, this phase-gradient amplitude remained constant even as the size of the PSM was reduced. Further, as the size of the remaining oscillatory PSM is reduced by the formation of segments, this was mirrored by a proportional reduction of phase wave velocity. As a result, the phase gradient becomes steeper as the PSM shrinks [72]. Thus, while the phase gradient amplitude remains constant, the phase-gradient slope changes proportionally to segment size. Most importantly, the oscillation phase-gradient was found to be a faithful and early predictor of segment size. This raised the possibility that oscillation dynamics encode information for both time and space.

### 1.5.2 The relative phase-shift between two oscillating pathways can carry positional information

The presence of a period gradient underlies the formation of a phase-shift gradient, which has important conceptual implications for how information can be encoded based on oscillation dynamics. For example, in mouse, both Wnt and Notch signaling oscillates in the PSM, but because Notch signaling oscillations slow down and form a period gradient, they gradually phase-shift relative to Wnt signaling oscillations [137]. Consequently, while Wnt and Notch oscillate out of phase in the posterior PSM, they oscillate in phase in the anterior PSM, where segments form. It follows that the phase shift between these two pathways changes as a function of space, allowing to put forward the hypothesis that phase-shift, or the rhythm

between oscillating pathways, encodes information for segmentation. Recent work in our lab has provided direct experimental evidence for a functional role of relative phase-shift encoding for proper segmentation [137]. Interestingly, the phase-relationship between Wnt and Notch signaling in the PSM can be experimentally controlled by using a microfluidic-based entrainment approach to periodically pulse small-molecule inhibitors and activators of these two pathways [137]. If Wnt and Notch signaling are maintained out of phase, the tissue can be kept oscillating for longer and patterning and segmentation is disrupted. These results illustrate how subtle features of dynamics can be important for developmental patterning, and underscore the need to study these systems using dynamic reporters combined with tailored functional perturbations.

The microfluidic approach outlined above also confirmed that the Wnt and Notch pathways are functionally linked [137]. In other words, when either pathway was targeted, entrainment was observed in both. The molecular mechanism behind this mutual entrainment has not identified yet, although there are several connections between the two Notch and Wnt signaling pathways that could mediate this link. For example, the Notch ligand *Dll1* is regulated by Wnt signaling (but not Notch signaling) in both chick and mouse [78, 142, 143]. As a result, *Dll1* expression is expressed out of phase relative to other Notch signaling oscillations (such as *Hes7*, *Lfng*, and *NICD*), but in phase with Wnt signaling oscillations at both the protein and RNA level [78, 128]. A second link between the two pathways comes in the form of the Wnt antagonist *Nkd*, whose oscillatory expression is also dependent on *Hes7* [126]. Elucidating the underlying mechanistic link between Notch and Wnt signaling oscillations is therefore a subject of future research.



## 2. Aims of the study

Most biological reactions have a strong dependence on temperature. Despite this, developing embryos need to be able to achieve proper growth and patterning in the face of environmental temperature variation. Somitogenesis in vertebrate embryos is known to be regulated by dynamic signals, where spatiotemporal precision is of crucial importance. The overarching aim of this thesis is to take a quantitative approach to explore how the molecular dynamics underlying somite formation adapt to changes in temperature, and how these dynamics are linked to robust patterning. To this end, I study somitogenesis in developing medaka embryos, which have been reported to develop at a wide range of temperatures.

In order to study the functional importance of signaling dynamics, the key challenge is to generate the tools that recapitulate endogenous dynamics and allow quantitative insight in a time-resolved manner. The first aim of this study is therefore to generate medaka endogenous knock-in lines for the Notch, Wnt and FGF signaling pathways to enable the quantification of signaling dynamics in real time. These reporters can then be used to characterise medaka segmentation oscillations and set the baseline for period and phase behaviour in the PSM under standard conditions.

The second aim is to explore how signaling dynamics change in response to changes in temperature. Thus, my goal is to define the temperature range within which robust somite formation can occur in medaka. Within this range, the knock-in reporters can be used as a readout to quantify how dynamic features such as period and phase change with temperature, and which remain constant.

Finally, the insights gained from studying segmentation clock oscillations in medaka can be used to ask how general the principles of dynamic signal encoding are between vertebrate species, from mouse to fish. In the long term, the insights gained from this study will be used to further our understanding of the functional importance of the dynamic aspects of signaling.



### 3. Results - Part I: Establishing medaka as a model to study signaling dynamics

Understanding the dynamics of somitogenesis from a quantitative signaling perspective requires the generation of real-time reporters that accurately reflect the behaviour of native RNA and proteins. To study the interplay between gradients and oscillations during patterning in medaka, I aimed to create high-fidelity fusion protein reporters that would reflect signaling activity in the three major pathways shown to be involved in somitogenesis: Notch, Wnt and FGF. CRISPR-Cas9 was therefore used to generate endogenously tagged reporter lines in the medaka Cab inbred strain. The targeting strategy and donor design for all CRISPR knock-in lines was done in collaboration with Thomas Thumberger from the Wittbrodt lab.

As discussed in section 1.3.5, the *Hes/her* family of transcription factors are thought to be at the core of Notch signaling oscillations in the vertebrate PSM. These oscillations are driven by autoregulatory negative feedback loops which link the Notch and FGF pathways (reviewed in [47]). To quantify Notch signaling oscillations I therefore targeted medaka *her7*, one of three orthologs homologous to mouse *Hes7*. From biochemical studies in zebrafish, *Her7* protein is known to play a dominant role in regulating its own oscillatory behaviour as well as that of other *her* paralogs [95]. While there is evidence for Notch oscillations in the medaka PSM by *in situ* hybridization [65], *Her7* oscillations have never been imaged in real time.

Together with the oscillating clock genes, Wnt signaling gradients in the PSM have been implicated in the control of somite formation in vertebrate embryos [107, 121]. Wnt signaling in the PSM is mediated through the action of  $\beta$ -catenin (*ctnnb1*), and negatively regulated by *axin2*, which also happens to oscillate in the mouse PSM [69, 121]. To study Wnt signaling activity in medaka embryos, I decided to generate reporters for both *Ctnnb1* and *Axin2*. In addition to the Wnt signaling gradient, an FGF signaling gradient controls the position and ability of the PSM tissue to differentiate into somites [54, 108, 109]. The Snail family of transcription factors are regulated by Wnt and FGF, and members of this family are known to oscillate in the PSM of mouse and chick [129]. To study FGF signaling activity, I therefore decided to create a *Snai1a* reporter in medaka [144].

### 3.1 Generation of a medaka Her7 segmentation clock reporter using CRISPR/Cas9

To visualize and quantify oscillatory gene activity in the medaka segmentation clock, I created a fusion protein reporter for Her7. To this end, I used the CRISPR-Cas9 system to insert a GSAGS linker followed by a modified YFP (mVenus, from here on referred to as Venus, [145]) immediately prior to the endogenous stop codon at the 3' end of the *her7* locus (see **figure 5**).

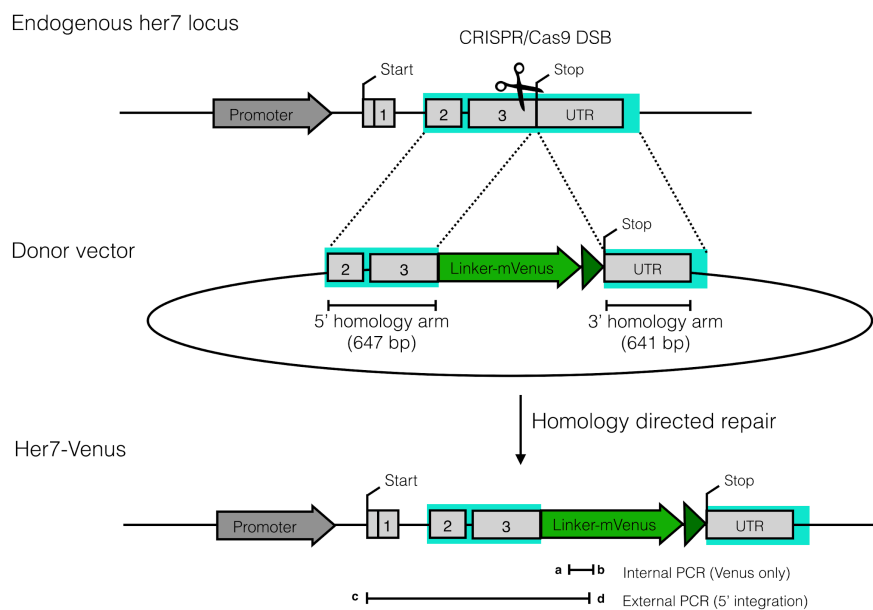


**Figure 5:** Schematic showing the knock-in strategy for mVenus in the endogenous *her7* locus using CRISPR/Cas9 homology directed repair. Homology arms (647 and 641 bp) inserted on either side of the mVenus coding sequence are indicated by blue squares. Screening by PCR targeted either mVenus only (“Internal PCR”) using primers a and b, or the specific 5’ integration (outside the homology arm, “External PCR”) using primers c and d.

To screen a subset of the injected samples, PCR was first done against Venus only (using primers a and b in **figure 5**). To confirm that specific integration had taken place at the *her7* locus, PCR using a primer pair binding outside the 5’ homology arm of the donor construct and inside the Venus sequence was used (hereafter referred to as the 5’ integration band, using primers c and d in **figure 5**). This PCR showed bands of the expected size in 50% of embryos. The remaining embryos were therefore raised to adulthood.

Unlike the results from embryonic DNA, PCR targeting of the 5’ integration band did not give any initial results in any of the 27 adult finclips. This could be due to the fact that the

injected fish are genetic chimeras, where the shorter wildtype locus is more likely to be detected by PCR than the targeted locus. The targeted locus would likely also be present in more copies in DNA extracted from whole embryo as opposed to an adult fin. In addition, the targeted locus turned out to be much longer than expected, as discussed below. For this reason, preliminary screening of potential founders was carried out based on PCR detection of Venus only. Using this approach, 12/27 potential F0 founders were found to be Venus positive, and 6/27 were found to transmit Venus to the germline with an efficiency ranging between 4-50% (summarised in **table 2**).

**Table 2:** Targeting efficiency in Her7-Venus CRISPR knock-in line

	Injected	Raised	Venus +	Germline transmitting (Venus)	Germline transmitting (in-frame integration)
Total nr. of F0	66	27	12	6	1
% of raised F0	-	100%	44%	22%	3.7%
Transmission efficiency				4-50%	9%

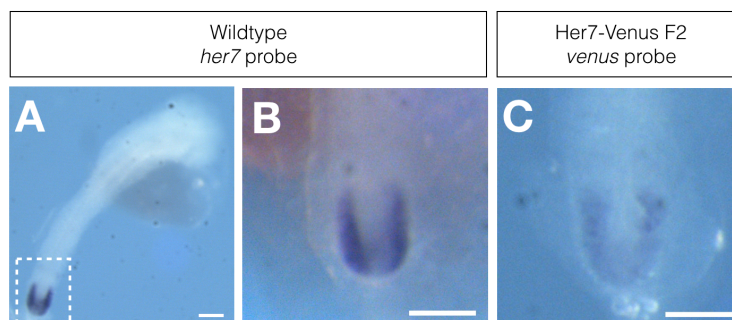


**Figure 6:** Colorimetric *in situ* hybridisation screen used to identify founders for the Her7-Venus line. **(A)** Wildtype medaka embryo at Iwamatsu stage 22 [49] stained with a probe against *her7*. **(B)** Enlarged image of the tailbud corresponding to the region outlined in (A). **(C)** Her7-Venus F2 embryo stained with a probe against Venus. Dorsal view, posterior oriented towards the bottom. Scale bars 100  $\mu$ m.

Due to the weak expression of endogenous *her7*, F2 embryos from several candidate F1s were screened by colorimetric *in situ* hybridisation using a probe against Venus. Using this approach, F2 from 2/15 F1 were found to express Venus RNA in the PSM region (**figure 6c**), with a dynamic expression pattern that reflects endogenous *her7* expression (**figure 6a and b**). Both positive F1 founders originated from the same F0. Despite the fact that Venus was present in 22% of F1 from this F0 founder, the specific Her7-Venus integration was present in only 9% of F1, suggesting that off-target integrations also occurred.

Sequencing the modified locus confirmed the in-frame integration of Venus on the 5' end. However, this also revealed a 3.5 kb extension after the 3'UTR, as shown in **figure 7**. This extended integration matched the donor vector backbone, followed by a region of non-homologous end-joining. However, this unintentional integration does not disrupt the *her7* 3'UTR, as the full 3'UTR sequence was included in the homology arm. Thus, a Her7-Venus fusion protein line with an RNA expression domain that mirrors endogenous *her7* was successfully generated in medaka.

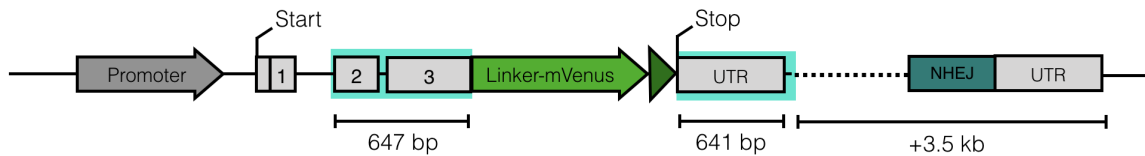


**Figure 7:** Schematic of the Her7-Venus locus. Sequencing revealed a 3.5 kb extension of the locus on the 3' end, where the 3'UTR in the homology arm was integrated together with the rest of the donor backbone (dotted line) and a region of non-homologous end-joining (NHEJ), before the endogenous UTR.

### 3.1.1 Validation of the Her7-Venus line

To evaluate whether the endogenous knock-in of Venus resulted in a functional protein, the Her7-Venus line was bred to homozygosity. If the knock-in of Venus were to significantly perturb protein function, we would expect to see a phenotype at the level of signaling dynamics or somite number and morphology in homozygotes. In contrast, Her7-Venus embryos are largely normal at early developmental stages (compare **figure 8a**). When synchronized from fertilisation, Her7-Venus embryos reach Iwamatsu stage 22 (9-10 somite stage), at the same time as wildtype controls, with comparable somite sizes (mean  $33.5 \pm 3.26 \mu\text{m}$  ( $n=65$ ) and  $34.2 \pm 4.08 \mu\text{m}$  ( $n=73$ ) respectively, see **figure 8b**). PSM pre-patterning, as scored by expression of *mesogenin* (a Wnt-regulated bHLH transcription factor involved in PSM patterning, [57]) and *myf5* (a posterior somite polarity marker, [57]) is also normal in Her7-Venus homozygotes relative to wildtype controls (**figure 8c** and **figure 8d**).

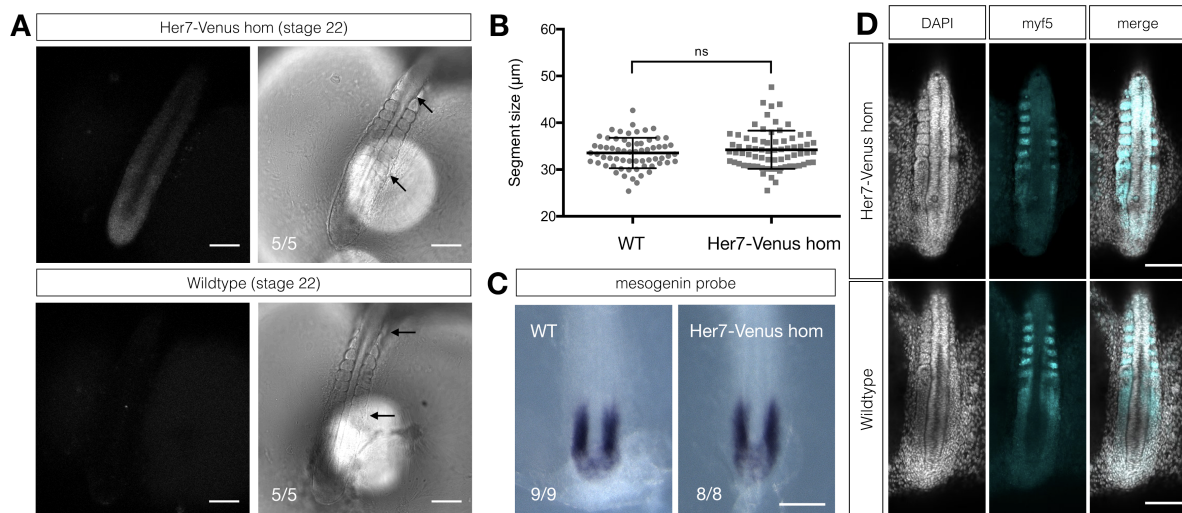


**Figure 8:** (A) Her7-Venus homozygote embryo with characteristic U-shaped expression of fusion protein in the PSM. Embryos do not show obvious developmental defects, and form the same number of somites as wildtype controls when synchronized until Iwamatsu stage 22 ( $n = 5$  per group). Black arrows mark first and last somite formed. (B) Somite size is not significantly different between wildtype and Her7-Venus homozygotes (mean somite size  $33.5 \pm 3.26 \mu\text{m}$  and  $34.2 \pm 4.08 \mu\text{m}$  respectively). Significance calculated by unpaired t-test,  $N=2$ ,  $n=65$ ,  $73$ . (C) *In situ* hybridisation using a mesogenin probe shows normal PSM patterning in Her7-Venus homozygotes relative to wildtype,  $N = 1$ ,  $n = 9$ ,  $8$ . (D) *In situ* hybridisation chain reaction using a myf5 probe shows normal somite patterning in Her7-Venus homozygotes relative to wildtype,  $N = 1$ ,  $n = 5$ ,  $3$ . Dorsal view, posterior oriented towards the bottom. Scale bars  $100 \mu\text{m}$ .

To study whether the patterning of somite derivatives is normal in Her7-Venus hatchlings, the morphology and number of segmented vertebrae was assessed by skeletal staining (**figure 9**). The results of this analysis showed that although they form a similar number of segments relative to wildtype hatchlings ( $30.8 \pm 0.753$  ( $n=6$ ) and  $31.4 \pm 0.787$  ( $n=7$ ) segments respectively, **figure 9c**), 67% of Her7-Venus homozygotes have a phenotype in the last segments of the vertebral column (**figure 9a**). In those homozygous Her7-Venus hatchlings where defects are apparent, at least 14-23 regular segments form before segment boundaries become fused and irregular. Furthermore, the average axis length (measured from the base of the skull to the start of the tailbone) is reduced in Her7-Venus homozygotes, measuring an average of  $2.87 \pm 0.255$  mm ( $n=6$ ) relative to wildtype controls which have an average length of  $3.22 \pm 0.129$  mm ( $n=7$ ) (**figure 9b**).

Together, this suggests that while somitogenesis is not significantly affected by the Her7-Venus fusion protein in early embryos until 9-10 somite stage, somite derivatives do seem to accumulate a phenotype towards the later stages of segmentation.

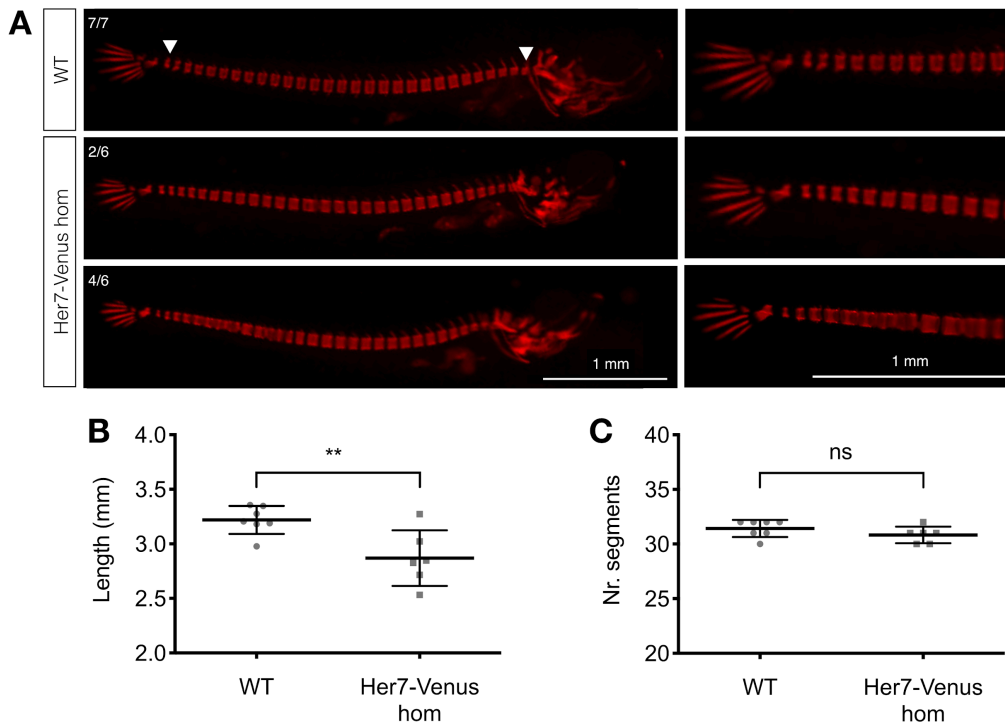


**Figure 9:** (A) Skeletal staining with alizarin red at 15 dpf reveals accumulation of segmentation defects in Her7-Venus homozygous hatchlings relative to wildtype controls. Panels on the right show closeup of hatchling tails on the left. Lateral view, posterior oriented towards the left. (B) Quantification of hatchling length (from the base of the skull to the start of the tail-bone, between white arrowheads) shows wildtype controls are longer than Her7-Venus homozygotes, with mean length  $3.22 \pm 0.129$  mm and  $2.87 \pm 0.255$  mm respectively. (C) Quantification of number of segments per hatchling shows that wildtype and Her7-Venus homozygotes form a similar number of segments, with  $31.4 \pm 0.787$  and  $30.8 \pm 0.753$  segments respectively. Significance calculated by unpaired t-test  $N=1, n=7, 6$  (\*\* =  $P \leq 0.01$ ).

### 3.1.2 Generation of a *her7* knockout line

The lack of a strong developmental phenotype in Her7-Venus homozygotes could indicate the presence of a functional fusion protein. However, it is possible that the *her7* paralogs *her5* and *her1/11* compensate for any loss of *her7* function. In support of this idea, there is some evidence that the *her7* and *her1/11* orthologs in zebrafish are partially redundant [64, 93, 97]. To further evaluate the impact of endogenously tagging Her7 in the Her7-Venus line and study whether functional *her7* is at all necessary for normal segmentation, a knockout line was created using CRISPR/Cas9.

Genetic knockout of members of Hes7 has been previously carried out in mouse, where the coding sequence after the first exon was replaced by the LacZ sequence [89]. The

region that was replaced contains most of the bHLH domain, which mediates DNA binding and dimerization [87]. Following the same strategy, a medaka *her7* knockout line was created using two sgRNAs designed to target either side of the basic helix-loop-helix (bHLH) domain (figure 10a).

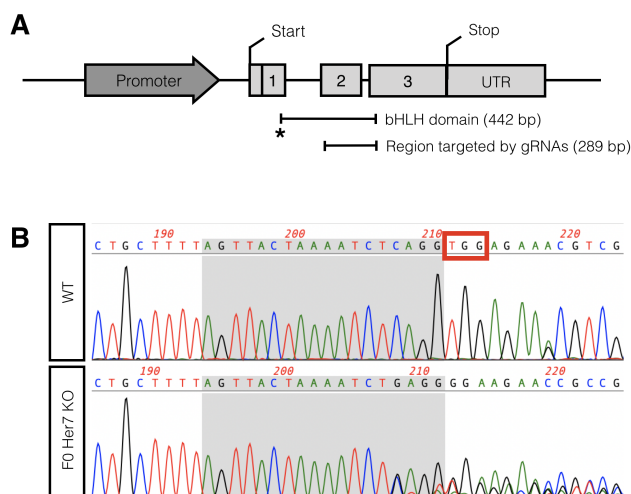


**Figure 10:** Design of a *her7* knockout line **(A)** Schematic of the *her7* locus, with the bHLH domain spanning all 3 exons (translating to 57 amino acids in the protein). This domain is required for DNA binding and dimerisation in members of the Hes/*her* transcription factor family (reviewed in Kageyama, development 2007). **(B)** Sequencing data from wildtype embryos (above) and F0 embryos injected with sgRNAs (below). sgRNA sequence in exon 1 highlighted in gray (corresponding to the position marked with an asterisk in A), PAM (TGG) outlined in red box. Note the appearance of multiple sequencing peaks starting 4 bp upstream of the PAM site, indicating the presence of different template sequences which would result from a CRISPR/Cas9-mediated disruption of the locus at this position.

Embryos subjected to *her7* CRISPR knockout showed morphological defects in somite formation already in the injected generation, ranging from relatively normal somites (figure 11a') to left-right asymmetry and a delayed somite formation (figure 11b') to a severe lack of somites and the entire axis below the head (figure 11c'). Except for some of the severely affected embryos, the morphology of the head was in most cases relatively normal. 11/36 injected embryos did not survive to hatching, and were therefore sacrificed for PCR screening. Of these embryos, 45.5% showed deletions ranging from 200-300 bp, and sequencing confirmed that cutting had occurred specifically around the sgRNA sites (figure 10b).

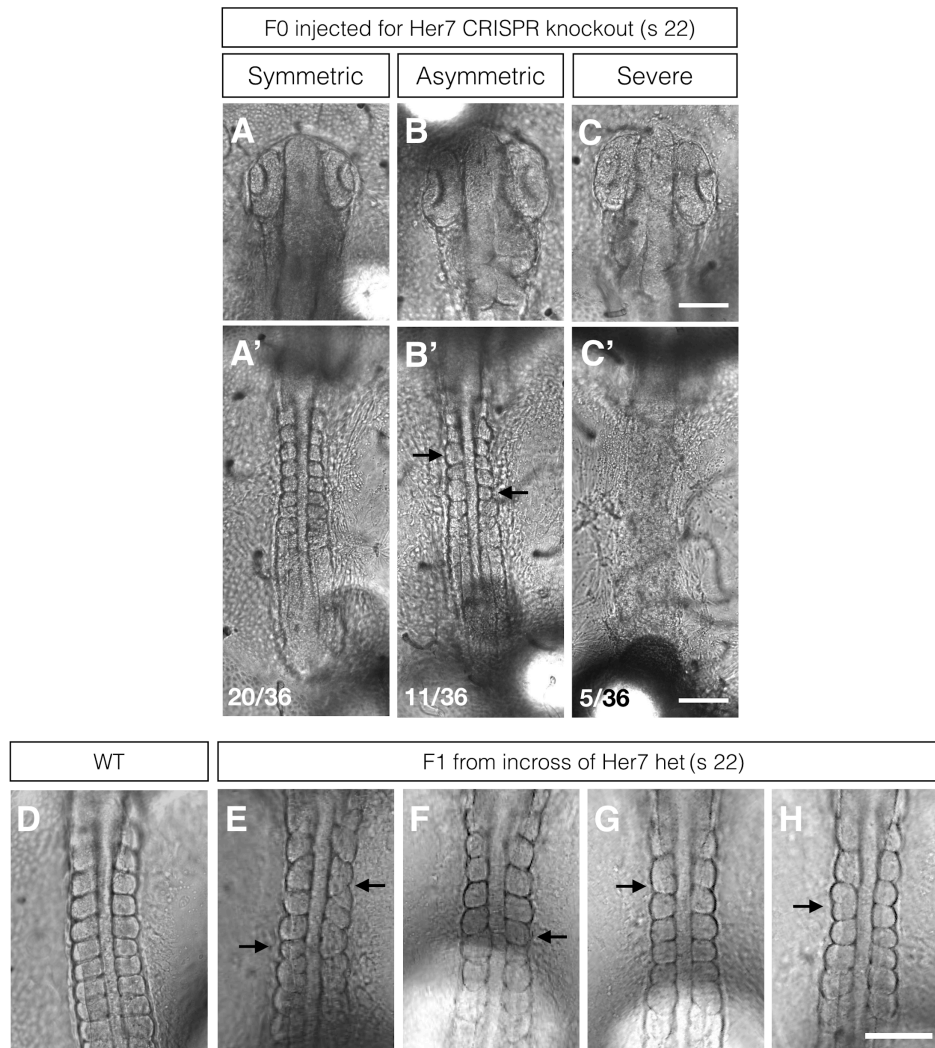


**Figure 11:** *her7* CRISPR knockout line. (A-C) Phenotype in injected F0 embryos, ranging from relatively normal somites to somite asymmetry and severe axis disruption. (E-H) Phenotype in F1 embryos from an incross of *her7* knockout heterozygotes, including fused somites and left-right asymmetry compared to wildtype in (D). Embryos at Iwamatsu stage 22. Dorsal view, posterior oriented towards the bottom. Scale bars 100  $\mu$ m.

Screening of the raised, injected F0 generation by PCR showed that 39% had a heterozygous deletion of approximately 300 bp around the bHLH domain. Among these, six were found to give germline transmission to F1 varying between 4-57% (**table 3**). Three founders were chosen for their high germline transmission (specified in **table 4**), and sequencing of these confirmed the presence of deletions spanning between 206-274 bp. Screening of the F1 generation from these founders showed the same phenotype as observed in the F0, (**figure 11e-h**) with defects including fused somites and left-right asymmetry.

**Table 3:** Targeting efficiency for *her7* CRISPR knockout line

	Injected	Raised	Deletion +	Germline transmission to F1
Total nr. F0	36	22	9	4-57%
% of raised F0	-	100%	41%	-

Sequencing of F1 founders revealed three different deletions of the bHLH region (**figure 12**). The wildtype protein sequence is 201 amino acids long, 57 of which belong to the bHLH domain. CRISPR knockout caused deletions ranging from 206-274 base pairs, resulting in truncations from premature stop codons in all three cases (shown as asterisks in **figure 12**). The lines originating from F0 number 24 and 33 had the most extensive deletions, retaining only the first 17-19 amino acids, 4-6 of which form part of the bHLH domain, respectively. In the case of line 24, a five-base pair insertion preceded the deletion. The line from F0 number 33 had a smaller deletion, with 39 amino acids retained from the original sequence, 27 of which form part of the bHLH domain, as summarized in **table 4**. In all cases, all F1 coming from the same F0 had the same deletion, and homozygous embryos from different lines did not survive until hatching, nor visibly differed in their phenotype (data not shown).

**Table 4:** Summary of modifications to the *her7* locus following CRISPR knockout for each of the three F0 lines.

Line	Total length protein (amino acids)	Total length cDNA (bp)	Length of deletion gDNA/cDNA (bp)	Amino acids retained from original sequence	Amino acids retained from bHLH domain	Germline transmission
WT	201	606	-	-	57	-
F0 24	60	413	269/188 + 5bp insertion	17	4	36%
F0 33	60	418	269/188	19	6	21%
F0 29	81	481	206/125	39	27	43%

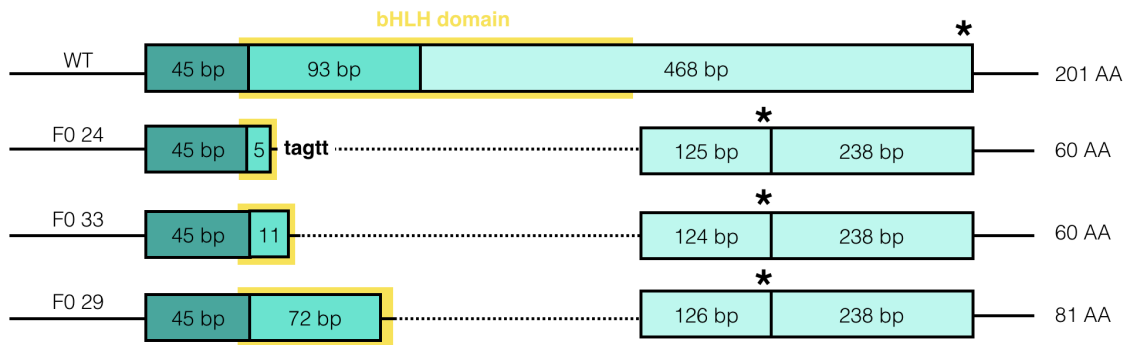


**Figure 12:** Characterisation of *her7* knockout lines. Sequencing revealed three different deletions in the three F0 that gave rise to the lines. The three *her7* codons (45, 93 and 468 bp in wildtype) are shown in different shades of blue. The bHLH domain (57 amino acids long) is shown in yellow. Stop codons are labeled with an asterisk. Total length of amino acid (AA) sequence specified on the right hand side.

### 3.1.3 Characterisation of the *her7* knockout phenotype at the molecular level

To confirm the absence of *her7* transcript and examine whether somite anterior-posterior polarity was affected in the phenotype of the *her7* knockout lines, two-color *in situ* hybridisation was carried out between wildtype and mutant siblings. To this end, heterozygous carriers were crossed and the resulting embryos were stained with RNA probes against *myf5* and *her7*. *myf5* codes for a bHLH transcription factor involved in myogenesis which marks the posterior half of each somite [57, 146]. Wildtype stage-matched embryos show a range of *her7* expression patterns that reflect the oscillatory nature of this gene (oscillatory phases labeled I-IV in **figure 13**). As shown in **figure 13**, when heterozygous fish from lines 24 and 33 were crossed together, 15/22 (68%) embryos show regular *myf5* staining and *her7* oscillations. In contrast, the remaining 7 (32%) embryos have smeared *myf5* staining in all somites, and no observable *her7* expression in the PSM. Assuming that those embryos with loss of *her7* expression are homozygous knockouts, this data indicates a loss of somite polarity along the entire axis in 9-10 somite stage mutant embryos.

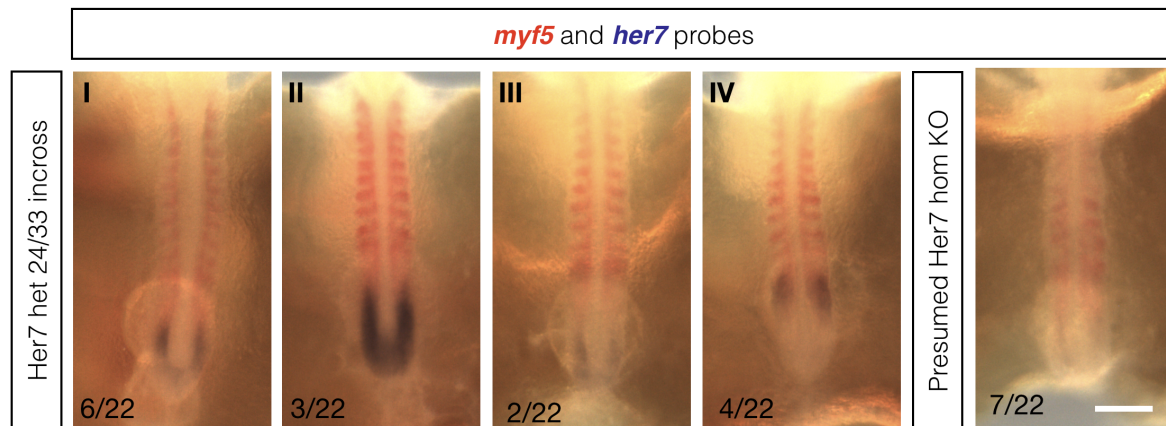


**Figure 13:** Double colorimetric *in situ* hybridisation in embryos from incross of *her7* heterozygotes from line 33 and line 24. Expression patterns were analyzed using fluorescein-labeled *myf5* probe (stain in red) and dig-labeled *her7* probe (stain in blue). While the majority of embryos show the expected expression pattern of *her7* with different wave phases labeled I-IV, 7/22 embryos show loss of correct somite patterning and *her7* expression (last panel). Embryos at Iwamatsu stage 22. Dorsal view, posterior oriented towards the bottom. Scale bar 100  $\mu$ m.

It is known that Her7 and its paralogs heterodimerize and repress their own expression in zebrafish [95]. The corresponding orthologs in medaka, Her7, Her5 and Her1/11 [65], also show oscillatory expression at the RNA level. To find out if other paralogs are still oscillating in the absence of Her7, double *in situ* hybridisation for *myf5* and *her1/11* was performed in offspring from an incross of *her7* heterozygotes from lines 24 and 33 (**figure 14a**) and line 29 (**figure 14b**). In this case, the majority of embryos (12/18 and 8/16 embryos in 10a and 10b respectively) again showed regular *myf5* staining, and - as expected from an oscillatory gene - *her1/11* cycles between different phases of gene expression (compare panels I-IV in figure 14a and 10b to wt expression in figure 14c, panel I-III). Interestingly, in those embryos where *myf5* staining was smeared, *her1/11* was no longer dynamic, and appeared upregulated throughout the *her1/11* expression domain (9/35 and 8/16 embryos for the incross of *her7* heterozygotes from lines 24/33 and line 29 respectively). This demonstrates that *her7* can regulate the oscillatory expression of its paralog *her1/11*.

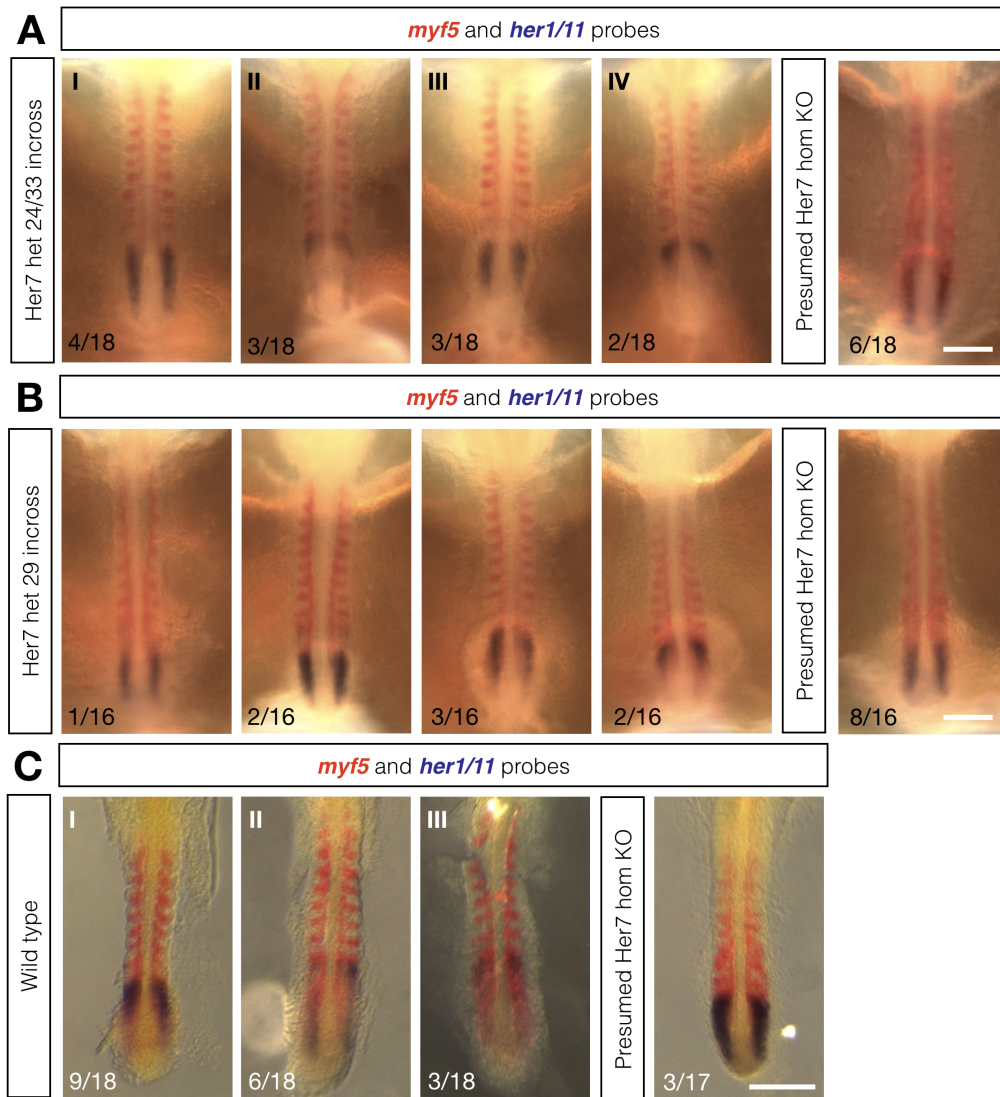


**Figure 14:** Double colorimetric *in situ* hybridisation in embryos from incross of fish heterozygous for *her7* knockout. Expression patterns were analyzed using fluorescein-labeled *myf5* probe (stain in red) and dig-labeled *her1/11* probes (stain in blue). Each column labeled I-IV shows the different wave phases within each group of embryos. **(A)** Embryos from incross of *her7* heterozygotes from line 33 and line 24. N = 2, n = 18, 17. **(B)** Embryos from incross of *her7* heterozygotes from incross of line 29. N = 1, n = 16. **(C)** Flat-mounted samples of wildtype embryos, for comparison, and a *her7* knockout embryos from incross of line 33 and 24. Embryos at Iwamatsu stage 22 (10 somites). Dorsal view, posterior oriented towards the bottom. Scale bar 100  $\mu$ m.

### 3.1.4 Characterisation of *her7* expression dynamics in the Her7-Venus line

To compare the dynamics of *her7* RNA expression between wildtype and Her7-Venus embryos, a colorimetric *in situ* hybridisation was carried out using exonic probes against both *her7* and *venus* sequences. As shown above, stage-matched embryos show a range of *her7* expression patterns, which can be sorted into wave phases (labeled I-IV in **figure 15**). However, while the range of *her7* expression patterns in wildtype and Her7-Venus heterozygotes were comparable, the expression levels were strikingly reduced in Her7-Venus homozygotes relative to wildtype (**figure 15a**). As expected, the expression of *venus* RNA was higher in Her7-Venus homozygotes relative to Her7-Venus heterozygotes, where *venus* expression is barely visible (**figure 15b**).

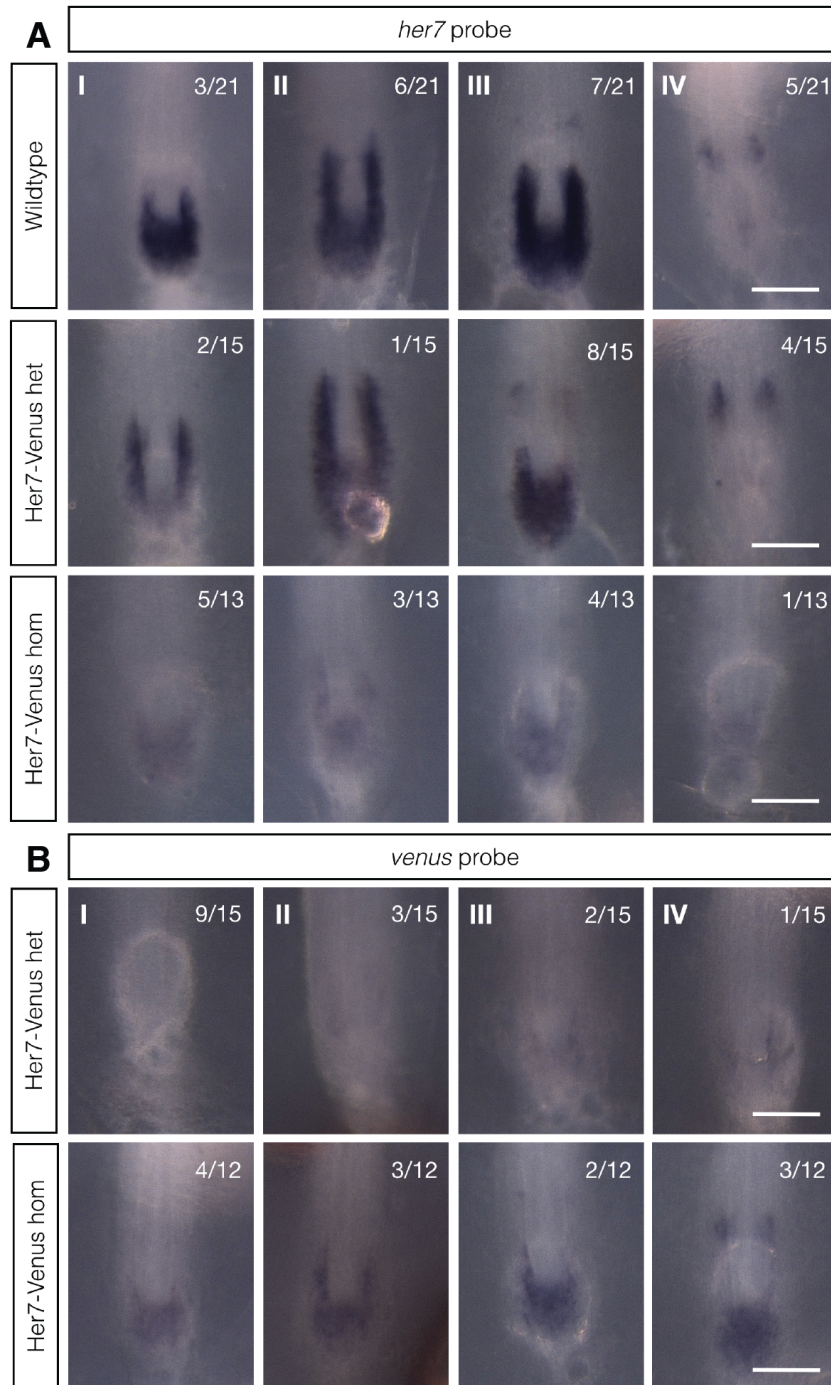


**Figure 15:** *In situ* hybridization with an RNA probe against *her7* (A) and *venus* (B) in wildtype (top row), Her7-Venus heterozygotes (middle row) and Her7-Venus homozygotes (bottom row). Dynamic expression of these genes is illustrated by showing four embryos for each group. Each column shows the different wave phases within each group of embryos, labeled I-IV. *Her7* expression is strongly reduced in Her7-Venus homozygotes. N = 2, n = 41, 28, 30 for *her7* stain in wildtype, Her7-Venus heterozygotes and Her7-Venus homozygotes respectively, N = 2, n = 15, 22 for *venus* stain in Her7-Venus heterozygotes and Her7-Venus homozygotes respectively. Embryos at Iwamatsu stage 22. Dorsal view, posterior oriented towards the bottom. Scale bars 100  $\mu$ m.

From the molecular analysis of the *her7* knockout line (**figure 14**) we know that *her7* can regulate *her1/11* expression. To test if the downregulation of *her7* expression in the Her7-Venus line would have any effect on the *her7* paralogs, expression of *her5* and *her1/11* was verified by *in situ* hybridisation (**figure 16**). These results showed that the oscillatory expression of both *her5* and *her1/11* in Her7-Venus heterozygotes and homozygotes was comparable in intensity to wildtype embryos.

Thus, while *her7* RNA is strongly downregulated in Her7-Venus homozygotes, the expression of its paralogs *her5* and *her1/11* is not affected. Knowing that the loss of *her7* leads to the upregulation of *her1/11* in the *her7* knockout, this result argues against any significant loss of function of the Her7 protein in the Her7-Venus line.

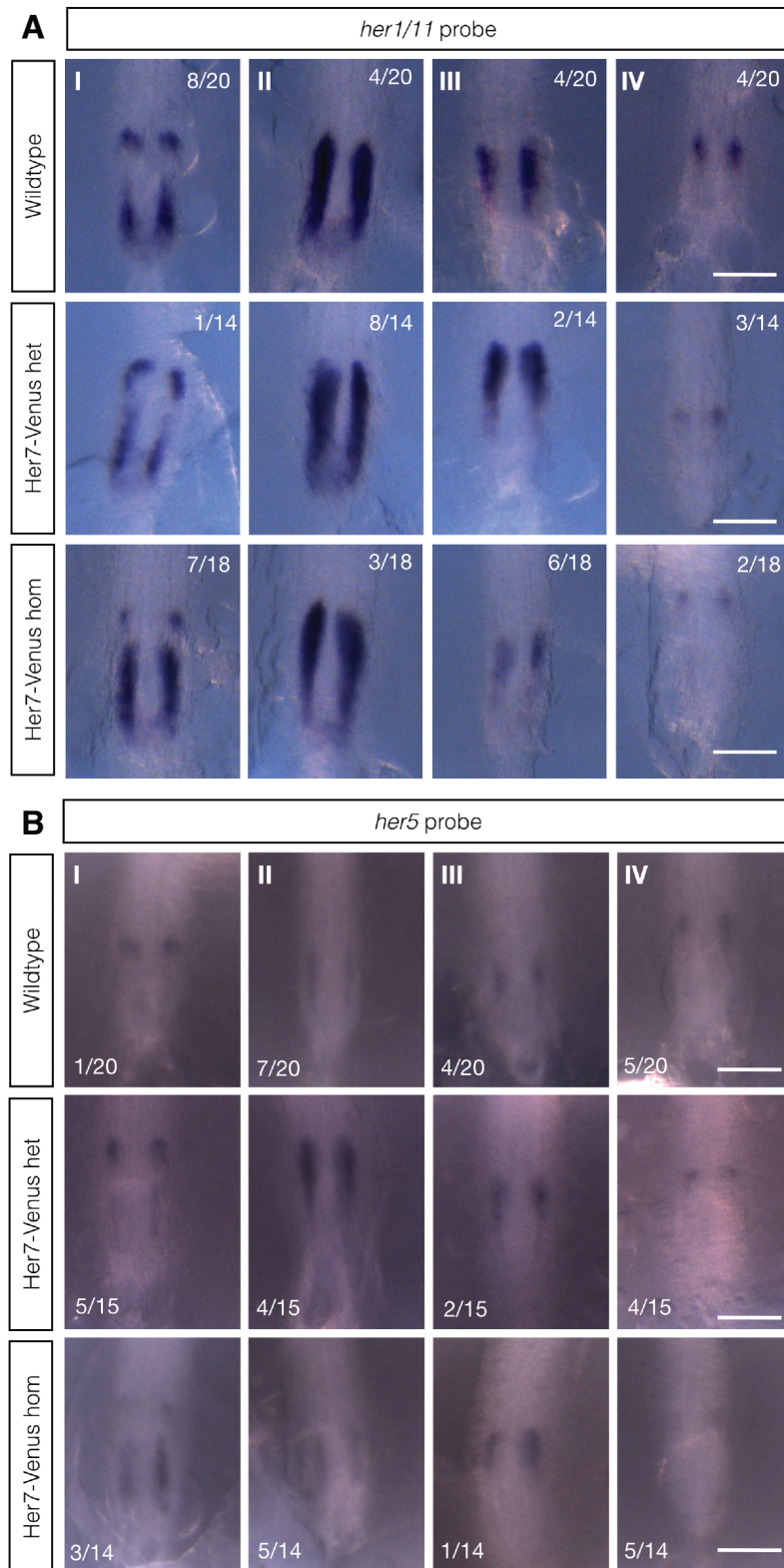


**Figure 16:** *In situ* hybridization with an RNA probe against **(A)** *her5* and **(B)** *her1/11* in wildtype (top row), Her7-Venus heterozygotes (middle row) and Her7-Venus homozygotes (bottom row). Dynamic expression of these genes is illustrated by showing four embryos for each group. Each column shows the different wave phases within each group of embryos, labeled I-IV. N = 1, n = 20, 14, 18 for *her1/11* and n = 20, 15, 14 for *her5*. Embryos at Iwamatsu stage 22 (10 somites). Dorsal view, posterior oriented towards the bottom. Scale bar 100  $\mu$ m.

### 3.1.5 Removal of the integrated donor backbone in the Her7-Venus line

The strong downregulation of *her7* mRNA expression in the Her7-Venus line (**figure 15**) could be related to the unintentional integration of the donor plasmid backbone, which extended the locus by 3.5 kb. In order to see if the integrated donor backbone has an effect on expression levels, CRISPR/Cas9 was used to knock out the inserted sequences extending from the 3'UTR. Two sgRNAs were tested, as summarized in **table 5**.

Through PCR screening from adult finclips, 11 founders were identified with bands of the expected size for a perfect integration of Venus in the *her7* locus (summarised in **table 5**). To test whether the expression of Her7-Venus was increased in these embryos, three founders were selected for their high germline transmission, and *in situ* hybridization with probes against *her7* was carried out. In the original Her7-Venus line (from here on referred to as Her7-Venus1), *venus* expression is barely visible in the PSM of heterozygotes (**figure 17b**), even after extensive staining. Strikingly, about 25% of embryos from the founders positive for the backbone knockout showed expression of *venus* that was comparable to that of Her7-Venus1 homozygotes (**figure 17b**, compare to **figure 15b**). These founders were used to propagate a second Her7-Venus line, from here on referred to as Her7-Venus2.

**Table 5:** Targeting efficiency for CRISPR donor backbone knockout in Her7-Venus1 line

sgRNA injected		Injected	Raised	Deletion +	Germline transmission to F1
T11	Total nr. of F0	35	17	6	N/A
	% of raised F0	-	100%	35%	-
T12	Total nr. of F0	21	16	11	38-53%
	% of raised F0	-	100%	69%	-

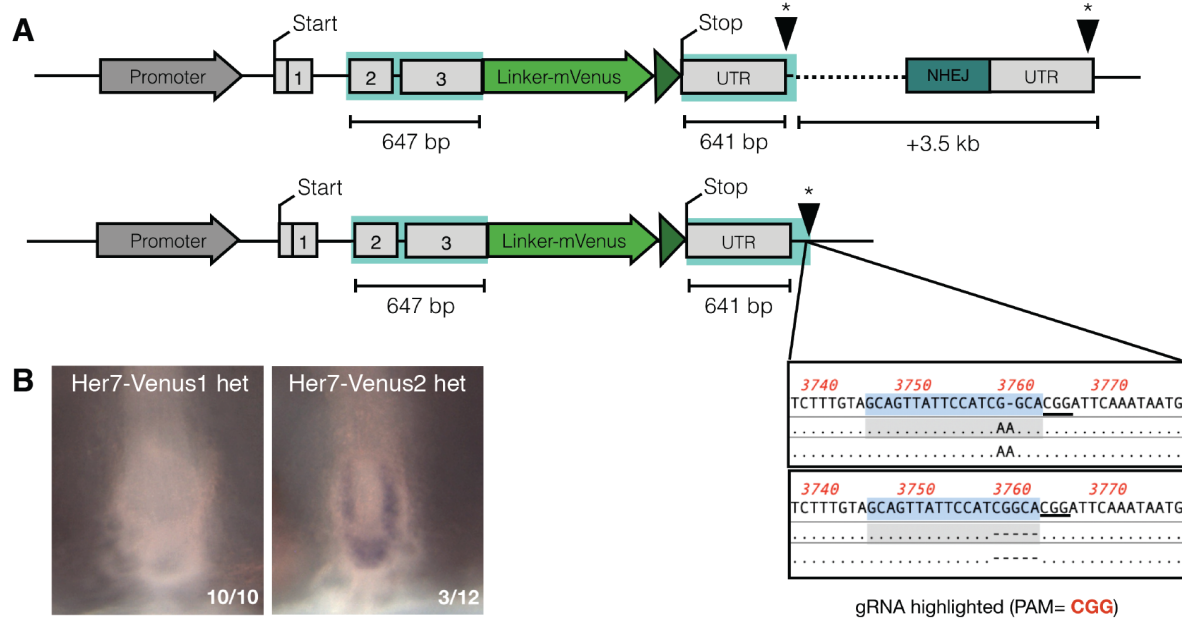


**Figure 17:** Removal of donor backbone from the Her7-Venus1 line **(A)** Schematic of donor backbone knockout, with T12 sgRNA target site indicated by black arrowheads marked with an asterisk. Successful knockout of the donor backbone resulted in either a SNP and single insertion or a 5 bp deletion close to the PAM site. **(B)** *In situ* hybridization using a probe against *venus* in Her7-Venus heterozygous embryos. Images show expression levels before (left) and after (right) CRISPR knockout of the integrated donor backbone. Embryos at Iwamatsu stage 22. Dorsal view, posterior oriented towards the bottom.

To evaluate how this increased expression in Her7-Venus2 translates at the protein level, live imaging of homozygous and heterozygous tails (described in more detail in **section 4.1.1**) with and without the additional backbone knockout was performed. Analysis of this data showed that mean signal intensity is increased where the donor backbone was removed in both heterozygotes and homozygotes by about 1.3 fold (**figure 18**).

Thus, CRISPR-mediated removal of integrated donor backbone did result in an increase in the expression of Her7-Venus. Therefore, the Her7-Venus1 line could be considered a hypomorph when it comes to *her7* expression. It remains to be tested whether this increase in expression at the RNA and protein level has an effect on the phenotype of mature segments shown in **figure 9**.

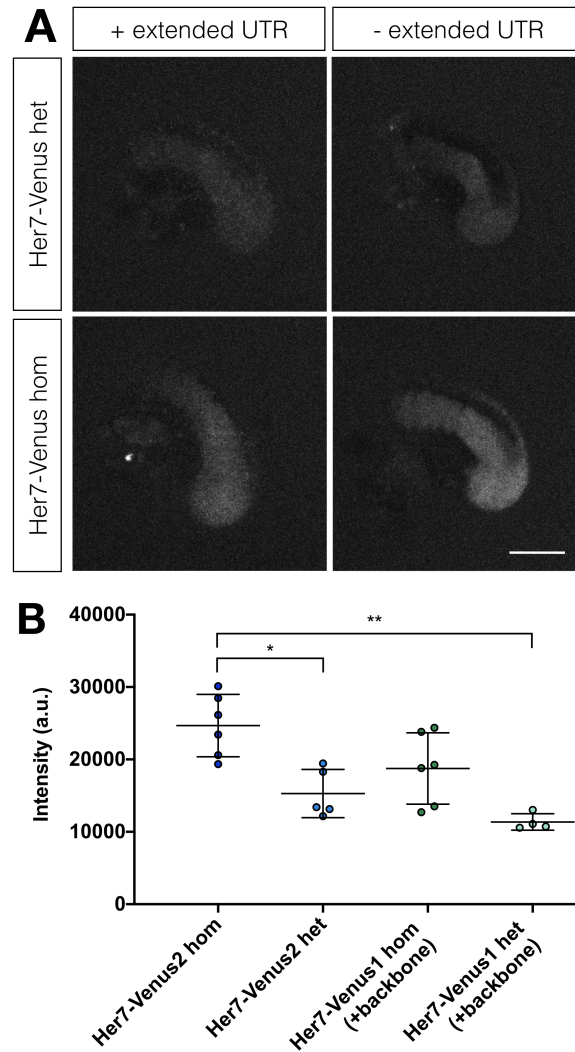


**Figure 18:** Mean signal intensity of Her7-Venus after backbone removal **(A)** Maximum projection of cultured tail explants before and after donor backbone removal **(B)** Quantification of signal intensity by averaging from 10 hour imaging time-series. For samples without the extended backbone, mean intensity is  $24682 \pm 4307$ ,  $15289 \pm 3234$ ,  $N = 2$ ,  $n = 6$ ,  $5$  for Her7-Venus 2 homozygotes and heterozygotes respectively. For samples with the extended backbone mean intensity is  $18745 \pm 4926$  and  $11356 \pm 1139$ ,  $N = 2$ ,  $n = 6$ ,  $4$  for Her7-Venus homozygotes and heterozygotes (with extended UTR) respectively. Lateral view, posterior oriented towards the bottom. Scale bar  $100 \mu\text{m}$ .

## 3.2 Generation of medaka Wnt and FGF signaling reporters using CRISPR/Cas9

### 3.2.1 Generation of Ctnnb1-Venus and Axin2.1-Venus knock-in lines

To visualize Wnt signaling dynamics in medaka embryos, CRISPR/Cas9 was used to target *ctnnb1* and *axin2*. While there is only one *ctnnb1* in the medaka genome, there are two versions of *axin2*, one on chromosome 1 (*axin2.1*) and the other on chromosome 8 (*axin2.2*). Expression of *ctnnb1* RNA can be detected along the whole axis, with the highest levels in the head, somites and posterior tailbud (**figure 19a**). The RNA expression patterns of *axin2.1* and *axin2.2* are very similar, also peaking in the head and posterior tailbud, although *axin2.2* seems to be weaker (**figure 19b** and **figure 19c**). Due to the stronger expression levels I decided to target Axin2.1.

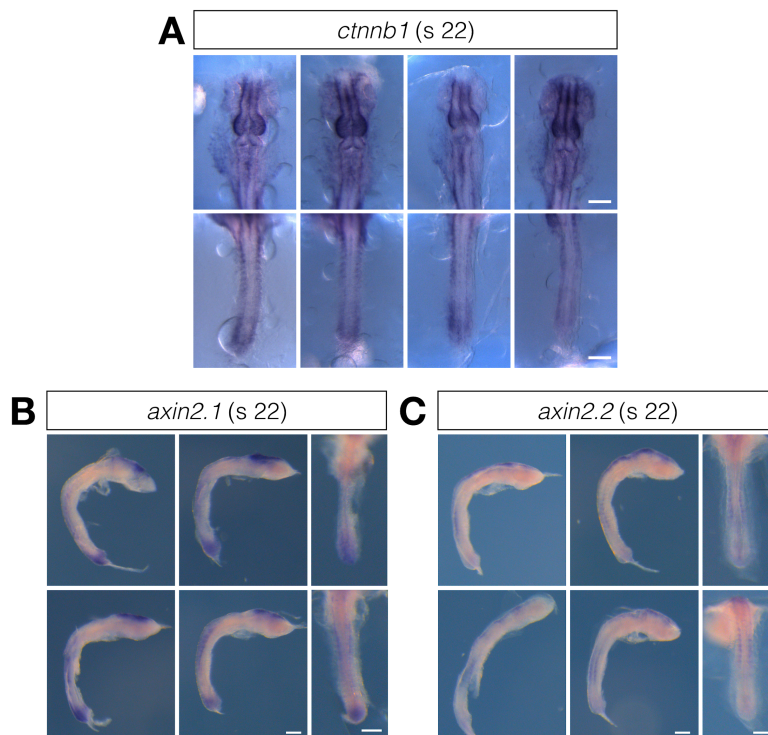
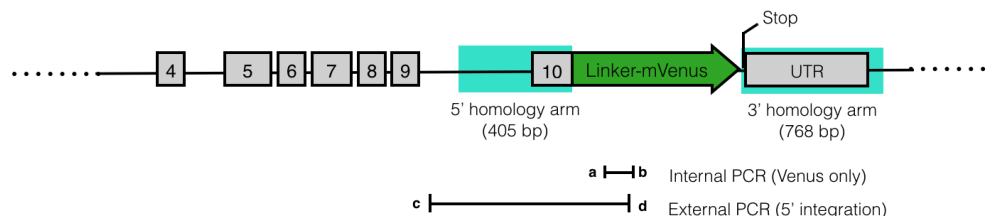


**Figure 19:** Colorimetric *in situ* hybridisation of Wnt components **(A)** *ctnnb1* **(B)** *axin2.1* and **(C)** *axin2.2* in wildtype medaka embryos at Iwamatsu stage 22. Dorsal and lateral view, posterior oriented towards the bottom. Scale bars 100  $\mu\text{m}$ .

Following the same strategy as for the Her7-Venus line, a knock-in strategy was designed to endogenously tag the Ctnnb1 and Axin2.1 proteins with a linker-Venus at the 3' end of the coding sequence (**figure 20**). Integration efficiency is summarized in **table 6**. To

visualize protein expression in these knock-in lines, imaging was done using a confocal microscope (**figure 21** and **figure 22**). Fluorescence levels in both lines are graded in the PSM, as quantified in **figure 21c** and **figure 22b**. Ctnnb1-Venus can also be detected in the somites and more generally on cell membranes, as well as in the head.

### A Axin2.1-Venus



### B Ctnnb1-Venus

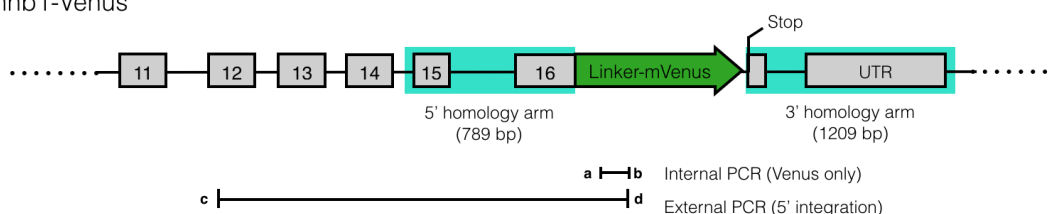


**Figure 20:** Schematic outlining targeting strategy for Wnt-signaling reporters **(A)** *axin2.1* (on chromosome 1) and **(B)** *ctnnb1*. Homology arms outlined in blue. Screening by PCR targeted either Venus only (“Internal PCR”) using primers a and b, or the specific 5’ integration (outside the homology arm, “External PCR”) using primers c and d.

**Table 6:** Targeting efficiency in the Ctnnb1-Venus and Axin2.1-Venus CRISPR knock-in lines

Line		Injected	Raised	Venus +	5' integration +	Germline transmission to F1 (Venus)	Germline transmission to F1 (5' integration)
Ctnnb1-Venus	Total nr. F0	29	14	2	2 (only 1 was fertile)	-	4/32 (12.5%)
	% of raised F0		100%	14%	14%	-	-
Axin2.1-Venus	Total nr. F0	42	14	2	2	12/12 (100%)	5/12 (42%)
						27/34 (79%)	0/34 (0%)
	% of raised F0		100%	14%	14%	-	-

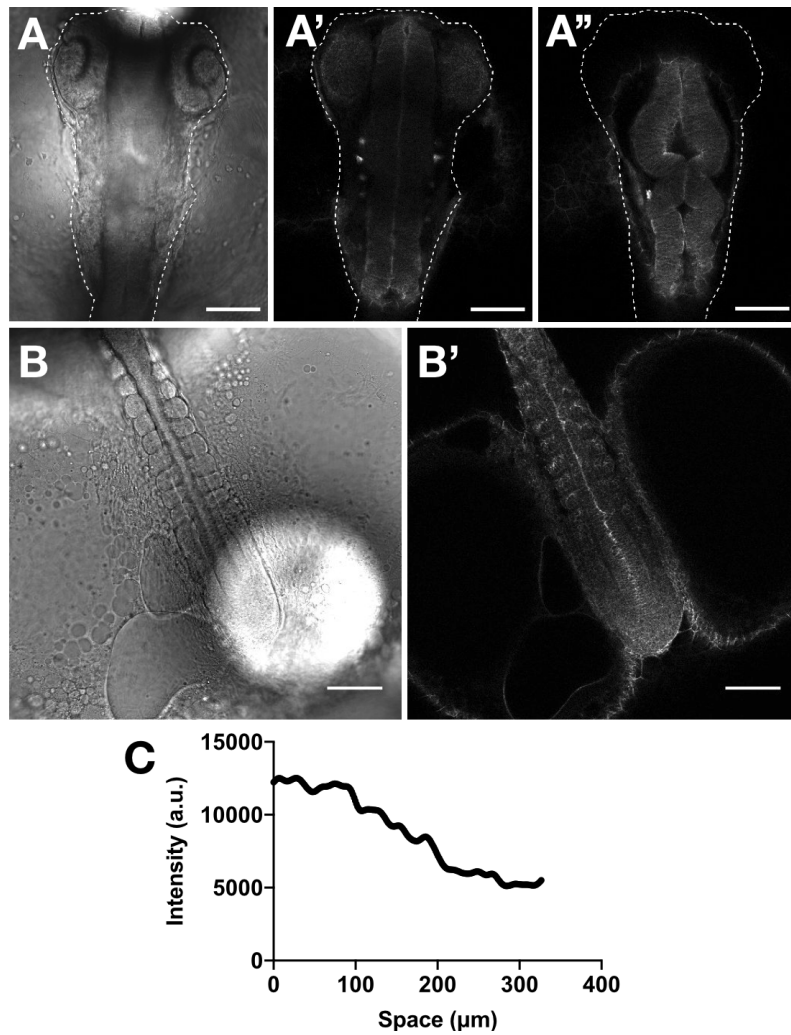


**Figure 21:** The Ctnnb1-Venus knock in line. **(A)** Expression of Ctnnb1-Venus in the head of medaka embryos at stage 22. **(A')** and **(A'')** show expression in deeper z-planes. **(B)** Expression along the axis and tailbud in a single z-plane. **(C)** Intensity profile measured using a 20 pixel-wide line drawn from last visible somite boundary until the tailbud of the embryo in **(B)** shows the Ctnnb1-Venus gradient in space, from posterior to anterior (posterior set to 0). Dorsal view, posterior oriented towards the bottom. Scale bars 100 μm.

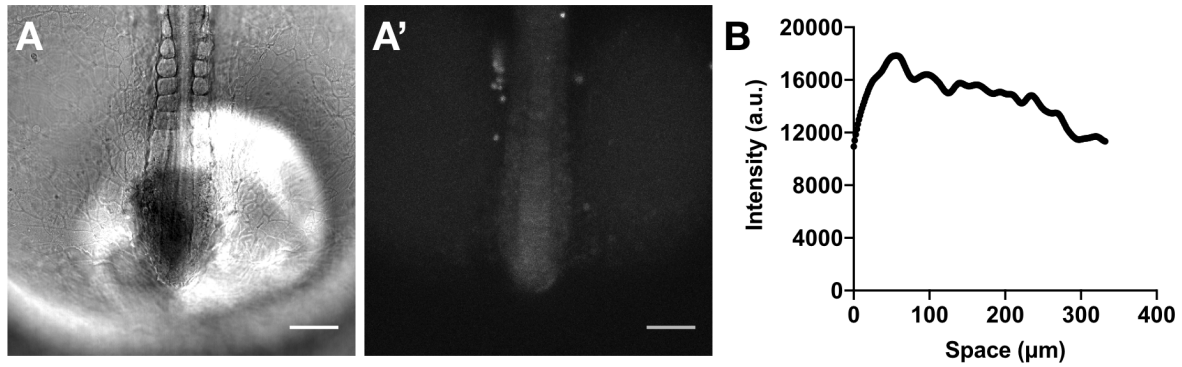


**Figure 22:** The Axin2.1-Venus knock-in line. **(A)** Expression in the PSM from maximum projection. **(B)** Intensity profile of a 20-pixel wide line drawn along the PSM, from last visible somite boundary until the tailbud of the embryo in **(A)** shows the Axin2-Venus gradient in space, from posterior to anterior (posterior set to 0). Dorsal view, posterior oriented towards the bottom. Scale bars 100 μm.

### 3.2.2 Generation of a Snai1a-Venus knock-in line

To visualize FGF signaling dynamics in medaka embryos, CRISPR/Cas9 was used to target *snai1a*. In medaka, there are three *snai* orthologs, *snai1a*, *snai1b* and *snai2*. Among these, only *snai1a* and *snai2* are expressed in the PSM [144]. While *snai2* is only expressed in the anterior PSM, *snai1a* is expressed in a U-shaped domain, with a graded distribution from posterior to anterior (**figure 23**).

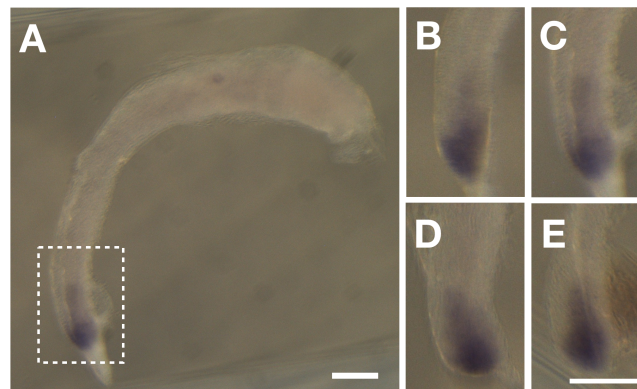


**Figure 23:** Colorimetric *in situ* hybridisation of the FGF target *snai1a*. **(A)** Whole view of embryo, note staining is also present just behind the head. **(B-E)** Magnified view corresponding to outlined region in **(A)** shows the posterior PSM from four different stage-matched embryos, where staining appears slightly variable between samples. Lateral view, posterior oriented towards the bottom. Scale bars 100 μm.

## Snai1a-Venus

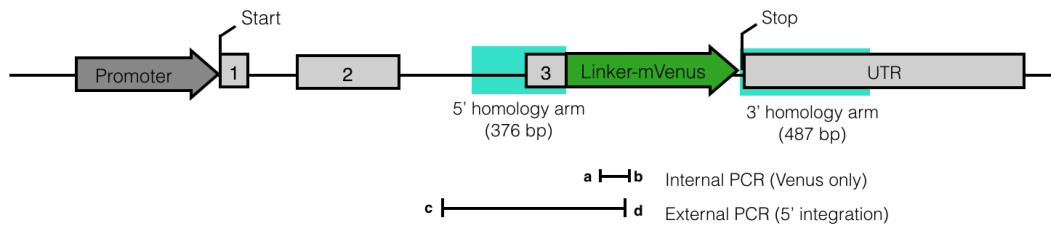


**Figure 24:** Schematic outlining targeting strategy for FGF-signaling reporter Snai1a-Venus. Homology arms (376 and 487 bp) outlined in blue.

CRISPR/Cas9 was used to endogenously tag the *snai1a* locus with a linker-Venus at the 3' end of the coding sequence, as shown in **figure 24**. Two sgRNAs were tested, T2 and T3, leading to two different founders with in-frame integrations at the endogenous *snai1a* locus, as summarized in **table 7**. Expression of Snai1a-Venus was also bright enough to be visible in a stereomicroscope, and seems to accumulate all along the axis, in both somites and PSM of developing medaka embryos (**figure 25**). In addition, large, bright nuclei are visible in the yolk around the main body axis. Due to their large size, these could correspond to the nuclei of the yolk syncytial layer in zebrafish (YSL, [147, 148]). In support of this, *snai1a* expression has previously been observed in the YSL in zebrafish [149].

**Table 7:** Targeting efficiency in the Snai1a-Venus CRISPR knock-in lines

sgRNA injected		Injected	Raised	Venus +	5'integration +	Germline transmission to F1 (in-frame integration)
T2	Total nr. F0	12	5	2	1*	11/30 (37%)
	% of raised F0	-	100%	40%	20%	-
T3	Total nr. F0	14	4	1	1	16/40 (40%)
	% of raised F0	-	100%	25%	25%	-

\*Also 3'integration +

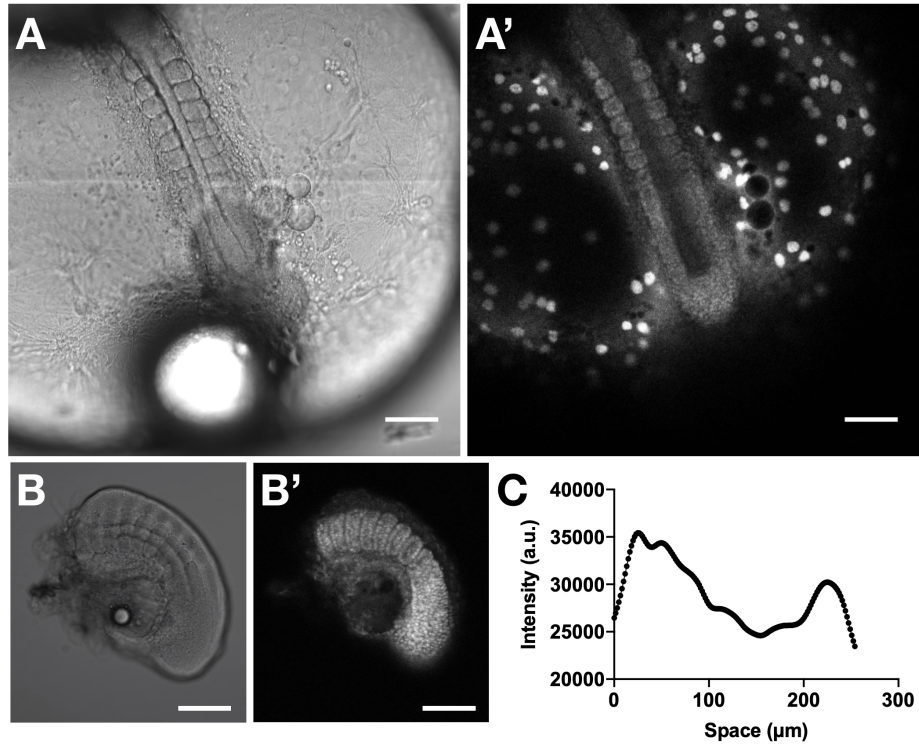


**Figure 25:** The Snai1a-Venus knock-in line. **(A)** Expression in somites and PSM of a whole embryo, from a single z-plane. Expression is also apparent in the nuclei of the yolk, possibly in the yolk syncytial layer (YSL). **(B)** Expression in tail explant from a single z-plane. **(C)** Intensity profile of a 20-pixel wide line drawn along the PSM of maximum projected image of the embryo in **(A)** shows the Snai1a-Venus gradient in space, from posterior to anterior (posterior set to 0). Dorsal **(A)** and lateral **(B)** view, posterior oriented towards the bottom. Scale bars 100  $\mu\text{m}$ .

## 4. Results – Part II: Exploring mechanisms of temperature compensation

How do embryos maintain proper patterning in the face of fluctuating environmental conditions? The relationship between the rate of somite formation and temperature has been characterised for zebrafish between 20-30°C [26], showing that somite size is temperature-invariant. However, without real-time measurements of the segmentation clock, we lack the knowledge to understand how the underlying signalling dynamics scale with changes in temperature. Medaka embryos have been reported to tolerate an impressive range of temperatures between 4-40°C [32, 33], making them well suited to study developmental robustness. Generally medaka are kept at at 27-28°C. For this reason, Her7-Venus dynamics (using both Her7-Venus1 and Her7-Venus2) were first quantified at 27°C (**section 4.1**). In order to address the mechanism behind temperature-invariant patterning, the Her7-Venus2 line was then used to explore how oscillation dynamics respond to temperature variation between 23-37°C (**section 4.2**).

### 4.1 Quantification of medaka segmentation clock dynamics at 27°C

#### 4.1.1 Time-lapse imaging of Her7-Venus oscillations in medaka

To characterise dynamic expression, live confocal imaging was carried out in the medaka Her7-Venus lines. To improve throughput and simplify imaging, a previously established culture method used for mouse tail explants [72, 135] was adapted for culture of embryonic medaka tissue. This culture protocol can be used to culture whole tail explants in glass bottom dishes, or for 2D-segmentation *in vitro* assays using the most posterior tip of the PSM (the tailbud) on fibronectin-coated dishes [72]. In general, tail explants provide the most reproducible data. While somite boundaries are not clearly visible in the medaka 2D-assay, tail explants grow and form somites in culture.

Live confocal imaging revealed that regular Her7-Venus oscillations were distinctly visible in whole embryos (**figure 26a-c**), segmenting tail explants (**figure 26g-i**) and in 2D-assays (**figure 26m-o**). In both whole embryos and tail explants Her7-Venus waves originate in the tailbud, and appear to sweep from posterior to anterior. Each cycle is defined by the appearance of one coherent wave, which coincides with the formation of one somite pair.

When oscillations reach the anterior PSM, they terminate with a single stripe of expression where the next somite boundary forms.

The oscillation dynamics in the PSM can be visualized as a kymograph, (**figure 26j, d and p**), which also enables the extraction of time-series data, as shown in **figure 26 e, k and q**. For example, the kymograph and time-series data generated from a tail explant shown in **figure 26j and k**, shows the initiation of ten waves of expression in 800 minutes (which correspond to the formation of ten segment boundaries in the brightfield channel), indicating a period of ~80 minutes. The kymograph also shows how the oscillatory field regresses as somites form at the anterior, while growth from the posterior end shifts the whole field downwards.

Imaging in intact embryos is complicated by the presence of periodic yolk contractions that cause movement of the sample. These contractions can be partially blocked by adding the gap-junction inhibitor heptanol [39], although throughput remains low due to the fragility of dechorionated embryos. Therefore, all subsequent quantification was carried out in tail explants, unless otherwise specified.

Thus, the Her7-Venus knock-in line allows time-lapse imaging of segmentation clock oscillations during medaka development for the first time.

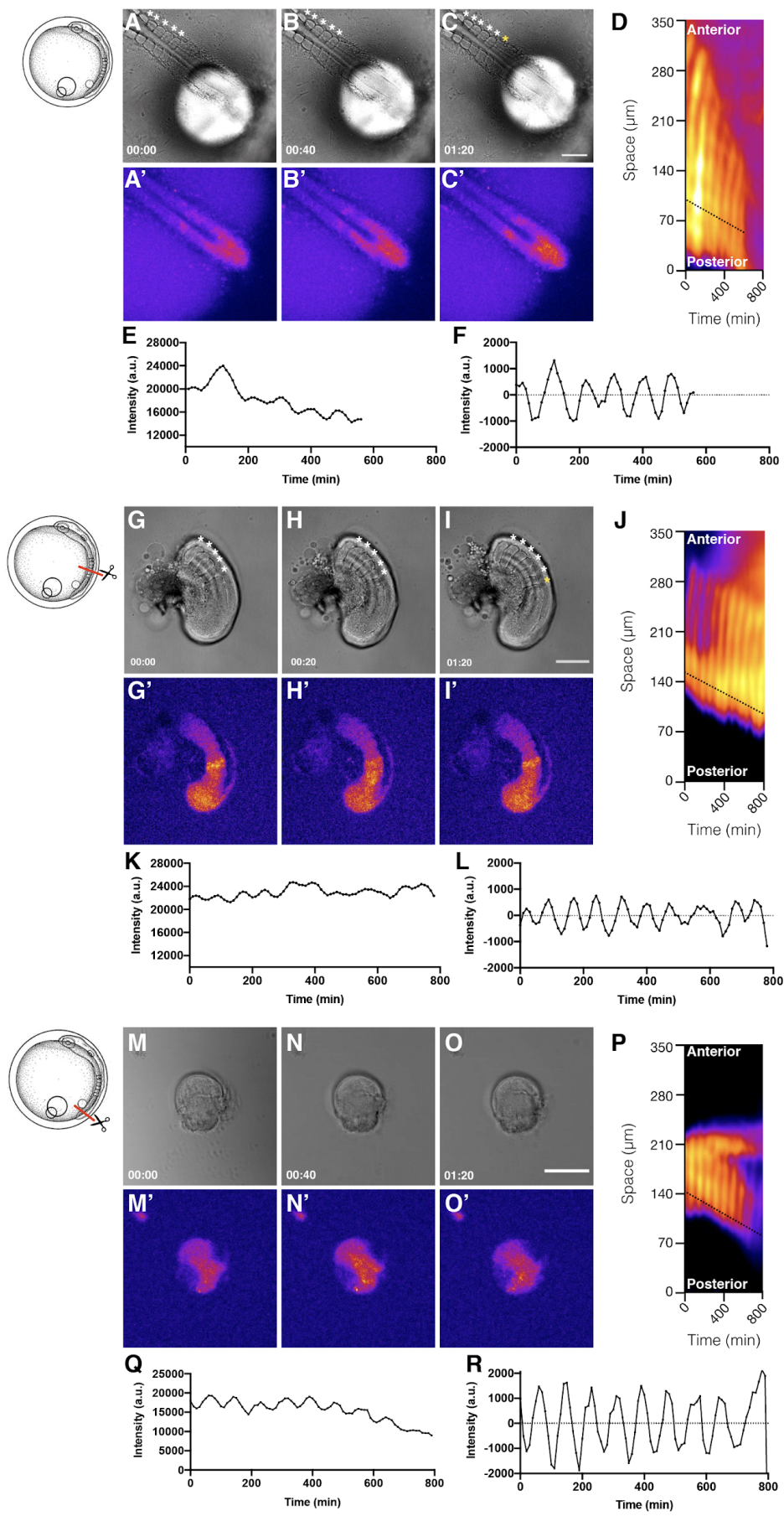


Figure 26

**Figure 26:** Real-time imaging of Her7-Venus oscillations in the confocal microscope at 27°C. **(A-C)** Imaging of a whole medaka embryo in 0.5% low-melting point agarose with 3.5mM heptanol. Dorsal view, posterior oriented towards the bottom right. **(G-I)** Imaging of a tail explant in culture medium. Lateral view, posterior oriented towards the bottom. **(M-O)** Imaging of tailbud tissue in a 2-D assay cultured on a fibronectin-coated plate in culture medium. Bottom view. Somites labeled with white asterisks, newly formed somite labeled with yellow asterisk. To visualize oscillations, a line can be drawn from the posterior to the anterior PSM in whole embryos or tail explants and intensity along this line can be plotted as a kymograph, where 0 corresponds to the posterior PSM as shown in **(D)** for the whole embryo and **(J)** for the tail explant. For the tailbud 2D assay, a line is drawn in the direction of wave propagation as shown in **(P)**. By drawing a line at the base of each kymograph (black dotted lines in **D**, **J** and **P**), raw time-series data **(E,K,Q)** can be extracted and detrended as shown in **(F,L,R)** for whole embryo, tail explant and tailbud 2D-assay respectively. Time in hours:minutes, scale bar 100  $\mu\text{m}$ . Schematic adapted from (Iwamastu [49]).

## 4.1.2 Quantification of segmentation clock dynamics

By closely examining the kymographs in **figure 26d** and **figure 26j**, it becomes apparent that the slope of the wave becomes slightly less steep as each wave reaches the anterior, indicating that it slows down as it travels along the PSM. Thus, it follows that there are multiple periods in the system. However, the period at the posterior PSM corresponds to the periodicity of a full wave, which can be used as a proxy for the rate of somite formation.

To measure segmentation clock period in tail explants, the period of oscillations was therefore determined in the tailbud (**figure 27a**). The extracted time-series data was used as an input for a wavelet analysis tool developed by Gregor Mönke in the lab (Mönke et al, in preparation). Following detrending of the signal (**figure 27b**, **figure 27c**), a cross-correlation is performed at each timepoint to a series of wavelets with defined period, which generates a spectrum as shown in **figure 27d**. When the wavelet of a given period has a high cross-correlation with the signal, it is given a high “power” score, defined as how much more likely this signal is to achieve a high correlation relative to white noise. The period is then extracted from this spectrum, as shown in **figure 27e**. Wavelet analysis revealed an average oscillation period over time of  $80.7 \pm 1.66$  and  $82.4 \pm 4.48$  minutes at 27°C, in tail explants derived from both Her7-Venus2 heterozygotes and homozygotes respectively ( $n = 5$  for each group, **figure 27e**).

To validate the explant culture method, oscillation period was also compared between intact embryos (without culture medium, in 0.5% low melting point agarose with 3.5mM heptanol), tail explants and tailbud 2-D assays (**figure 28**). While Her7-Venus in the PSM of whole embryos had an average oscillation period of  $86.6 \pm 3.4$  minutes ( $n=6$ ), Her7-

Venus in both tail explant and tailbud 2D-assays oscillates slightly faster, at  $79.5 \pm 2.8$  minutes ( $n=9$ ) and  $81.0 \pm 1.9$  minutes ( $n=6$ ) respectively. While this may be due to the tissue culture conditions, these samples are also representative of different developmental time points, since tail explants and tailbud 2D-assays are cultured from the 12 somite stage, whereas whole embryos are cultured from the 3-4 somite stage.

Together, these results demonstrate that segmentation clock oscillations, which correspond to period in the posterior PSM, have a periodicity between 79.5-86.6 minutes in medaka PSM at  $27^\circ\text{C}$ . Furthermore, the oscillation period is comparable between whole embryos, tail explants and 2D assays.

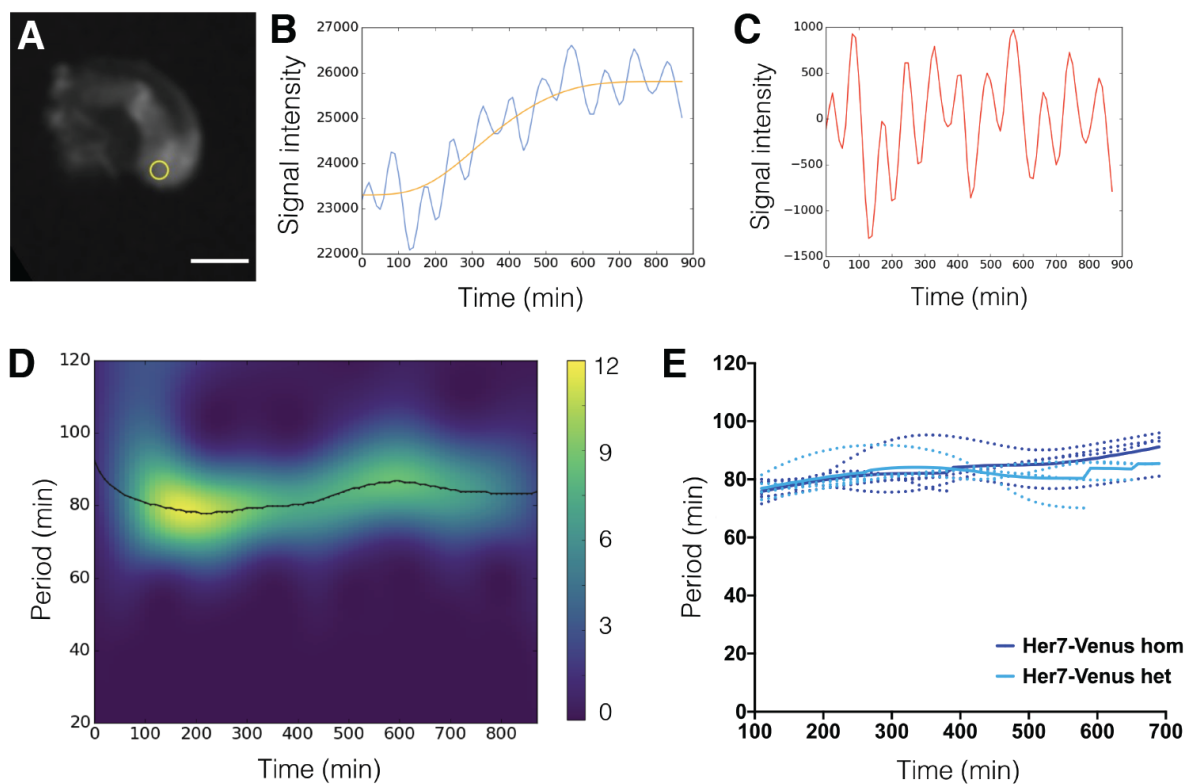


**Figure 27:** Quantification of oscillation period in medaka tail explants at  $27^\circ\text{C}$ . A time-lapse dataset of maximum-projected fluorescence images is used to quantify signal intensity over time using a moving ROI following the posterior tailbud as shown in (A), resulting in a raw time-series as shown in (B). The yellow line shows the trend in the data. (C) Detrended signal used as the input for a time-frequency (wavelet) analysis (Gregor Mönke) shown in (D) which reveals a period of around 80 min over time. The color map represents the power value according to the scale bar on the right. (E) Plotting extracted period over time,  $80.7 \pm 1.66$  and  $82.4 \pm 4.48$  minutes for Her7-Venus2 heterozygotes and homozygotes respectively. Dotted lines show individual samples, solid lines show mean for each group.  $N = 2$ ,  $n = 5$ , 5 for heterozygotes and homozygotes respectively. Scale bar  $100 \mu\text{m}$ .

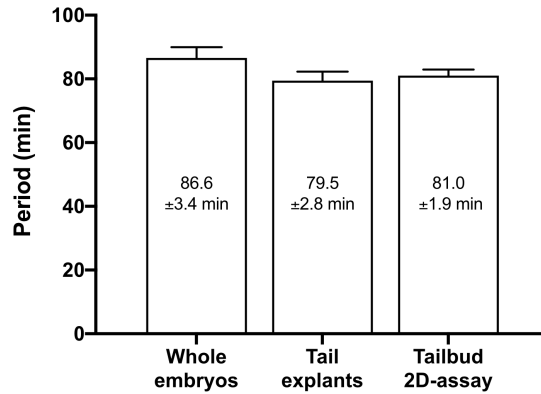


**Figure 28:** Comparison of oscillation period in the Her7-Venus1 line between whole embryos, tail explants and tailbud 2D-assays at 27°C. Mean period and standard deviation indicated in each column. N = 1, n = 6 for whole embryos, N = 2, n = 9 for tail explants, and N = 2, n = 6 for tailbud 2D-assays.

### 4.1.3 Comparative analysis of oscillation dynamics in the Her7-Venus1 and Her7-Venus2 lines

As discussed in **section 3.1.4**, the original Her7-Venus1 line showed a strong downregulation of *her7* RNA in the PSM (see **figure 15**) linked to the accidental integration of the donor vector backbone in the 3'UTR of the endogenous locus. Removal of the integrated backbone increased the signal intensity of Her7-Venus oscillations.

In order to see if the removal of the donor backbone integration had any effect on Her7-Venus dynamics, the period of oscillations from the original Her7-Venus1 (hypomorph) line and the new Her7-Venus2 line were compared in tail explants. Interestingly, period is not significantly affected by the presence of the donor backbone integration in the Her7-Venus1 line, with homozygous explants oscillating at  $81.1 \pm 2.1$  minutes (n = 5) and  $82.4 \pm 4.5$  minutes (n = 5) before and after backbone removal, respectively. In addition, heterozygous embryos which still carry one unmodified copy of the *her7* locus oscillate with a similar period, at  $78.2 \pm 1.1$  minutes (n = 4) and  $80.7 \pm 1.7$  minutes (n = 5) before and after backbone removal, respectively (**figure 29**).

Therefore, despite the strong reduction in *her7* RNA in the Her7-Venus1 line, oscillation period remains comparable between the Her7-Venus1 and Her7-Venus2 lines.

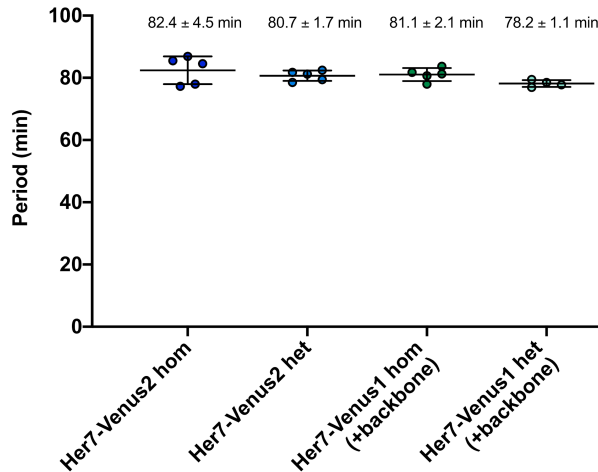


**Figure 29:** Comparison of oscillation period in the Her7-Venus line before and after the removal of the integrated donor backbone. Period of oscillations does not change significantly after donor backbone removal.  $N = 2$ ,  $n = 5$ ,  $5$  for Her7-Venus2 homozygotes and heterozygotes, and  $N = 2$ ,  $n = 5$ ,  $4$  Her7-Venus1 homozygotes and heterozygotes (with extended UTR) respectively.

#### 4.1.5 Quantification of the period and phase gradients in the PSM

Previous studies of oscillatory dynamics in the PSM of mouse and zebrafish have demonstrated that there is a period gradient along the PSM, with cells at the posterior oscillating faster than cells at the anterior [74, 77]. In order to fully describe the behaviour of Her7-Venus oscillations, the spatial aspect therefore has to be taken into account. To address this, the wavelet analysis tool described previously (in **section 4.1.2**) can be applied to generate wavelet movies by quantifying oscillation dynamics in each pixel of a time-series dataset, as shown in **figure 30**. These movies can be used to not only measure the period, but also the corresponding phase in space along the oscillating PSM (**figure 31**). To define the anterior limit of the oscillatory field, the PSM and somite boundaries were annotated using the brightfield channel at a time-point where a somite boundary has just formed (as shown in **figure 30a**). Measuring in the posterior-anterior direction within this area revealed that Her7-Venus oscillates at around ~80 minutes in the posterior, slowing to ~100 minutes in the anterior PSM.

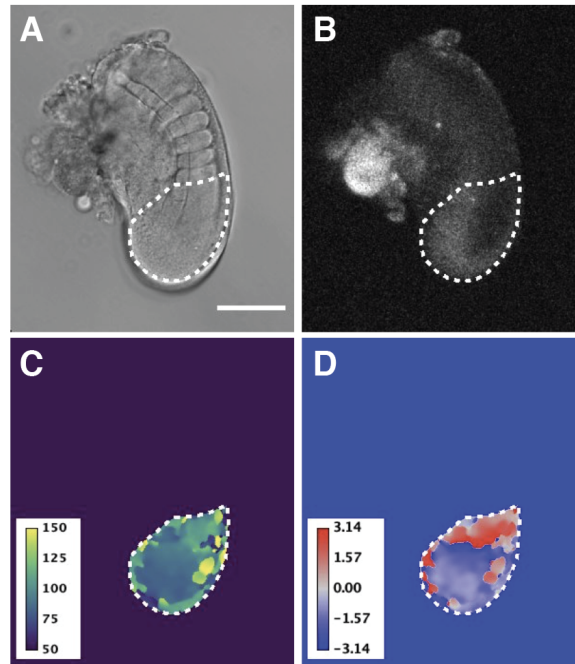


**Figure 30:** Still frames of imaging dataset and corresponding wavelet movies at a time-point when a somite pair has just formed. **(A)** Brightfield and **(B)** Venus fluorescence image of a tail explant in culture, showing the PSM outlined by a white dashed line. **(C)** Period movie, with the period gradient spanning between 80-100 minutes. **(D)** Phase movie, with the phase gradient spanning between 3.14 and -3.14. Lateral view, posterior oriented towards the bottom. Scale bar 100  $\mu\text{m}$ .

The slowing of *her7* oscillations according to the period gradient leads to a slight phase-shift in each cell relative to its neighbour, resulting in a phase gradient along the PSM. Using the wavelet movies, we can quantify the spatial phase-shift in time and space. As shown in **figure 30d**, the phase span measured in the PSM roughly ranges from  $-\pi$  to  $\pi$  radians. To quantify the phase gradient, phase was calculated and made continuous from  $0$ - $2\pi$  (phase unwrapping), where  $0$  is set to the posterior. As shown in **figure 31b**, this revealed a clear phase gradient from posterior to anterior, with an amplitude of  $4.69 \pm 1.79$  radians ( $n = 9$ , **figure 31c**). Values were normalized to PSM length to account for variation in both PSM size, and in the curvature of the line used to measure both the phase and period gradients (**figure 31a' and b'**). Another way of representing the phase amplitude data is by plotting the wave number [75], or the number of full  $\pi$  to  $-\pi$  waves present in the PSM for each measurement, which was calculated to be  $0.75 \pm 0.29$  waves ( $n = 9$ , **figure 31c'**).

These results confirm the presence of a period gradient where oscillations are about 20 minutes slower in the anterior PSM relative to the posterior PSM. In addition, measurements of a phase gradient spanning just under  $2\pi$  agrees with the observation that approximately 0.75 coherent waves are travelling in the PSM at any given time.

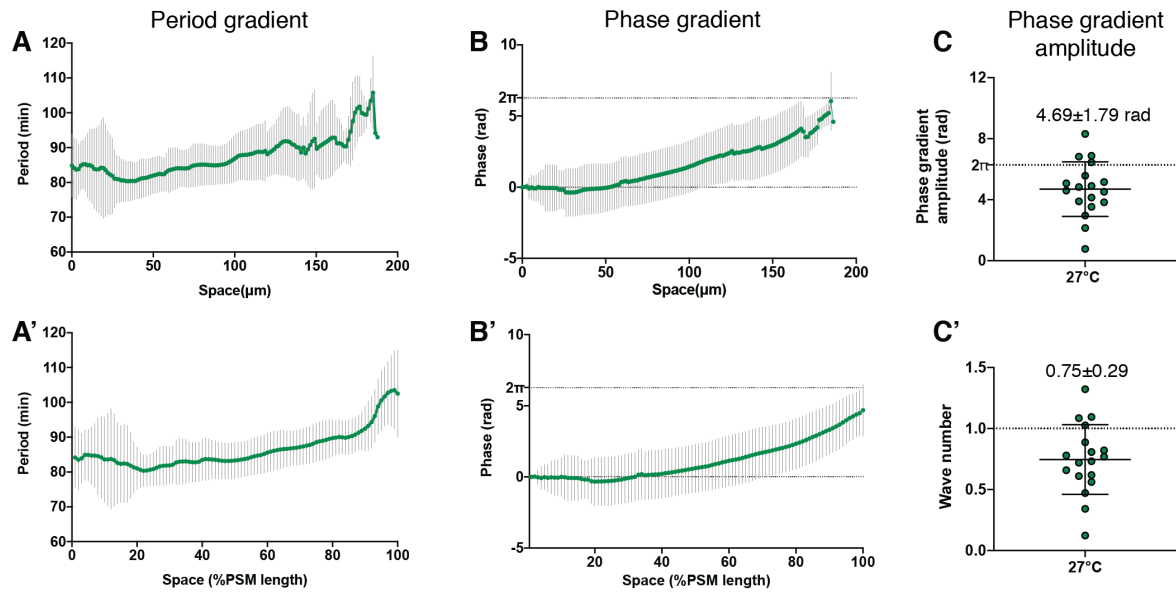


**Figure 31:** Period and phase gradients at 27°C. **(A)** Period, **(B)** phase gradients and **(C)** phase gradient amplitude in tail explants cultured at 27°C, measured using wavelet movies. Normalized to PSM length in **(A')** and **(B')**, normalized to wave number [75] in **(C')**. Posterior end of the PSM is set to 0 in **(A)** and **(B)**. Mean and standard deviation over space. N = 2, n = 9 embryos, with two measurements per embryo.

## 4.2 Quantification of medaka segmentation clock dynamics between 23-37°C

### 4.2.1 Defining the range of temperature-compensated patterning in medaka

Generally medaka are kept between 27-28°C, but to establish the viable range of temperatures where compensation happens, groups of embryos were put at temperatures ranging from 4-40°C immediately after fertilisation until 7-8 somite stage or hatching. As shown in **figure 32**, the permissible range of temperatures for embryos to make it all the way until hatching is between 17-35°C. Within this temperature range, time to hatching was variable, and embryos developed faster at warmer temperatures than colder ones. Below this range, at 15°C 47% of embryos did reach 7-8 somite stage, but the rate of embryonic development was highly variable, and several embryos had visible defects already from gastrulation stages. At 10°C embryos develop very slowly, and gastrulation appears severely impaired. On the other hand, at 37°C, fertilised embryos did not proceed with development.

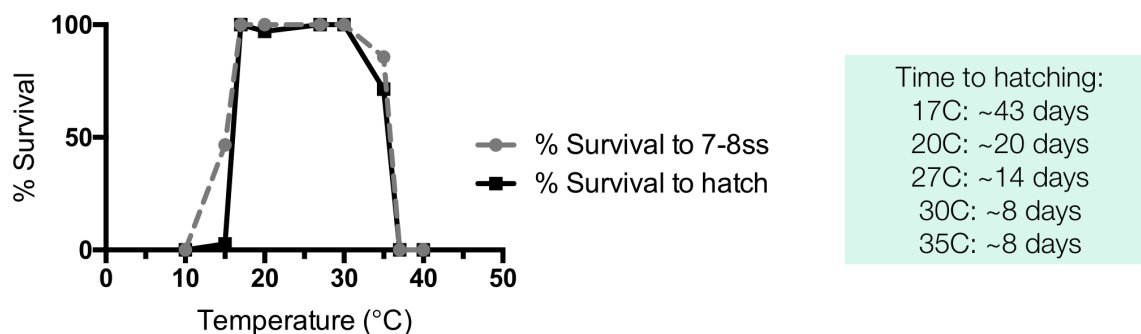


**Figure 32:** Survival of embryos grown at different temperatures

To determine how patterning is affected during development at different temperatures, wildtype embryos were grown between 15-35°C until Iwamatsu stage 22. Staging was determined based on the morphology of the head and number of visible somites. As a read-out, somite morphology and polarity was quantified in fixed embryos by three-color *in situ* hybridization chain reaction (HCR; [150]) (**figure 33**) using probes listed in **Table 8**. HCR is a sensitive, high-resolution technique which makes it easier to quantify morphological features compared to colorimetric *in situ* hybridization.

**Table 8:** List of probes used for *in situ* hybridization chain reaction in order to compare morphology and polarity of embryos grown between 15-35°C.

Gene	Expression pattern
<i>myf5</i>	Expressed in posterior domain of mature somites, and anterior PSM
<i>mesp-a</i>	Dynamically expressed in one or two progressively narrowing stripes, marking the next forming somite, or where PSM ends
<i>mesogenin</i>	Expressed in PSM

At 27°C and 35°C, *myf5* is clearly localized to the posterior somites, *mesp* is expressed dynamically in one or two stripes where it specifies the next forming somite, and *mesogenin* is visible below the *mesp* domain in the unsegmented PSM. However, when embryos were grown at 15°C, 7/13 embryos showed severely disorganized *myf5* staining, with most somites lacking a clear posterior compartment. In the remaining 6/13 embryos, the majority of somites have a defined *myf5*-positive posterior compartment. Despite this, all samples grown at 15°C still exhibit dynamic *mesp* staining (although the anterior stripe appears broader) and *mesogenin* staining is visible in the unsegmented PSM (**figure 33a**).

Although somite polarity is disrupted at 15°C, somite boundaries are still visible in the embryos with relatively organized *myf5* staining. Calculating the average somite length revealed that somite length in embryos grown at 15°C is comparable to those grown at 27°C, at  $38.1 \pm 2.0 \mu\text{m}$  (n=6) and  $40.2 \pm 1.2 \mu\text{m}$  (n=8) respectively, despite the fact that they are improperly patterned. Further, the somites in embryos grown at 35°C are smaller than in the two other groups, with an average somite size of  $34.8 \pm 0.7 \mu\text{m}$  (n=9, **figure 33b**).

In summary, development of medaka embryos occurs normally between 17-35°C. However, while segments grown at 35°C have normal anterior-posterior polarity, they are slightly smaller than 27°C controls. In contrast, somites in embryos grown at 15°C do not display normal anterior-posterior polarity, yet segment size is comparable to 27°C controls.

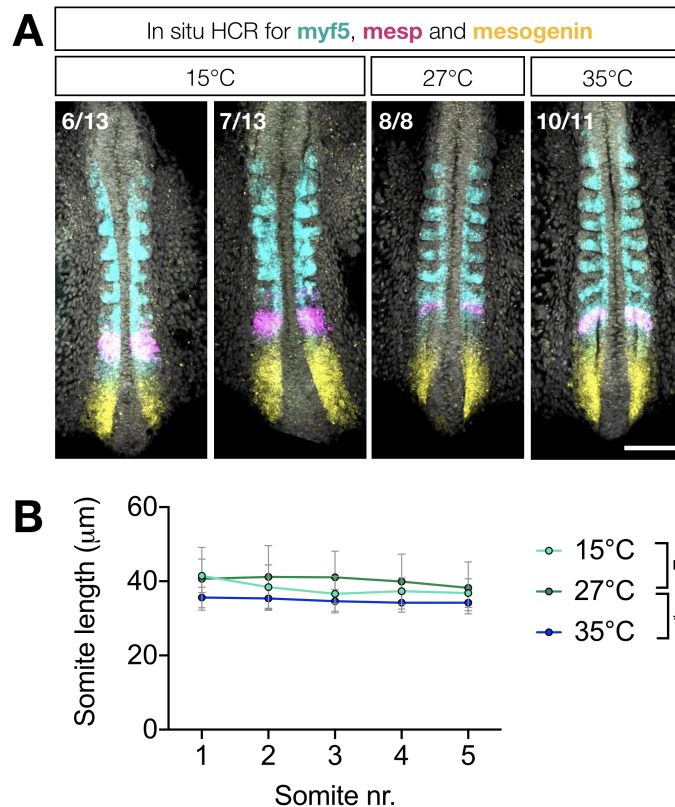


**Figure 33: (A)** HCR staining of *myf5* (posterior somite marker, in cyan), *mesp* (marker of next forming somite, in magenta) and *mesogenin* (PSM marker, in yellow) in embryos grown at 15°C, 27°C and 35°C until Iwamatsu stage 22. **(B)** Quantification of somite size from HCR images. Mean somite length and standard deviation is  $38.1 \pm 2.0 \mu\text{m}$ ,  $40.2 \pm 1.2 \mu\text{m}$  and  $34.8 \pm 0.7 \mu\text{m}$  from  $n=6$ ,  $8$  and  $9$  embryos for 15°C, 27°C and 35°C, respectively. Dorsal view, posterior oriented towards the bottom. Scale bar 100  $\mu\text{m}$ .

#### 4.2.2 Exploring Her7-Venus oscillation dynamics between 23-37°C

To explore how signaling dynamics change in response to temperature, live imaging of tail explants from the Her7-Venus2 line was performed between 23-37°C, with a temporal resolution of 5 or 10 minutes. While tail explants segmented and grew normally at 23°C and 27°C, imaging in culture at 35°C and 37°C resulted in abnormal growth and morphology. Despite this, quantifiable oscillations still persisted in the tissue, and are therefore included in subsequent analysis.

### 4.2.3 Quantification of posterior oscillation period between 23-37°C

To quantify how period in the posterior PSM changes with temperature, intensity profiles were generated from live-imaged Her7-Venus2 heterozygous tails in the posterior PSM. Period in the posterior PSM was then extracted using wavelet analysis of the intensity profiles. To determine the parameters for this wavelet analysis, all samples were first processed using the same settings with a wide range of periods to scan for, between 20-200 minutes. Following this first scan, the samples were scanned again with more stringent settings to extract less noisy data.

Changing the culture temperature of Her7-Venus tail explants affected oscillatory behaviour, with explants at 35°C and 37°C oscillating faster and explants at 23°C oscillating slower than the controls at 27°C. This trend is reflected in kymographs where, for the same interval of time, an increasing number of waves are visible in the PSM with increasing temperature (**figure 34a**). To quantify this change, period in the posterior PSM was measured for each condition (**figure 34b**). These measurements revealed an average oscillation period of  $125 \pm 4.7$  minutes at 23°C,  $81.4 \pm 4.3$  minutes at 27°C,  $57.5 \pm 4.9$  minutes at 35°C and  $57.4 \pm 2.5$  min at 37°C ( $n = 6, 9, 21, 7$  respectively, with two measurements per embryo). Plotting this data by frequency as a function of temperature reveals a linear relationship between the two (**figure 34b**).

These results demonstrate that the period of the Her7 segmentation clock changes between 23-37°C, and is therefore not temperature-compensated. Importantly, while period changes 2.2 fold, average somite size only changes about 1.15 fold (between 34.8-40.2  $\mu\text{m}$ , see **figure 33b**) between 15-35°C.

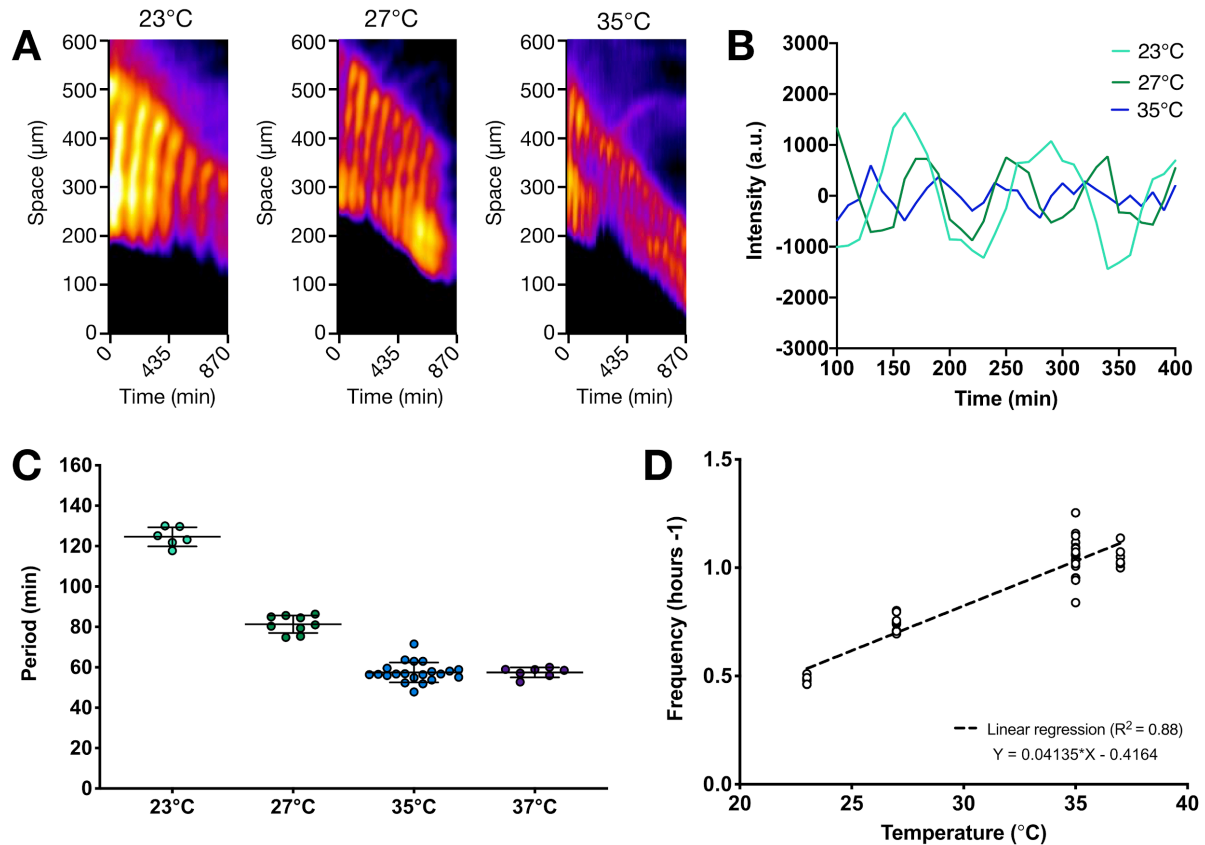


**Figure 34:** Period of Her7-Venus oscillations change over temperature. **(A)** Kymographs showing Her7-Venus oscillations in tail explants between 23-35°C. Note more oscillations occur over the same time period at higher temperatures. **(B)** Detrended Her7-Venus signal extracted using a moving ROI at the posterior end of tail explants between 23-35°C in the samples shown in **(A)**. **(C)** Oscillation period measured in the posterior tailbud between 23-37°C, mean period is  $125 \pm 4.7$ ,  $81.4 \pm 4.3$ ,  $57.5 \pm 4.9$  and  $57.4 \pm 2.5$  min, for 23°C, 27°C, 35°C and 37°C respectively. **(D)** Same data as in **(C)**, plotted as frequency over temperature with line of best fit from linear regression. Mean period and standard deviation from  $N = 1, 2, 4, 1$  and  $n = 6, 9, 21, 7$  embryos for 23°C, 27°C, 35°C and 37°C respectively.

#### 4.2.4 Quantification of period gradient between 23-37°C

Her7 dynamics change along the PSM, forming a period gradient from posterior to anterior (**figure 31a**). To explore how this aspect of the dynamics changes with temperature, wavelet movies were generated. Using the wavelet movies, the period gradient was measured as described in **figure 31**. Interestingly, as observed for the period of Her7-Venus oscillations in the posterior PSM, higher temperatures result in globally faster oscillations, and a significant shift of the entire period gradient in space (**figure 35, table 9**).

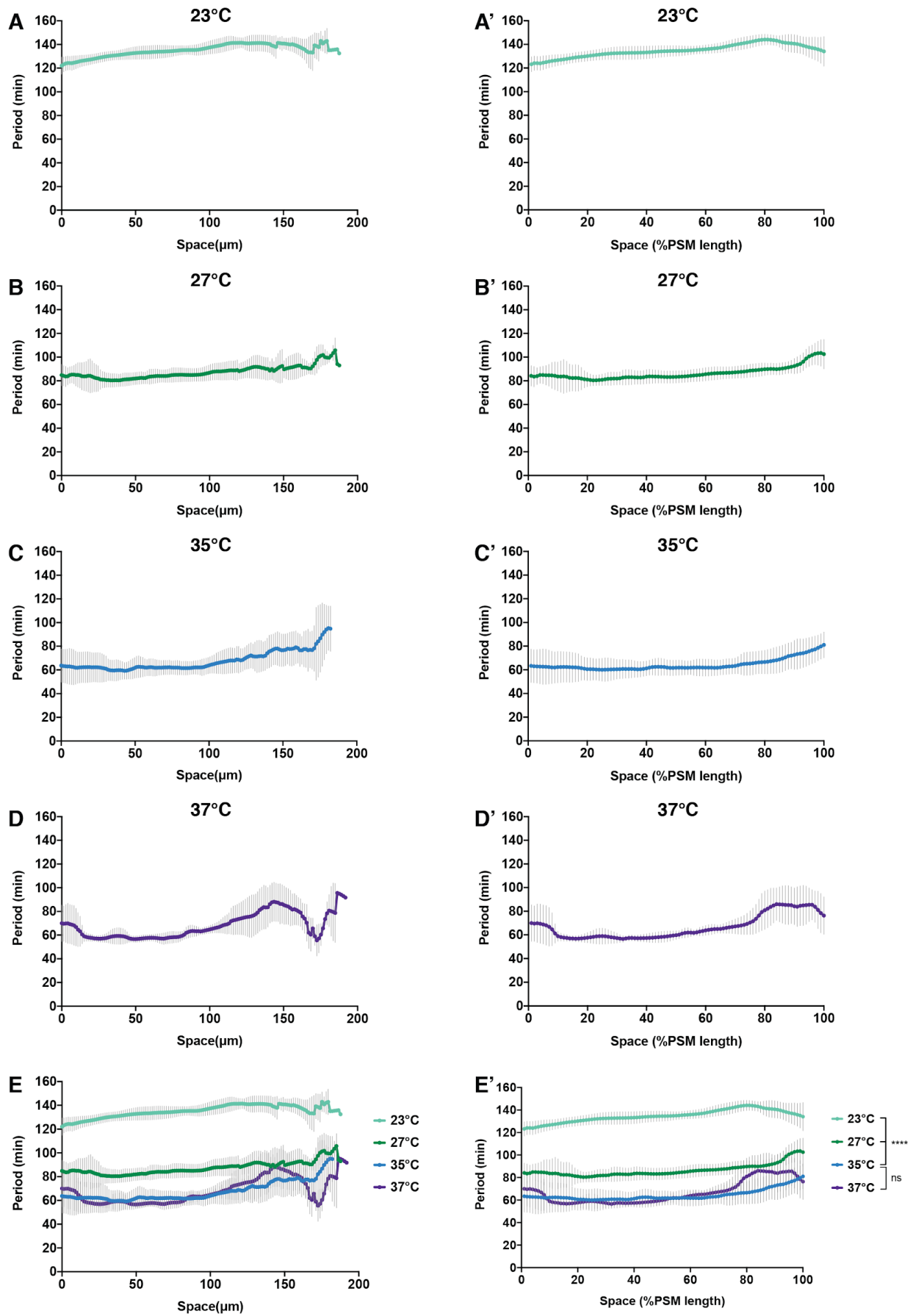
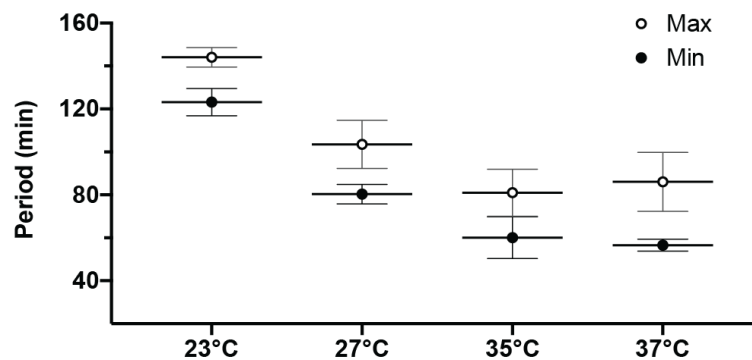


Figure 35

**Figure 35:** Period gradient over space measured between 23-35°C. Posterior end of the PSM is set to 0 in all cases. **(A-D)** Period measurements for each condition with space in  $\mu\text{m}$ , overlaid in **(E)**. **(A'-D')** Period measurements for each condition with space normalised to %PSM length, overlaid in **(E')**. Mean period and standard deviation over space from  $N = 1, 2, 4, 1$  and  $n = 6, 9, 21, 7$  embryos with two measurements, each averaging 20 pixels, per embryo, for 23°C, 27°C, 35°C and 37°C respectively. Significance was calculated using one-way Welch ANOVA where  $ns = P > 0.05$ , and  $**** = P < 0.0001$ .



**Figure 36:** Period gradient amplitude measured between 23-37°C. Minimum and maximum period values were calculated from the average lines shown in **figure 35**, as shown in table 9.  $N = 1, 2, 4, 1$  and  $n = 6, 9, 21, 7$  embryos (with two measurements per embryo), for 23°C, 27°C, 35°C and 37°C respectively. Significance was calculated using one-way Welch ANOVA where  $ns = P > 0.05$ .

To quantify how much slower the anterior oscillations are relative to the posterior oscillations, the period gradient amplitude was calculated. To circumvent individual noisy measurements, period gradient amplitude was calculated by subtracting the mean minimum value (from **figure 35**) for all measurements from the mean maximum value for all measurements, plotted in **figure 36** and summarized in **table 9**. These results show that the period gradient amplitude is between 20.8-23.2 minutes in all groups except for the tails imaged at 37°C, where the amplitude is higher at 29.5 min.

Oscillation period in the posterior and anterior PSM changes between 23-37°C, demonstrating that the period gradient is not temperature-compensated. However, unlike the period values themselves, the period gradient amplitude remains relatively constant at all temperatures except 37°C.

**Table 9:** Calculation of period gradient amplitude using mean maximum and minimum values from **figure 35**.

Group	Mean min period (min $\pm$ SD)	Mean max period (min $\pm$ SD)	Amplitude (min)	Amplitude (% of max)
23°C	123.2 $\pm$ 6.3	144.0 $\pm$ 4.6	20.8	14.5
27°C	80.3 $\pm$ 5.8	103.5 $\pm$ 4.4	23.2	22.4
35°C	60.0 $\pm$ 9.7	81.0 $\pm$ 10.9	21.0	25.7
37°C	56.6 $\pm$ 5.9	86.0 $\pm$ 4.3	29.5	34.2

#### 4.2.5 Quantification of phase gradient between 23-37°C

Knowing that the period gradient changes with temperature, I next investigated how the phase gradient would respond. Therefore, the phase gradient was measured between 23-37°C (**figure 37**). Using the same time points used to measure the period gradient, the phase gradient from posterior to anterior was calculated in the wavelet movies as described for **figure 31**. The phase gradient does indeed span close to  $2\pi$  radians, and is not significantly different between conditions (**figure 37e**). The phase span was also calculated in measurements of the mean phase gradient amplitude, calculated to be  $5.26 \pm 1.24$  rad,  $4.69 \pm 1.79$  rad,  $5.21 \pm 2.26$  rad and  $5.20 \pm 1.64$  rad for 23°C, 27°C, 35°C and 37°C respectively ( $n = 6, 10, 21, 7$  embryos, with two measurements per embryo) (**figure 38a**). This corresponds to wave numbers of  $0.84 \pm 0.20$ ,  $0.75 \pm 0.29$ ,  $0.77 \pm 0.46$  and  $0.67 \pm 0.48$  for 23°C, 27°C, 35°C and 37°C respectively (**figure 38b**). In other words, just under one full wave at a time is travelling across the tissue in all conditions tested. These results reveal that unlike the period gradient, the phase gradient does not significantly vary between conditions.

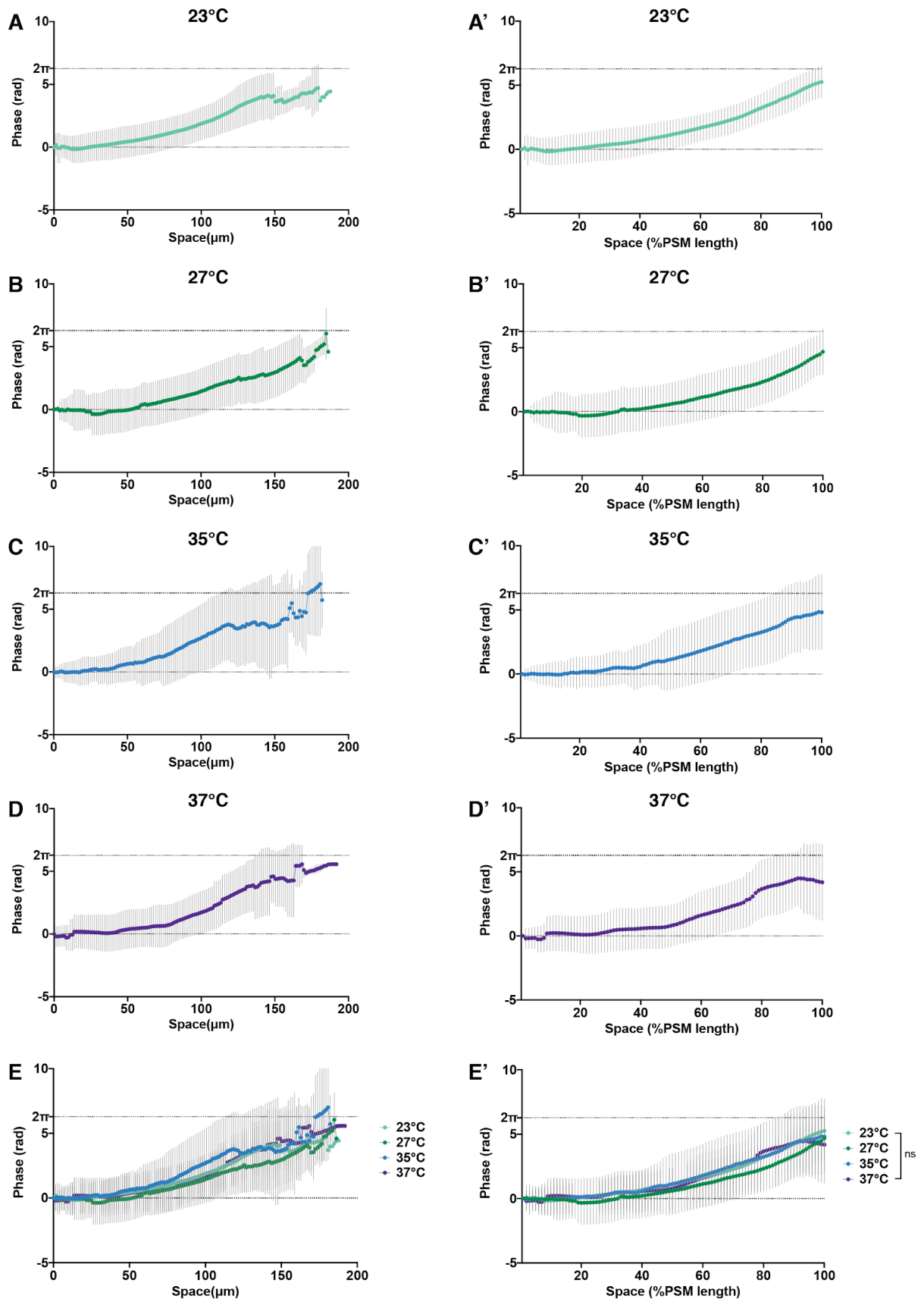


**Figure 37**

**Figure 37:** Phase gradient over space measured between 23-37°C. Posterior end of the PSM is set to 0 in all cases. **(A-D)** Phase measurements for each condition with space in  $\mu\text{m}$ , overlaid in **(E)**. **(A'-D')** Phase measurements for each condition with space normalised to %PSM length, overlaid in **(E')**. Mean phase and standard deviation over space from  $N = 1, 2, 4, 1$  and  $n = 6, 9, 21, 7$  embryos (with two measurements per embryo) for 23°C, 27°C, 35°C and 37°C respectively. Significance was calculated using one-way Welch ANOVA where  $ns = P > 0.05$ .

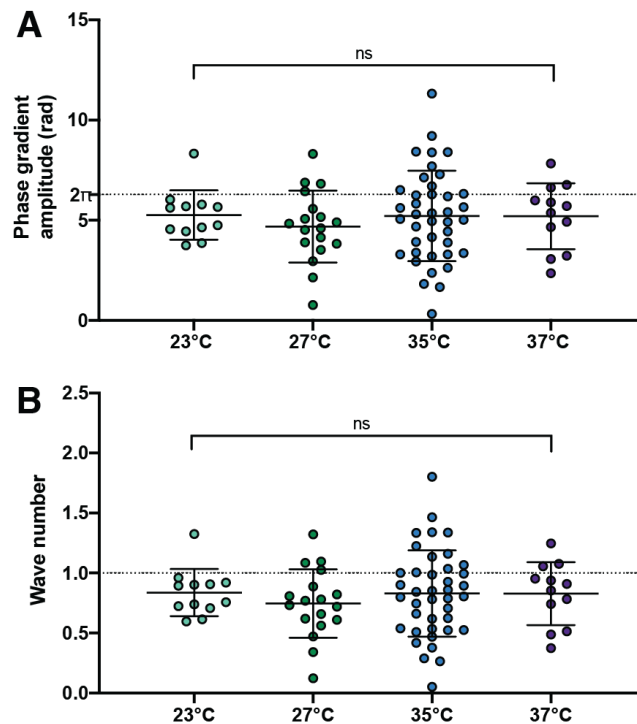


**Figure 38:** Phase gradient amplitude and wave number measured between 23-37°C. **(A)** Mean phase gradient amplitude calculated by subtracting the first value from the last values for each measurement. Mean and standard deviation is  $5.26 \pm 1.24$  rad,  $4.69 \pm 1.79$  rad,  $5.21 \pm 2.26$  rad and  $5.20 \pm 1.64$  rad for 23°C, 27°C, 35°C and 37°C respectively. **(B)** Wave number [75] calculated using the same values as in **(A)**, corresponding to  $0.84 \pm 0.20$ ,  $0.75 \pm 0.29$ ,  $0.77 \pm 0.46$  and  $0.67 \pm 0.48$  waves for 23°C, 27°C, 35°C and 37°C respectively. Mean and standard deviation from  $N = 1, 2, 4, 1$  and  $n = 6, 9, 21, 7$  embryos (with two measurements per embryo). Significance was calculated using one-way Welch ANOVA where  $ns = P > 0.05$ .

## 5. Discussion

### 5.1 Exploring mechanisms of robustness during patterning and morphogenesis in medaka

During embryonic development, cells are required to interpret a web of dynamic signals and form complex patterns in space and time. This ability to coordinate in order to form stereotypical patterns has to be precisely maintained, even in the face of intrinsic noise and environmental fluctuations. While significant effort is put into maintaining constant conditions during the development of mammalian embryos, externally fertilised species are directly exposed to environmental change. In particular, temperature is known to have an impact on the rate of development in many externally fertilised species, including *Drosophila* [20], *Xenopus* [18], zebrafish [19] and medaka [22]. Developing embryos therefore have to establish mechanisms to buffer against temperature fluctuations to achieve phenotypic robustness.

#### 5.1.1 Medaka can develop normally across a wide temperature range

Adult medaka have been reported to tolerate 4-40°C, and breeding facilities routinely keep large tanks outdoors year-round. Remarkably, adults can survive even under layers of snow and ice, as long as the water does not freeze completely [31]. When the water temperature drops below 5°C they enter a state of hibernation, where they do not feed or spawn [31]. Data collected from one of these outdoor breeding facilities in 2018 showed that medaka can survive between 0.3°C to 35.9°C in these conditions (**figure 39**). Although adult medaka can tolerate this impressive range of temperatures, embryonic development is not likely to occur at the lower end of this range in the wild, as spawning season is only between mid-April and late September in Japan (shaded region in **figure 39a**, [49]).

In this study, embryonic development resulting in viable hatchlings was found to occur between 17-35°C (demarcated between the horizontal black dotted lines in **figure 39a**), which is consistent with previous reports [33]. Outside of this permissive range development was more variable, and a higher rate of lethality was observed. Interestingly, 17-35°C corresponds well to the range of ambient temperatures medaka can be expected to experience during their spawning period in outdoor facilities, as plotted in **figure 39a**.

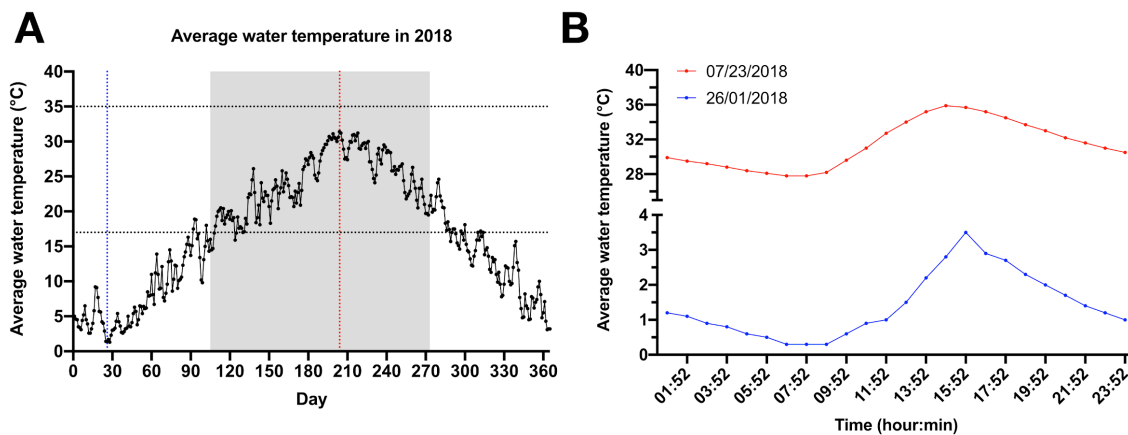


**Figure 39:** Temperature recorded in an outdoor breeding facility in Okazaki (A) Average water temperature for 2018. Coldest and warmest average day marked by blue and red dotted lines, respectively. Spawning season (between mid-April and the end of September) shaded in grey. Black dotted lines demarcate 17–35°C. (B) Temperature fluctuation during day-night cycle on the coldest day (26th of January, in blue, between 0.3°C and 3.5°C) and the warmest day in (23rd of July, in red, between 27.8°C–35.9°C) in 2018. Raw data kindly provided by Dr. Ai Shinomiya, (NIBB, Okazaki) and Professor Takashi Yoshimura (Nagoya University).

While enduring a wide range of constant temperatures is already a significant feat, embryos in the wild face the additional challenge of adapting to a constantly changing temperature. From the data shown in **figure 39b**, we know that during the medaka breeding period in summer, they can experience a span of up to 8°C (between 27.8°C–35.9°C) during one diurnal cycle. Given the linear dependence of segmentation clock period with temperature presented in this study, an embryo developing in these conditions might therefore experience a gradual change in oscillation period between ~56 and ~82 minutes in a single day. Given this big change in oscillation period the outstanding question remains—how do medaka embryos meet the challenge of forming a normal number of well patterned somites under such a wide range of varying temperature conditions?

The Her7-Venus line allows us to directly measure the effect of temperature on segmentation clock oscillations in medaka for the first time. While the live imaging experiments presented here were performed at constant temperatures between 23°C–37°C, future experiments will also address the impact of temperature variation on patterning. This can be tested in the form of continuous variation, similar to what embryos face in their natural habitat, but also more unnatural variation such as would be imposed by a sharp temperature step.

## 5.1.2 Defining the criteria for temperature-compensated segment formation

In order to study the effect of temperature on Her7-Venus oscillation dynamics, we first have to define the criteria for temperature-compensated segment formation. Central to this question is whether embryos can form functional segments at the temperatures assayed. First of all, somites should be compensated for in terms of morphology, which includes size, shape and symmetry. Second, we have to take into account somite polarity, which involves the establishment of an anterior-posterior identity critical for downstream differentiation into vertebrae [48]. While both of these criteria are clearly important, somite size is the most straight-forward to quantify, and varies from 34.8-40.2  $\mu\text{m}$  in embryos grown at 15°C to 35°C. To enable comparison between temperature-dependent measurements, we can think about them in terms of their  $Q_{10}$  value. This parameter represents the change of rate experienced by a biological reaction in response to a 10°C increase in temperature, and tends to be close to 2-3 for most non-compensated reactions [151]. In the circadian oscillator field, reactions with a  $Q_{10}$  value between 0.85-1.15 are considered to be temperature-compensated [151, 152]. Although the  $Q_{10}$  value is generally applied to reaction rates, we can apply it here to represent the change in somite size along a 10°C interval.

In the results presented in this thesis, somite size has a  $Q_{10}$  of 0.84-0.96 between 15-35°C (see appendix in **section 8.2**). If we use the conventions from the circadian field, it follows that by this criterion alone somite size is temperature-compensated within this entire interval. However, when you also consider somite patterning, as scored by qualitative assessment of the posterior polarity marker *myf5*, polarity, and therefore function, is not temperature-compensated in samples grown at 15°C. Within the context of this thesis, although segment size may not be exactly the same between 27-35°C, segmentation is considered temperature-compensated based on the observation that *myf5* expression is correctly expressed. To more fully describe temperature-compensated segmentation, additional criteria which can affect downstream differentiation, such as somite shape and left-right symmetry will be addressed in future studies.

Interestingly, previous studies in zebrafish have found temperature-related differences in morphometry and swimming ability [153, 154]. Therefore, evaluating the effect of temperature on mature structures derived from correctly polarized somites such as the vertebrae and muscle would also be important to conclude whether somites are functionally compensated within this temperature range. For now, we can conclude that somite formation is temperature compensated between 27-35°C, but not at 15°C, which is also outside of the

range of normal development. Preliminary results suggest that development occurs normally between 17-26°C. To establish the full extent of temperature-compensated somitogenesis it would be important to extend the detailed analysis of somite polarity and size also to these temperatures.

### 5.1.3 The segmentation clock is not temperature-compensated

Knowing that segmentation can occur normally between 27-35°C, I next investigated how the underlying Her7-Venus oscillation dynamics change in response to temperature. In particular, the aim was to understand which aspects of dynamics would be predictive of temperature-compensated segment formation. It is important to note here that the somite size measurements presented above were taken from fixed embryos grown at different temperatures from the one-cell until the 8-9 somite stage. In contrast, quantifications of Her7-Venus oscillations were done in embryos that were grown at 27°C until the 12-somite stage, at which point the embryos were equilibrated to the different temperature conditions after dissection in preparation for imaging. Therefore, while we can draw first conclusions based on this data, the timing of temperature change needs to be taken into account. We can now build on these findings and compare to experiments in altered temperature conditions from the one-cell stage onwards.

Measurements of the segmentation clock period, corresponding to Her7-Venus2 oscillations in the posterior PSM of tail explants, revealed a  $Q_{10}$  value of 1.91 between 23°C and 35°C. Thus, unlike somite size, which has a  $Q_{10}$  of 0.86 along this interval, segmentation clock period almost doubles upon a 10°C decrease, and is therefore not temperature-compensated in medaka. This has previously been observed in zebrafish, where somite size is temperature-invariant, but segmentation period changes 3-fold between 20-30°C [26]. Hence, while segment size itself is compensated for, segmentation period is not.

Many basic biological processes show temperature-dependence in a similar way, including the timing of cell division, which is faster at higher temperatures [15]. Despite the apparently obvious effect of temperature on the rate of biochemical reactions, there are examples of oscillatory processes where period does not change with temperature. Notable among these is the circadian oscillator, which controls daily cycles of sleep and metabolism, where period is strictly maintained during temperature variation [151, 155]. Interestingly, the temperature-compensated circadian oscillator is still temperature-sensitive, and can be phase-shifted by entrainment to heat pulses [152]. Although some central period-determining reactions are temperature-compensated, compensation is not always reflected at the level of

individual components, and appears to emerge as a system-wide property in the circadian oscillator [151, 156]. Determining the temperature-sensitive and -insensitive components of the network to understand how this regulation is possible is a matter of ongoing research.

The biological importance of maintaining temperature compensation in some traits, but not others, can be linked to their function. In the circadian example, the ability of this oscillator to maintain a constant period is crucial to maintain its function in regulating daily rhythms. In contrast, if the period of segmentation clock oscillations were temperature compensated, they would not have been able to adapt to the overall altered developmental rate. Thus, by having a temperature-sensitive segmentation clock period, the developing embryo can still form polarized somites of roughly the same size.

#### 5.1.4 The period gradient changes with temperature

After establishing the temperature-dependence of Her7-Venus oscillations in the posterior PSM, the next logical step would be to quantify the effects of temperature on the other periods in the system. To this end, the Her7-Venus period gradient was measured between 23°C-37°C.

Knowing that the Her7-Venus oscillations in the posterior PSM have a  $Q_{10}$  value of 1.91, we might expect all the periods in the PSM to approximately double if the temperature is reduced by 10°C. Consequently, the slope and amplitude of the period gradient would be different between conditions, although in relative terms (as a percent change) the adjustment would be equivalent. However, a closer look at the data reveals that this is not the case. In fact, while the  $Q_{10}$  for period in the posterior PSM is 1.91, the corresponding value for the period in the anterior PSM is 1.62. Thus, the  $Q_{10}$  value is actually changing as a function of space. The observed changes to the period gradient can therefore not simply be explained by all the periods in the system slowing down or speeding up by the same factor. Theoretically, if a simple scaling would occur, the *relative* period gradient amplitude would remain constant during temperature variation, as a percent change. Instead, we see that the *absolute* period gradient amplitude is constant, remaining close to 20 minutes between 23-35°C. In other words, the absolute amount by which Her7 oscillations in a cell slow down before that cell is incorporated into the next somite is temperature-invariant.

The period gradient has previously been observed in the PSM of both zebrafish and mouse [74, 77]. Interestingly, when single cells are isolated from zebrafish PSM, the slowing

of Her1 oscillations continues, indicating that this is a cell-autonomous property [140]. Furthermore, the period gradient is spontaneously re-established following dissociation of mouse PSM cells [77]. Together, this implies that the period gradient could play a functional role in PSM patterning.

### 5.1.5 What is the functional relevance of a period gradient in the PSM?

One functional consequence of cell-intrinsic slowing of oscillations in space is highlighted in a situation where there is more than one oscillator in the PSM. This was first proposed in theoretical model by Goodwin and Cohen in 1969. This model is based on a system where two oscillating signals are propagated across the PSM with different dynamics such that the relative phase shift between the two signals changes as they progress from posterior to anterior. Consequently, cells can read out positional information based on this local phase shift [59]. In this way the signaling oscillations are not only carriers of temporal, but also spatial information.

Another model based on relative phase encoding was proposed in Lauschke et al in 2013, to explain the observation that segment formation always coincided with a  $2\pi$  phase shift in mouse PSM. Interestingly, this  $2\pi$  phase shift was maintained regardless of PSM size in a temperature-independent manner [72]. This model, referred to as the alpha model, takes a cell-centered approach: a cell in the posterior oscillates with an intrinsic period which exponentially slows down by a factor  $\alpha$  as the cell moves towards the anterior. The cell will stop oscillating and differentiate when it is phase-shifted by  $2\pi$  relative to the posterior PSM. The cell can decode phase-shift by means of a non-slowng reference oscillator within the same cell. Excitingly, we have evidence that waves of Notch and Wnt signaling activity can change their relative phase relationship as a function of space in the mouse PSM [137]. Specifically, Wnt signaling oscillations are expressed in a tissue-wide pulse, as expected from a reference oscillator. On the other hand, Notch signaling oscillations slow down to form a period gradient in space, and the resulting phase-difference between these two pathways therefore changes from out of phase in the posterior PSM, to in phase at the anterior PSM, where the next segment forms [86, 121, 124, 137].

The question remains whether accumulating the  $2\pi$  phase-shift in the alpha model is necessary for a cell to differentiate or if it just represents an indirect readout of a deeper mechanism. To test the functional role of phase-shift encoding, the phase-relationship between Wnt and Notch signaling was changed by using a microfluidic entrainment strategy to periodically pulse small-molecule inhibitors and activators of these two pathways.

Excitingly, when Wnt and Notch signaling were kept out of phase, cells in the PSM tissue oscillated for longer and segmentation was delayed [137]. This result supports the idea that the local phase shift is important for PSM patterning and segmentation.

The alpha model allows us to predict where and when a cell will differentiate if the rate by which its oscillations are slowing down, characterized by the parameter  $\alpha$ , is known. In other words, how the oscillation period in a cell slows down in time and hence in space will determine where it stops oscillating, effectively integrating spatial and temporal information in the same oscillatory signal.

### 5.1.6 The phase gradient is temperature-compensated

According to the alpha model framework, the change in period drives the accumulation of phase-shift, which in turn is assumed to encode positional information for somite differentiation. With this in mind, it is essential to understand how both the period and the phase gradient respond to changes in temperature. If relative phase-encoding has functional relevance, we would predict that the phase-shift along the PSM, corresponding to the phase gradient amplitude, is kept constant during segmentation at different temperatures. We therefore wondered whether this would be the case in medaka. For this reason the phase gradient was characterised between 23°C-37°C in Her7-Venus2 tail explants. Indeed, we found that both the shape and amplitude of the phase gradient were temperature-independent in medaka PSM between 23-37°C. The average phase gradient amplitude was calculated at  $4.69 \pm 1.79$  radians, corresponding to  $1.49 \pm 0.57\pi$  at 27°C, and this was value not significantly different at any of the temperatures tested between 23-37°C.

Interestingly, we have previously shown that also in mouse PSM, the phase gradient is temperature invariant, though the range of temperature that could be assessed was limited (i.e. 33°C and 37°C) [72]. My results in medaka show that both the absolute change in period (in minutes) and the absolute change in phase (in radians) along the PSM is temperature-independent in medaka tail explants. The fact that the phase-gradient amplitude is temperature-invariant during segmentation in the PSM is therefore compatible with the idea that oscillations can carry positional information by relative-phase encoding.

## 5.1.7 Challenging existing models of somitogenesis to explain temperature-compensated patterning

The experiments outlined above can be used not only to formulate a hypothesis for the mechanism of temperature compensation, but also to ask whether predictions from existing models of somite formation are compatible with my results. In addition to the models based on relative-phase encoding described above, the most commonly cited model is known as the “Clock and Wavefront model”, first proposed in 1976 [58]. The predictions that can be made from these models, and how we can move forward to test these predictions, will be considered in turn in the sections below.

### The alpha model

As described in more detail in **section 5.1.5**, in the alpha model positional information is encoded by means of relative phase-shift. In the temperature experiments presented here we have an independent way to change the period of oscillations. Interestingly, with the constraint that the period gradient amplitude is a constant 20 minutes between 23°C-35°C, and that the  $2\pi$  phase gradient is temperature-independent, the model would predict that the  $\alpha$  variable is proportional to the period in the posterior PSM (see appendix for full derivation). Thus, given that the period in the posterior PSM changes with temperature, it follows that there is a different  $\alpha$  for each condition. In other words, the rate of exponential slowing is temperature dependent.

Considering the experimentally-derived values for period and  $\alpha$ , we can use the model to plot the predicted rate of slowing in a given cell at a given temperature as a function of time. Comparing the predicted slowing to measurements of oscillation frequency will inform whether the alpha model can accurately model behaviour along this wide range of temperatures. In addition, further predictions can be made regarding the relationship between the posterior period in the PSM and  $\alpha$  for temperatures which have yet to be tested. Furthermore, the model can predict how long a cell would require to traverse the PSM at each temperature. Detailed experimental measurements for each prediction and characterisation of the corresponding somite morphology and polarity will allow us to challenge this model in the context of temperature compensation.

Finally, the validity of the alpha model can be tested by measuring the effect of temperature in the context of the medaka tailbud 2D-assay. This simplified context would allow us to assess the same predictions outlined above in the absence of confounding factors such as growth or cell movement.

## The clock and wavefront model

The regulation of somitogenesis is often described within the framework of the “Clock and Wavefront” model, proposed by Cooke and Zeeman in 1976 [58]. This model suggests that the position of somite boundaries is instructed by two independent factors - the “clock”, which encodes temporal information, and the “wavefront”, which encodes spatial information.

The clock is represented by a temporally periodic signal, which allows the tissue to switch, at a defined periodicity, between permissive and non-permissive states for differentiation. Simultaneously, the position of the next somite boundary is set by a wavefront of “cellular change” which regresses in the anterior-to-posterior direction with embryo elongation. Following wavefront regression, a somite forms when the cells in that region enter the permissive state to differentiate. The position of somite boundaries is therefore determined by the intersection between these two independent elements. In mouse and chick, the clock is widely believed to be a network of Notch, Wnt and FGF signaling oscillations [86, 124], whereas the wavefront is thought to be delimited by Wnt and FGF signaling gradients [108, 109, 121]. In zebrafish, Wnt and FGF signaling gradients are equivalent to what has been observed in higher vertebrates. However only Notch signaling oscillations have been linked to the clock mechanism so far [86, 107, 110].

According to this model, segment size  $S$  is determined by the speed of wavefront regression  $V$  multiplied by the oscillation period  $T$ , in other words, how far the wavefront moves for the duration of one period:

$$S = V \times T$$

In the context of the temperature effects presented here, for somite size to remain relatively constant, the velocity of the wavefront needs to inversely correlate with the oscillation period as temperature changes. Given that the segmentation clock period decreases by more than 2-fold between 23°C and 35°C, the speed of wavefront regression would have to increase by the same factor. To directly address how the wavefront changes in various temperature conditions, quantitative insight into signaling gradient dynamics is required. To this end, the *Ctnnb1-Venus* and *Snai1a-Venus* lines can be used to obtain direct measurements of the signaling gradients in the PSM during changes in temperature. Thus, future experiments can combine measurements of segmentation clock oscillations and signaling gradients at different temperatures to see whether or not these fit the predictions of the model.

## 5.1.8 Is relative-phase encoding a plausible mechanism in medaka?

In the context of robustness to temperature, models based on relative phase encoding offer a simple solution to the problem of maintaining correct segment size. Both spatial and temporal information are carried within the relative-phase shift between two traveling waves, which are assumed to have similar regulatory mechanisms. The relative difference between them would therefore remain the same if their speed changes by the same factor. In contrast, encoding of space and time in the clock and wavefront model is based on two independently regulated elements. The models based on relative phase-shift encoding also assign an important functional role to the period gradient. However, these models implicate the presence of a second oscillator. As described in **section 5.1.5**, we have evidence in mouse that this second oscillator could be Wnt signaling oscillations, which shows a changing phase-relationship with Notch signaling oscillations along the PSM [137]. In contrast, only Notch signaling oscillations have been identified in the PSM of zebrafish so far [86].

## 5.1.9 Looking for a second oscillator in medaka using the Wnt and FGF signaling reporter lines

Axin2 is known to oscillate in the mouse PSM downstream of Wnt signaling activity, and changes its phase relationship to Notch signaling oscillations as a function of space [121, 137]. This gene could therefore be a readout of the reference oscillator. The Axin2 ortholog is also predicted to be oscillatory in chicken PSM, but not in fish so far [86]. With this in mind, we were interested in exploring whether Wnt signaling oscillations might be present in medaka. However, unlike the expression patterns of Axin2 in mouse [121], there was no clear evidence of oscillatory expression of either of the two *axin2* paralogs in medaka. In addition, signaling oscillations were not detectable in the Axin2.1-Venus line.

The Snail family of transcription factors, which are under the control of Wnt and FGF signaling, are also oscillatory in the PSM of higher vertebrates. Specifically, Snai1 oscillates in the mouse PSM, and Snai2 oscillates in the chick PSM [129]. There are two Snail orthologs expressed in medaka PSM: *snai1a* and *snai2* [144]. *snai2* is only expressed in the anterior PSM and seems to shift its anterior position in time with somite formation. Interestingly, Snai1a is expressed in a U-shaped domain similar to the Her7 expression pattern, with the anterior front of this domain seemingly changing in intensity between stage-

matched embryos, hinting at the possibility of oscillations [144]. These dynamic expression patterns motivated us to generate a *Snai1a*-Venus knock-in line. So far, *Snai1a*-Venus protein oscillations could not be detected in this line, although the signal does appear dynamic at the anterior.

Despite the absence of clear oscillations, in-depth characterisation of the *Snai1a*-Venus and *Axin2.1*-Venus lines is necessary to rule out their existence. Quantification of dynamics is not straightforward and could be hampered by the weak endogenous expression in these lines. To increase the expression levels, these lines are currently being bred to homozygosity.

### 5.1.10 *Her7* paralogs could fulfill the requirements of a “second oscillator”

Although we lack evidence for oscillatory signaling in the Wnt and FGF pathways in medaka and zebrafish, there are multiple oscillating candidates within the Notch signaling-regulated *Her* family which could potentially act as a reference oscillator. Importantly, a relevant candidate oscillator would have to change its phase-relationship with *Her7* as a function of space in the PSM.

In zebrafish, *her7* expression overlaps with *her1* expression during all phases of oscillation [64, 157]. Interestingly, previous ISH studies have shown that expression of *her12*, an ortholog of mouse *Hes5*, appears to change its phase-relationship with *her1* and *her7* in zebrafish PSM. Specifically, while expression of the two overlaps in the tailbud, they are anti-phase in the anterior PSM [65, 98]. The corresponding medaka *her12* ortholog is also oscillatory in the PSM [65], and if this phase-relationship is conserved in medaka PSM, the *her12* gene could be a good candidate for a second oscillator. A similar, although more subtle, situation has been observed when comparing the phases of *her1/11* and *her5* (both orthologs of mouse *Hes7*) along the PSM in medaka [65]. To explore the potential for relative phase-shift encoding in medaka, the phase-relationship between these genes will have to be characterised in more detail.

Another interesting candidate is *her13.2*, the medaka and zebrafish ortholog of mouse *Hes6* [65, 106]. In zebrafish, *her13.2* is not clearly oscillating but is rather graded along the PSM [65]. Similarly, *her13.2* (and *her13.1*) oscillations are not visible in medaka but their expression pattern has the characteristic posterior U-shaped domain with an anterior wave-like pattern of other oscillatory *Her* genes. Interestingly, *her13.2* has been

proposed to set the timing of oscillations by affecting the period of the segmentation clock [106]. Furthermore, unlike the other *Hes/her* family proteins, *her13.2* appears to be Notch-Delta independent in both *Xenopus* and zebrafish [65, 158]. Instead, *her13.2* expression is regulated by FGF signaling [105]. For these reasons, it would be interesting to explore whether *her13.2* expression indeed oscillates in the PSM. If this gene does oscillate it could be considered FGF signaling activity rather than Notch signaling activity.

## 5.2 Exploring robustness to variation in levels of Her7

A widely cited advantage of dynamic signal encoding is the increased robustness to perturbations and noise [103, 159]. With this in mind, we wondered how oscillation dynamics would be affected in the Her7-Venus1 line, which is a hypomorph for Her7 levels. Contrasting the phenotype (or lack thereof) in the Her7-Venus2 line with the Her7-Venus1 and the Her7 knockout line could shed light on how information is encoded in oscillatory behaviour.

### 5.2.1 Her7 is essential for medaka segmentation

To study whether *her7* is at all required for normal somitogenesis in medaka, a *her7* CRISPR knockout was generated. The *her7* knockout phenotype in homozygous embryos is characterised by irregular somite morphology, disorganized boundary formation and left-right asymmetry starting from the first somites. At the molecular level, the disorganized expression of the posterior somite marker *myf5* indicates a loss of somite polarity. From the ISH analysis of the medaka *her7* knockout line, I also found that the oscillatory expression of *her1/11* is lost in the absence of *her7*. Instead, *her1/11* expression appears upregulated in the whole previously oscillating domain. A similar mechanism of *her7*-mediated regulation of both *her1* and *her11* in zebrafish has previously been shown and will be discussed further in **section 5.3.2** and **5.3.3** [94, 95, 157]. Together, our findings indicate that *her7* is essential for somitogenesis medaka, and that it controls the oscillatory expression of *her1/11*.

## 5.2.2 Reduced levels of Her7 in the Her7-Venus1 line can sustain normal segmentation in embryos

While we know that normal segmentation cannot occur without *her7*, how much *her7* expression is really necessary to sustain oscillatory behaviour and normal segmentation? An unexpected consequence of integration of Venus was the downregulation of *her7* RNA in Her7-Venus1 homozygotes. On the one hand, the loss of *her7* expression could be caused by a decrease of transcript stability or transcription rate in Her7-Venus1 embryos. On the other hand, Her7 is an auto-repressive transcription factor, so the reduced expression could also be explained by an increase in protein levels or protein stability. In support of this, overexpression of either *her7* and *her1* in zebrafish was shown to repress both *her7* and *her1* [97]. From the *her7* knockout line presented in this thesis, we know that *her7* regulates *her1/11* expression in medaka. Thus, it can be reasoned that if the Her7-Venus1 knock-in had caused an increase in Her7 protein stability, and subsequently auto-repressive activity, it would also affect the expression of *her1/11*, and possibly its paralog *her5*. On the contrary, both *her1/11* and *her5* expression was comparable to wildtype in both dynamics and intensity. This result argues against an increased protein stability and/or auto-repressive activity of Her7.

As estimated by comparing the fluorescence signal intensity between the Her7-Venus lines before and after vector backbone removal, the Her7-Venus1 is a hypomorph with about 74-76% of the protein levels seen in the Her7-Venus2 line (**figure 18**). However, when looking at the corresponding RNA levels, it appears that the downregulation in homozygotes is far greater than what is implied from the fluorescence measurements. This observation needs to be confirmed by qPCR.

From the extent of this loss of *her7* expression, it would be reasonable to expect a phenotype in Her7-Venus embryos. On the contrary, validation experiments showed that both Her7-Venus1 and Her7-Venus2 lines can be kept as viable homozygotes, with no obvious phenotype visible in embryos. In particular, somite polarity and PSM pre-patterning is indistinguishable from wildtype embryos where assessed (until the 9-10 somite stage). However, a phenotype in the Her7-Venus1 line does become apparent at post-embryonic stages. Specifically, Her7-Venus1 hatchlings form between 14-23 regular segments, before showing signs of fused, irregular segmentation in the posterior-most vertebrae. This could indicate a phenotype affecting the pre-patterning of later somites. To address this, somite polarity markers should be assessed in somites 14-23. Furthermore, if the downregulation of

*her7* expression in Her7-Venus1 embryos is the cause of this segmentation phenotype, we can expect to see an improvement in Her7-Venus2 hatchlings. To this end, we are currently evaluating the segmentation phenotype in the Her7-Venus2 line.

Knowing that *her7* controls *her1/11* oscillations, the extent to which *her7* is downregulated is also not enough to disrupt oscillations in the paralogs. Thus, the strong downregulation of *her7* expression levels seen in the Her7-Venus1 line would suggest that very little Her7 is enough to sustain normal segmentation and *her1/11* expression. This is also supported by the fact that embryos which are heterozygous for *her7* do not show any obvious signs of impaired somitogenesis (data not shown), although a detailed investigation has yet to be carried out. Interestingly, robustness to a reduction in Notch signaling levels has previously been observed in a mouse hypomorph of the NICD [160], which also oscillates in mouse PSM [78, 84]. Homozygous NICD hypomorph embryos show severe morphological defects in most of the body- yet somite formation and polarity are remarkably well maintained [160]. Together, these experiments demonstrate the potential of oscillatory signals to be robust to noise and signaling levels.

### 5.2.3 The period of oscillations is robust to changes in *her7* levels

A careful inspection of the Her7 oscillations in the two reporter lines generated (Her7-Venus1 and Her7-Venus2) showed that while signal intensity is reduced in Her7-Venus1 embryos, oscillation period is not significantly different between the two. Furthermore, in both lines, the oscillation period is the same in heterozygous (with one wildtype and one tagged *her7* allele) and homozygous (with two tagged *her7* alleles) embryos. This data indicates that the endogenous knock-in of Venus does not significantly affect Her7 protein function. It also suggests that Her7 period is robust in the face of a significant loss of signaling levels.

The basic mechanism for the generation of Hes/*her* oscillations is proposed to involve delayed auto-regulatory negative feedback loops [103, 104]. The delay is necessary to enable the autonomous generation of oscillations, without the need for any additional intermediate components [104]. Mathematical modeling by Lewis and Monk based on this simple principle was able to recapitulate the period of *her1/her7* oscillations in zebrafish [103] and Hes1 oscillations in mouse [104]. The Lewis model proposed that a delay consisting of the total length of transcription, RNA processing, export and translation is the main determinant for the period of oscillation in Her transcription factors [103]. If this is true,

absolute levels of *Hes/her* RNA and protein should be less important than this delay in determining the period of oscillations. To test this assumption, the Lewis model was used to test the effects of reducing protein production. Interestingly, a 90% reduction of protein production still allows for robust oscillations with no change in period. A further 95% reduction will still allow for oscillations with the same period, although these are progressively dampened [103]. If the reduced protein production tested in the model is equivalent to the reduced *her7* RNA in the Her7-Venus1 line, the results from the Lewis model fit with the observation that period is not affected in Her7-Venus1 embryos. Furthermore, the segmentation phenotype which is visible in the last 14-23 segments of Her7-Venus1 hatchlings could be compatible with the oscillatory dampening described.

In contrast to the robustness of *her7* to signaling levels demonstrated in this thesis, previous experiments have shown the the protein half-life of HES7 is crucial to proper segmentation. Specifically, an 8 minute increase in half-life from the wildtype 22 minutes caused loss of normal somite-prepatterning, morphology and coherent oscillations [130]. Interestingly, this phenotype only appeared after 3-4 normal somites had already formed. This change in half-life could be explained by mathematical modelling where oscillations are damped after the first few peaks. The delayed negative feedback in the Monk model agrees with this result [104]. In this model, protein half-life has a large impact on oscillation period. Given that medaka oscillation period is shorter than in mouse, if the fusion of Venus to endogenous Her7 would have impacted protein stability by a few minutes, this would likely have resulted in a visible phenotype. In the light of this model, the results presented here argue against any significant change in half-life to the Her7-Venus fusion protein.

## 5.3 A comparative analysis of Hes/Her dynamics and function in medaka, mouse and zebrafish

Both the mouse and zebrafish models are well established in the field of somitogenesis and, together with studies in chick, form the basis of the majority of our knowledge in this field. To complement existing vertebrate models, segmentation clock oscillations were characterised in medaka.

In both zebrafish and medaka, a whole genome duplication early in the teleost fish lineage is thought to be responsible for a large number of paralogs in these species relative to mouse. Redundant copies of individual genes may have gained or lost function, or become complementary (non-redundant) by sub-function partitioning. zebrafish and medaka

are at least 110 million years apart, and in many cases it seems that their duplicated genes have evolved differently. Mutant phenotypes from the two species can therefore be used in comparative studies to reveal the evolution of functional differences between genes. The presence of redundant genes also makes it possible to study mutants which are lethal at early stages or cause haploinsufficiency in mice [32, 33, 161, gajewski 2006]

### 5.3.1 Oscillation dynamics in medaka, zebrafish and mouse

The mouse *Hes7* gene, thought to be the core regulator of Notch signaling oscillations, is orthologous to zebrafish *her7*, *her1*, *her5* and *her11*, and medaka *her7*, *her5* and *her1/11* [57, 65]. With the exception of zebrafish *her5*, all of these *her* genes are oscillatory in the PSM of both species. Qualitative analysis reveals that the expression patterns of the medaka orthologs are more similar to higher vertebrates [65]. In particular, expression in zebrafish is characterised by a U-shaped domain and two discrete domains in the anterior, suggestive of multiple travelling phase waves (see **figure 3**, in **section 1.3.6**). On the other hand, in medaka, mouse and chick the U-shaped domain is only accompanied by a single discrete anterior domain, suggestive of one travelling phase wave. The meaning of the additional waves of *her* gene expression is unclear, but has been suggested to be due to differences in RNA stability. Whether the presence of extra waves is a derived or ancestral feature, it is clear that zebrafish is not representative for all lower vertebrates, or even teleost fish [65].

The Her7-Venus knock-in lines enable quantification of Her7 protein oscillations in medaka for the first time. Live imaging of intact embryos and tail explants demonstrates that Her7-Venus oscillations show a striking similarity to Notch signaling oscillations in the mouse PSM. First of all, the PSM of medaka and mouse are similar in that embryos grow from the posterior while somites form at the anterior, keeping the size of the oscillatory field relatively constant. This is different from Notch signaling oscillations in zebrafish, where the oscillatory field gradually shrinks as somites form [46, 75]. Furthermore, Her7-Venus protein dynamics mirrors the RNA expression patterns described above in that the oscillations form a single coherent wave of expression along the PSM. In contrast, the corresponding expression of Her7 protein in zebrafish occurs in two-three waves [75]. In fact, in zebrafish the number of waves present in the PSM decreases over developmental time, from 2.5 to close to 1 between segment 7 and 21 Soroldoni, 2014 #223}. This decrease in wave number as the tissue shrinks is contrary to what happens in *lfn3*-Venus oscillations in mouse PSM, where

the wave number remains constant (close to 1) irrespective of PSM size as long as the tissue is segmenting [72].

### 5.3.2 Medaka *her7* is functionally equivalent to the combination of zebrafish *her7* and *her1*

Most of the functional insight we have for the duplicated genes in the *her* gene family come from studies in zebrafish. In zebrafish, the core oscillation mechanism for Notch signaling oscillations is thought to be mediated by the combined action of *her7* and *her1* [95]. Given that the *her7* and *her1* genes are located head-to-head 18.5 kb apart in the genome, and the fact that these paralogs have an overlapping expression pattern have led many to suggest that they are controlled by shared regulatory elements [64, 65, 157]. Despite this, loss of function studies targeting *her7* and *her1* individually or simultaneously have revealed complementary functions for these paralogs [64, 93, 96]. Specifically, *her7* knockout or knockdown causes disrupted somite polarity, enlarged somites and incomplete boundaries, but this is restricted to somites 8-17. On the other hand, *her1* knockout or knockdown embryos only show defects in somites 1-3 [93, 96]. A more severe phenotype where all somites are affected only occurs when both *her7* and *her1* are lost, such as in a mutant lacking this whole genomic region or in a double morpholino knockdown of *her1* and *her7* [64, 93].

In the medaka *her7* knockout presented here, somite polarity and morphology is impaired along the whole axis at stage 22 (9-10 somites). This is similar to what has been observed in the mouse *Hes7* knockout, where embryos show defects in boundary formation, symmetry and somite patterning along the entire anterior-posterior axis [89].

The loss of function studies for zebrafish *her7* and *her1* reveal that these paralogs seem to play separate, complementary functions in zebrafish PSM. Since a comparable phenotype in medaka can be achieved by knocking out *her7* alone, this gene in medaka appears to functionally replace both *her7* and *her1* in zebrafish. Interestingly, *her7* in medaka therefore appears to be more functionally similar to *Hes7* in mouse relative to *her7* in zebrafish.

### 5.3.3 Medaka *her1/11* is functionally more related to zebrafish *her11* than *her1*

In addition to *her7* and *her1*, zebrafish *her11* is the last zebrafish gene orthologous to mouse *Hes7* which oscillates in the PSM [65]. While oscillatory *her1* expression overlaps with *her7* expression [64, 157], *her11* is not expressed in posterior PSM, but is rather expressed in two stripes in the anterior PSM which overlap with the anterior domain of *her1/her7* oscillations [65, 94]. In addition, *her11* can be found in the midbrain-hindbrain boundary [94]. When the *Hes7* orthologs were characterised in medaka, Gajewski et al. found *her7*, corresponding to zebrafish *her7*, *her5*, which is not expressed in zebrafish PSM and *her1/11*, which combines the expression patterns of the zebrafish *her1* and *her11* genes [65].

One unanswered question involves whether medaka *her1/11* is functionally as important as *her1* in zebrafish. As discussed above, *her1* plays a complementary role with *her7* in zebrafish somitogenesis, and the loss of this gene causes a clear phenotype in early somites [93, 96]. Due to the central role of *her7* and *her1* in zebrafish, the medaka *her1/11* ortholog is sometimes implied to have equal functional importance to medaka *her7* [101]. However, morpholino knockdown of medaka *her1/11* does not cause the severe phenotype seen after loss of zebrafish *her1*, with *myf5* staining comparable to wildtype, indicating normal somite polarity [101]. In addition, the results presented in this thesis demonstrate that loss of medaka *her7* alone is sufficient to cause a severe phenotype in somite polarity and morphology along the whole axis, without the need for additional knockout of *her1/11*. Therefore, medaka *her1/11* does not appear to be functionally equivalent to zebrafish *her1*.

Previous studies in zebrafish have shown that the oscillatory expression of *her11* is dependent on both *her7* and *her1* expression, with the loss of *her1* being the mildest, loss of *her7* having a more severe effect, and loss of both causing completely uniform expression of *her11* in the whole PSM [94]. Thus, only the loss of both *her7* and *her1* results in a *her11* expression phenotype in zebrafish which is comparable to *her1/11* expression in the medaka *her7* knockout. Together, this evidence seems to support that medaka *her1/11* is more similar to zebrafish *her11* than zebrafish *her1*.

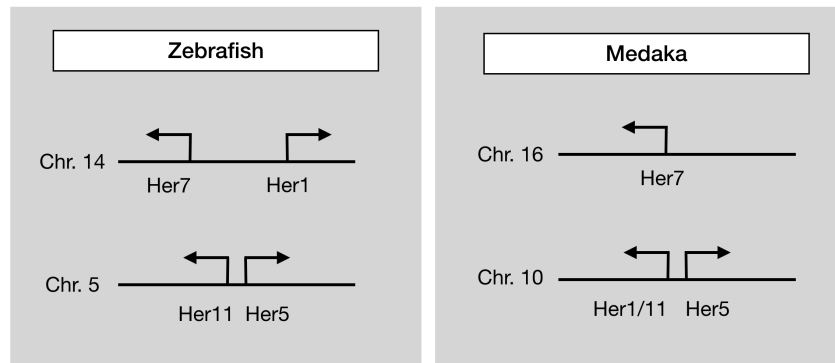


**Figure 40:** Schematic representing the genomic organization of the mouse *Hes7* orthologs in zebrafish and medaka (based on Gajewski et al. [65]).

From phylogenetic analysis based on amino acid sequence, medaka *her1/11* is orthologous to both zebrafish *her1* and *her11*, although it appears closer to *her1* [65]. However, from gene synteny analysis (see figure 40) medaka *her1/11* is adjacent to *her5*, organized in the same manner as zebrafish *her11* and *her5* [65]. If genetic linkage is used as a proxy for similarity between these genes, the genomic organization of these genes supports that medaka *her1/11* is more related to zebrafish *her11* rather than *her1*. However, this may not be trivial, and due to the high similarity between these paralogs it is not straightforward to make functional comparisons across species.

In summary, *her7* and *her1* in zebrafish jointly regulate the core clock mechanism in zebrafish, and are upstream of *her11* oscillations [94, 95, 98]. In medaka *her7* is the functional equivalent of zebrafish *her7/her1*, and is likely upstream of *her1/11*. To confirm that this is the case, it would be necessary to look at the expression of *her7* upon loss of *her1/11* in medaka. The effect of the medaka *her7* knockout on *her5* (the third *Hes7* ortholog), which unlike its zebrafish counterpart is expressed in the PSM in an oscillatory manner [65], has not yet been evaluated. Taken together, this indicates a difference in the regulation of somitogenesis between these two fish species, and confirms that medaka *her7* is essential for correct somite patterning.

## 6. Outlook

The medaka Her7-Venus knock-in line allows us to quantify endogenous segmentation clock oscillations for the first time. Excitingly, live imaging of this fusion protein enables the study of how signaling dynamics change at a wide range of temperatures *in vivo*. The results presented here allow us to start formulating a hypothesis about the functional role of the phase and period gradient for normal segmentation.

In the future, it would be important to measure somite size and polarity at a wider range of temperatures to precisely define the region within which temperature-compensated somite formation occurs. To study how development responds to temperature on a longer time-scale, it is also necessary to score whether morphology of somite derivatives, such as the vertebrae are affected. With this information in hand, we can more precisely define how much variability in morphology and patterning falls within the definition of temperature-compensation.

Beyond somitogenesis, it would be interesting to extend this analysis to the effect of temperature on other morphological features. Interestingly, pre-patterning does not have to occur in the same way at different temperatures, but can still be coordinated so that the final pattern is functionally compensated. In connection to this, it has previously been reported that the relative timing of appearance for different developmental landmarks may vary with temperature during development of herring and *Drosophila* embryos [9, 162].

To understand what changes between permissive and non-permissive temperatures- it would be interesting to explore how dynamics are affected at the extremes of compensation where the system breaks down. Another exciting challenge will involve the study of how dynamics respond to temperature fluctuations. This could involve smooth transitions, such as would be experienced by embryos in their natural habitats, but also sharp temperature steps. Interestingly, heat-shock in zebrafish sometimes causes the formation of one smaller somite, followed by a larger one [107]. Having access to the underlying dynamics during this type of perturbation could inform how dynamics have to change for this to be possible. An additional dimension could involve exploring whether embryos with sensitised backgrounds are equally robust to temperature variation. For example, the Her7-Venus1 line can be used as a hypomorph for Her7 levels, or the Notch inhibitor DAPT can be used to disrupt intercellular communication. Applying different

temperatures in these backgrounds may reveal which aspects of the system contribute to maintaining phenotypic robustness.

Finally, the measurements of Her7-Venus oscillations can be complemented with measurements of Wnt and FGF signaling dynamics, which are also thought to be related to embryo growth. This would be important to address axis elongation, together with the role of cell proliferation and cell movement, which are known to be highly correlated with temperature. To put these results into the context of existing models for somitogenesis, we can focus on testable predictions and use this to distinguish between them. Together, the sum of all of these influencing factors will allow us to form a more complete picture of temperature-compensated development

## 7. Materials and methods

### 7.1 List of genes referenced in this study

**Table 10:** List of genes and ENSEMBL identifiers referenced in this study, using the Japanese Medaka HdrR genome (ASM223467v1)

Gene name	Mouse ortholog	ENSEMBL ID	Chromosome
Axin2.1	Axin2	ENSORLG00000001945	1
Axin2.2	Axin2	ENSORLG00000008893	8
Ctnnb1	Ctnnb1	ENSORLG00000005845	16
Her7	Hes7	ENSORLG00000016162	16
Her5	Hes7	ENSORLG00000009833	10
Her1/11	Hes7	ENSORLG00000010016	10
Her4.2	Hes5	ENSORLG00000003974	7
Her12	Hes5	ENSORLG00000003967	7
Mesogenin (msgn1)	Msgn1	ENSORLG00000014828	24
Mesp-a	Mesp2	ENSORLG00000014659	3
Myf5	Myf5	ENSORLG00000016257	23
Snai1a	Snai1	ENSORLG00000023047	5

### 7.2 Generation of medaka lines by CRISPR/Cas9

CRISPR technology, originally derived from bacterial adaptive immunity, is based on the nuclease activity of Cas9 protein, whose specificity is defined by the interaction of two RNA sequences (crRNA and trcrRNA). These sequences can be combined to form a single guide RNA (sgRNA) [163]. The CRISPR target sequence can be any 20 nucleotides, with the only limitation that these are immediately followed by a 3-base pair protospacer-adjacent motif (PAM). When a sgRNA-guided Cas9 reaches its target site, it will cut between 3-4 base pairs upstream of the PAM. The commonly used *Streptococcus pyogenes* Cas9 most efficiently cleaves NGG-type PAMs, but can also cut at NAG-type PAMs with about 20% efficiency [164].

When a double-strand break is introduced in the genome, the endogenous DNA repair machinery can either bridge the gap by homology-directed repair (HDR) or non-homologous end-joining (NHEJ). While HDR uses homologous template DNA to accurately repair the

lesion, NHEJ rather produces random indels that can lead to frameshifts and gene knockouts [164].

Endogenously tagged medaka fusion protein lines were generated using CRISPR-mediated homology-directed repair. The design of the sgRNAs and donor vector were done with Thomas Thumberger (Wittbrodt lab). Cloning of the Her7-Venus and Ctnnb1-Venus donor constructs was carried out by Kristina Stapornwongkul.

## 7.2.1 sgRNA design

To identify sgRNA candidates for endogenous CRISPR knock-ins, target sequences for each gene (100bp upstream and 50bp downstream of the stop codon) were analysed using the online sgRNA target predictor tool CCTop [165] with the parameters listed in **table 11**. Target sites were chosen to be as close as possible to the desired location of the DSB (within 10-20 bp). Since sgRNA target sites have to be mutated in the final donor sequence, target sites in the CDS were preferred over those which bind after the stop codon, as this could affect 3' regulatory sequences. Lastly, sgRNAs were evaluated for their potential off-target effects. Although sgRNAs are most efficient when they completely match their target sequence, they can have some off-target activity at highly similar sequences. In general, more than 2 mismatches at the core (the 12 bp closest to the PAM), or 4 mismatches in total will not lead to cutting by Cas9 [165]. However, anything less than that could potentially be an off-target site. Therefore, the location of potential off-target sites (using both NGG and NAG PAMs) was taken into consideration when choosing sgRNA targets, avoiding those which have partial matches to other known coding sequences. Final sgRNAs are listed in **table 12**.

To verify if sgRNA target sites were indeed present in our wildtype medaka colony, the targeted region was amplified for sequencing. Primers for amplification were designed to bind outside the region of homology used in the donors, so that they could be used again during later PCR screening for in-frame integrations (listed in **table 25**, under category "full integration").

**Table 11:** Input parameters for the design of sgRNAs using the CCTop tool [165]

Setting	Input
PAM type	NGG-NRG (NGG target, NGG/NAG evaluation)
Target site length	20
Core length	12
Overhangs for IVT	TAGG/AAAC (T7)
Max total mismatches	4
Max core mismatches	2
Genome	Japanese medaka HdrR

**Table 12:** list of sgRNAs and target sites used for CRISPR lines

sgRNA	Target sequence 5'-> 3' (PAM in bold)	Oligos for cloning (Fwd+Rev)
her7_T8	GCCAGACTCTGTGGAGGCC <b>TGG</b>	TAgGCCAGACTCTGTGGAGGCC
		AAACGGGCCTCCACAGAGTCTGG
her7_T9	TTGGTGACCGGGTCAGGGCC <b>AGG</b>	TAggTTGGTGACCGGGTCAGGGCC
		AAACGGCCCTGACCCGGTCACCAA
ctnb1_T6	GGGATTCAAACCAACTGGC <b>TGG</b>	TAGGGATTCAAACCAACTGGCC
		AAACGGCCAGTTGGTTTGAATC
ctnb1_T14	ATGTTTATCTCGGTATTTAC <b>AGG</b>	TAggATGTTTATCTCGGTATTTAC
		AAACGTAAATACCGAGATAAACAT
axin2.1_T2	ATGTACGAGGGCAAGGC <b>TGGG</b>	TAggGTACGAGGGCAAGGCCT
		AAACAGGACCTTGCCCTCGTAC
axin2.1_T6	CGAGGGCAAGGC <b>TGGGCAAGG</b>	TAggAGGGCAAGGCCTGGGCA
		AAACTGCCCAGGACCTTGCCCT
snai1a_T2	CGTGGGGTCTCACACTGAGG <b>TGG</b>	TAggTGGGGTCTCACACTGAGG
		AAACCCTCAGTGTGAGACCCCA
snai1a_T3	ACTCGTGGGGTCTCACACTG <b>AGG</b>	TAggTCGTGGGGTCTCACACTG

		AAACCAGTGTGAGACCCACGA
her7_3'HF_T11	TCCTTTGAATAAATAACGGGTGG	TAggCTTTGAATAAATAACGGG
		AAACCCCGTTATTTATTCAAAG
her7_3'HF_T12	TAGCAGTTATTCCATCGGCACGG	TAggGCAGTTATTCCATCGGCA
		AAACTGCCGATGGAATAACTGC
her7_KO_T9	AAAGTTACTAAAATCTCAGGTGG	TAggAGTTACTAAAATCTCAGG
		AAACCCTGAGATTTTAGTAACT
her7_KO_T1	CATCCCGGAAGGACTGCTTCTGG	TAggTCCCGGAAGGACTGCTTC
		AAACGAAGCAGTCCTTCCGGGA

## 7.2.2 sgRNA synthesis

Once the appropriate targets were selected, oligos with overhangs for plasmid ligation (forward: 5' TAGG 3'/reverse: 5' AAAC 3') were ordered from Sigma Aldrich. For the forward oligo, the GG in the overhang is necessary to ensure efficient transcription by T7. To anneal oligo pairs, 1  $\mu$ l of each (forward and reverse, 100  $\mu$ M concentration) was mixed with 20  $\mu$ l of dH<sub>2</sub>O and 18  $\mu$ l annealing buffer (10 mM Tris pH 7.5-8, 30 mM NaCl) and heated to 95°C, and gradually cooled to 10°C in the PCR machine as shown in **table 13**.

**Table 13:** PCR settings for oligo annealing

Temperature	Duration
95°C	5 min
Ramp down to 70°C (0.1°C/sec)	
70°C	10 min
Ramp down to 65°C (0.1°C/sec)	
65°C	10 min
Ramp down to 60°C (0.1°C/sec)	
60°C	10 min

Ramp down to 10°C (0.1°C/sec)

10°C	hold
------	------

Annealed oligos were diluted 1:33 and ligated into plasmid DR274 (addgene nr. 42250, [166]) pre-digested with Bsa-I (also known as Eco31I, Thermo Fischer, FD0293). In the DR274 plasmid, the locus-specific target site will be inserted in frame with the remaining sgRNA sequence and a T7 promoter. For sgRNA production, 10 µg of each plasmid was linearised overnight with Dra-I (ThermoFisher, FD0224) and the resulting fragments were separated by gel electrophoresis. The 300 bp band was excised and purified, and used as a template for *in vitro* transcription from the T7 promoter using the Megshortscript kit (ThermoFisher, AM1354). Following transcription, RNA cleanup was performed using the RnEasy minElute cleanup kit (Qiagen, 74204). Successful transcription and cleanup of sgRNAs was confirmed by agarose gel. sgRNAs were stored at -80°C until use.

### 7.2.3 Testing sgRNA efficiency

*In vitro* testing of sgRNAs to determine whether they would cut the targeted locus was carried out according to the Wittbrodt lab protocol. TOPO plasmids containing the targeted region generated for verification of locus integrity (see **section 7.2.1**) were used as DNA templates for the reaction. The *in vitro* assay works best if there are at least 900 bp between the target site and the end of the DNA. With this in mind, 1 µg of each plasmid was linearised, avoiding internal restriction sites. Following DNA purification, the linear template was then mixed with the corresponding sgRNA and Cas9 protein (NEB, M0386) as shown in **table 14**, and incubated at 37°C for 1.5 hours. All sgRNAs tested were found to cut their corresponding targeted locus *in vitro*.

**Table 14:** Components for in-vitro testing of sgRNAs

Component	Volume	Final concentration
Linear plasmid	-	200 ng
sgRNA (15 ng/µl)	2 µl	30 ng
Cas9 protein (1 µM)	1 µl	30 nM
10x buffer 3.1	3 µl	1x
Nuclease-free dH2O	To 30 µl	-

Even if an sgRNA works *in vitro*, the efficiency of cutting could change in an *in vivo* context. Therefore, a subset of embryos were sacrificed after injection to check for in-frame 5' integrations by PCR, using primers listed in **table 25**. All sgRNAs tested showed in-frame integrations in sacrificed embryos, except *ctnnb1\_T14*. To find out if this sgRNA was even cutting the locus at all, primer nr. 5 and 54 were used to amplify a 155 bp region around the cutsite in DNA from injected embryos. The resulting amplicons were sequenced with primer nr. 5 (GATC Biotech/Eurofins genomics). Normally, if the sgRNA is active, sequencing will show multiple peaks in the vicinity of the cutsite. On the contrary, samples injected with *ctnnb1\_T14* showed clean peaks in all samples, confirming that no editing was detectable. Therefore only *ctnnb1\_T6* was used to generate the Ctnnb1-Venus line.

## 7.2.4 Donor vector design

To facilitate homologous knock-in of Venus fluorescent protein, donor vectors were created for each line. Following a strategy developed in the Wittbrodt lab, donor vectors were designed so that they would be linearised upon injection *in vivo*. For *in vivo* linearisation, an orthogonal sgRNA target site was inserted before the start of the homology arms, referred to as the "C13" site. This target site is recognized by a highly efficient sgRNA which was originally designed to cut GFP. Due to the high sequence similarity between GFP and mVenus, the C13 site therefore had to be mutated in the mVenus sequence used for the donor vectors. The Venus sequence used for all endogenous knock-in lines was cloned into the EV3 entry vector by Kristina Stapornwongkul (Master thesis). In some cases the plasmid donor was replaced with 5'biotinylated long dsDNA donors, which were shown to facilitate single copy integration and a higher HDR efficiency [37].

## 7.2.5 Cloning of homology arms for donor vectors

Homology arms (ranging between 400-1000 bp) were chosen to match the sequences flanking either side of the stop codon, avoiding repeat regions, and leaving enough space for the design of reliable screening primers outside the homology region. To decrease the chance of disrupting the transcribed sequence, homology arms were designed to include whole annotated features, such as exons or 3'UTRs, whenever possible. If no 3'UTR was annotated, conserved regions were identified using the UCSC genome browser, and included in the 3' homology arm. This is advantageous to minimize the extent of detrimental mutations on the

locus in case homology-directed repair does not happen. To protect donor integrity and prevent re-cutting after homologous repair, sgRNA sites were mutated in the donor construct by mutagenesis PCR (using primers in **table 15**). At this stage, care was also taken to remove any restriction sites that could interfere with downstream cloning. As much as possible, silent mutations were inserted in coding sequences (to avoid possible regulatory regions), while preserving GC content in the locus. For this purpose, two sets of primers were designed, one with the wild type sequences, and one with the mutated sequences (labeled “mut” in **table 15**). In case the mutagenesis PCR failed, wildtype primers were used to amplify the sequence instead, and the resulting amplicon was used as a template for PCR with the mutated primers.

**Table 15:** Primer sequences used for cloning and mutagenesis of homology arms in donor plasmids

Gene	Primer name	Sequence 5'-3'
venus	GFP/Venus_F_mut	GGCGAGGGGGACGCGACGTACGGCAAGCTGACCCT
	GFP/Venus_R_mut	CGTCGCGTCCCCCTCGCCCTCGCCGGACACGCTGA
	Linker-Venus_F_BamHI	GCCGGATCCGGCAGCGCCGGCAGCGCCGCCGGCA
	Linker-Venus_R_KpnI	GCCGGTACCTCAAAGCTTGTACAGCTCGTCCATG
	LinkerVenus_F	CCGGGATCAGAATCAAGTGT
	LinkerVenus_R	TAGGAACTTCGGTACCACGC
her7 5'HF	her7_5H_F_BamHI	GCCGGATCCCTCAGGTGGAGAAGCGTCGCAGGGAG
	her7_5H_R_wt	GGGCCAGGGCCTCCACAGAGTCTGG
	her7_5Hmut_R_KpnI	GCCGGTACCGGGCCACGGTCGCCATAAAGTCTGGCTGAG
her7 3'HF	her7_3H_F_BamHI	GCCGGATCCTGACCCGGTCACCAACCAGCCG
	her7_3H_R1_KpnI	GCCGGTACCGAATCCGTGCCGATGGAATAACTGCTAC
ctnnb1 5'HF	ctnnb1_5H_F_BamHI	GCCGGATCCGACTTGGGTTTGGACATCGGGCGCACAGGGCGAG

	ctnnb1_5H_R_wt	CAGGTCGGTATCAAACCAGGCCAGTTGGTTTGAATCCCC
	ctnnb1_5Hmut_R_KpnI	GCCGGTACCCAGGTCGGTATCAAACCACGCGAGTTGGTTGCTGTGCGCC
ctnnb1 3'HF	ctnnb1_3H_F_BamHI	GCCGGATCCTAAATACCGAGATAAACATTACTACTACAC
	ctnnb1_3H_R_KpnI	GCCGGTACCCCTTATGAGTCGTTTGTGTGCAGTT
axin2.1 5'HF	axin2_1_5'HF-BamHI_F	GCCGGATCCGTGTGTTTTTAAAAATGGTGTTTTTTACACA
	axin2_1_5'HF-wt_F	GTCCATCCTCTCCACCTTGC
	axin2_1_5'HFmut-KpnI_R	GCCGGTACCGTCCATCCTCTCCACTTTTCTAACACTTCCCTCGTACAT GGCAG
axin2.1 3'HF	axin2_1_3'HF-BamHI_F	GCCGGATCCTGAAGGCAGCCGGAG
	axin2_1_3'HF-KpnI_R	GCCGGTACCAACTATCAGCAGCATAGAAGACCG
snai1a 5'HF	snai1a_5'HF_EV2_F	GCCGGTCTCAGGCTCCTCCTCAGCCCCACCATC
	snai1a_5'HF_EV2_R	GCCGGTCTCAAGGTCAGTGGAGCAGCAG
snai1a 3'HF	snai1a_3'HF_EV5_R	GCCGGTCTCACTGATTTGTGACACGCCAAGAGAGT
	snai1a_3'HFmut_EV5_F	GCCGGTCTCACTGCTGTAAGACCCACGAGTGAGGA
Donor backbone sequencing	37_pGGdest_backbone_F	TCGCGATAATGTCGGCAATCAGG
	38_pGGdest_backbone_R	TTCTCGCTCACTGACTCG
	39_pGGdest_backbone_F	GACCGATACCAGGATCTTGC
	27_pGGDest_F	GAGCGCCCAATACGCAAACCG

Donor constructs were assembled using Golden GATEway cloning [167]. This method allows modular assembly of up to 24 different sequences using a combination of Golden gate cloning and Multisite Gateway cloning (based on att recombination). For the generation of

CRISPR donor constructs in this study, only the first step of Golden GATEway cloning was used, where up to eight different sequences can be cloned into entry vectors (EVs) and assembled in a defined order based on custom compatible overhangs in one reaction step. Custom compatible overhangs are achieved by using Golden Gate entry vectors containing restriction enzyme sites for Bsal, which cuts outside of its own recognition sequence.

For cloning of homology arms into the Golden Gate entry vectors, a BamHI site (GGATCC) or KpnI (GGTACC) site were added to the forward and reverse primers respectively. To allow cutting close to the end of the DNA fragment, an additional three nucleotides (GCC) were added before each RE site. To ensure that only mutagenized sequences were used for further cloning, RE-overhangs were only added to mutated primers.

Restriction enzyme digestion of homology arms and entry vectors was done overnight with BamHI-HF and KpnI-HF (NEB, R3136S and R3142S) in a 50 ul reaction volume. Following purification and ligation of the digested EV backbone and insert, the reaction transformed by heat shock into DH5 $\alpha$  competent cells as described above. Colonies were cultured for plasmid extraction with ampicillin.

Once each part of the assembly was cloned into its respective entry vector, the integrity of the insert was verified by sequencing (GATC Biotech/Eurofins genomics). For the final golden gate reaction, components were assembled in a single tube as listed in **table 16**. Cutting of custom overhangs was achieved by using the restriction enzyme Bsal (Eco311, Thermo Scientific, ER0291).

**Table 16:** components for the golden gate reaction

<b>Component</b>	<b>Final concentration</b>
10x FD-green buffer (Thermo Scientific, B72)	1x
10x ligase buffer (NEB, B0202S)	1x
Bsal (Eco311 , Thermo Scientific, ER0291)	6 U
T4 DNA ligase (NEB, M0202S)	30 U
50 ng of each entry vector	2.5 ng/ $\mu$ l
50 ng of the destination vector	2.5 ng/ $\mu$ l
dH <sub>2</sub> O	To 20 $\mu$ l

Mutagenesis of sgRNA sites in the donors was verified by an *in vitro* Cas9 cutting assay, as described in **section 7.2.3**.

## 7.2.6 Site-directed mutagenesis

Initial testing of sgRNAs for the Ctnnb1-Venus line showed that the preferred guide did not cut at all *in vitro* or *in vivo*. Therefore, different sgRNA's were chosen, and site directed mutagenesis was carried out on the donor construct to silently mutate these sites in the homology arm. To insert additional point mutations, PCR was done using the Q5 site-directed mutagenesis kit (NEB, E0552S) and primers in **table 17**.

**Table 17:** Primers used with the site-directed mutagenesis kit to modify the *ctnnb1* donor.

Primer name	Sequence 5'-3'
70_Q5SDM_ctnnb1_5'HFw_F	CAACTCGCGTGGTTTGATACCGACCTGTAAATACCG
71_Q5SDM_ctnnb1_5'HFw_R	GTTGCTGTCGCCAGGAGGCAGGCCCTCT

## 7.2.7 Medaka single-cell injections

Single cell-injections for the generation of CRISPR lines were performed as described in Kinoshita et al. [31]. The day before injection, wildtype medaka from the Cab inbred strain (F64-F66) were separated. On the day of injection, male and female fish were put together in a ratio of two-three females per male. During this time, injection mix was prepared in RNase free conditions according to **table 18** and placed on ice.

**Table 18:** Injection mix for single cell injections of CRISPR-mediated HDR.

Component	[Final]
Cas9 RNA	150 ng/μl
Target sgRNA (1 or 2x)	15 ng/μl
sgRNA C13*	15 ng/μl
DNA donor	5 ng/μl
Nuclease-free dH2O	To 10 μl

\*Only added if circular plasmid was used as DNA donor

After 15 minutes of mating, fertilised eggs were collected and placed in ice-cold 1xERM (embryo rearing medium, see **section 7.7**), to keep them at the one-cell stage as long as possible. The eggs were separated using two pairs of blunt forceps, and lined up in a pre-chilled agarose injection plate filled with ice-cold 1xERM. Injection plates were pre-cast using a plastic mold with 1x1 mm grooves which was floated on a 100 mm petri-dish filled with 1.5% agarose/dH2O, and left to cool.

Injection needles were made from borosilicate glass capillaries (1.0 mm outer diameter x 0.58 mm inner diameter x 10 cm length, 30-0016, Harvard Apparatus) with a vertical needle puller (Sutter instruments, model p-30, settings heat 1: 800, heat 2: 600, pull: 20). Using microloader tips (Eppendorf, 5242956003) needles were backfilled with 3µl of the injection solution and mounted on a microinjection setup (MN-153, Narishige) connected to an electronic Femtojet 4x microinjector (Eppendorf, 205253000017) with access to pressured air. The needle was opened by carefully brushing the side of an embryo with the tip, taking care to keep the opening to a minimum to avoid damage when injecting. Injections were carried out with injection pressure between 600-800 hPa, and holding pressure of 10-20 hPa. Following injection, eggs were moved from the injection plate to a petri dish filled with fresh 1xERM, sorted to remove dead or badly injected eggs, and kept at 27°C.

A summary of the injected components for the generation of each line can be found in **table 19**. To increase the chance of an endogenous knock-in, two sgRNAs were injected together in some of the lines. However, this was later discontinued due to the risk of additional off-target effects.

**Table 19:** Summary of the components microinjected into medaka embryos which resulted in the final knock-in and knockout lines. \*The Cas9 variant was a gift from the Wittbrodt lab (Gutierrez and Wittbrodt, unpublished).

Line	Type	sgRNAs used in final line	Donor	Cas9 used	Homology arms (5'/3') (bp)
Her7-Venus1	Endogenous knock-in	her7_T8 + her7_T9	Plasmid donor + C13	Mammalian codon optimized Cas9 (synthesized from Addgene plasmid #43861)	647/641
Her7-Venus2	Knock-out	her7_3'HF_T12	-	XCas9 variant*	647/641
Ctnnb1-Venus	Endogenous knock-in	ctnnb1_T6	5'biotinilated long dsDNA donor	XCas9 variant*	789/1209
Axin2.1-Venus	Endogenous knock-in	axin2.1_T2 + axin2.1_T6	Plasmid donor + C13	Cas9 variant*	405/768

Snai1a-Venus	Endogenous knock-in	snai1a_T3	Plasmid donor + C13	Cas9 variant*	376/487
Her7 <sup>-/-</sup>	Knock-out	her7_KO_T1 + her7_KO_T9	-	Cas9 variant*	-

## 7.2.8 Removal of the donor backbone for the generation of the Her7-Venus2 line

In the Her7-Venus1 line, the 3'UTR sequence is repeated twice in the modified locus, one being part of the 3' homology arm, and the other being the endogenous form. Taking advantage of this, a strategy was designed using a single sgRNA that would then recognize and cleave at both positions, effectively cutting out the entire donor backbone, resulting in a single 3'UTR. The sgRNA was designed to cut outside of the area of high sequence conservation, to do minimal damage to the locus. Two sgRNA candidates, either T11 or T12 were tested. One week post-injection, a subset of embryos were sacrificed to evaluate the sgRNA efficiency. These initial results showed that T12 was more efficient than T11, with 35% and 15% of embryos positive for the backbone deletion respectively. Therefore, the T12 sgRNA was used to generate the final Her7-Venus2 line.

## 7.2.9 Her7 knockout line

To create the Her7 knockout line, the bHLH domain was identified using uniprot identifier Q1L7T8, linking out to prosite. sgRNA sites were chosen to flank either side of the bHLH domain.

## 7.2.10 Fish husbandry

Medaka were kept in a recirculating system at 27°C, with a 14:10 light/dark cycle [31]. Wildtype strains were a kind gift from the Wittbrodt lab, derived from the Cab inbred strain, incrossed to the 64th generation at the time we received them. To minimize the possibility of off-target effects, all lines were crossed out to wildtype.

Embryos were staged according to Iwamatsu [49].

## 7.3 Genotyping

To perform fin clips for DNA extraction, adult medaka were anesthetized with tricaine solution (0.4% buffered stock solution, diluted 1:20 in fish water). Once the fish was immobilized, less than 50% of the tail-length was cut off using sterilized scissors and forceps, and placed in a 1.5 ml tube containing 50 µl finclip buffer with freshly added proteinase K to a final concentration of 1 mg/ml. To keep track of individuals, finclipped fish were kept in a labelled beaker filled with recovery medium (fish water with 100 µl/L methylene blue) overnight (until genotyping results are ready). Tools were carefully cleaned with water and 70% ethanol between each fish.

Finclip samples were incubated overnight at 65°C, to dissolve the tissue and extract DNA. Following incubation, 100 µl of distilled water was added to each tube, and mixed by inverting. To heat inactivate the proteinase K, samples were incubated 10 min at 90°C, and shortly spun down before being cooled on ice. For genotyping, usually 1 µl of sample was added to each PCR reaction. Samples were kept at 4°C for long term storage, to avoid shearing of DNA.

### 7.3.1 Genotyping strategy

Screening was initially performed using PCR primers against the venus sequence only. Following the identification of venus-positive samples, PCR using a primer pair binding outside the 5' or 3' homology arm of the donor construct and inside the Venus sequence was used (hereafter referred to as the 5' integration and 3' integration PCR, respectively). The 5' integration PCR and 3' integration PCR are used to determine whether specific integration has taken place. The full locus is sequenced with primers outside the homology arms on both sides (hereafter referred to as full integration PCR). Primer sequences for each line can be found in **table 25**.

### 7.3.2 Settings for PCR genotyping

Genotyping was carried out by PCR using either the Q5 polymerase (NEB, M0491S) or the Onetaq polymerase (2x mastermix, NEB, M0482S). Reaction components and general PCR settings are listed in **table 20** and **table 21** for Q5 PCR, and in **table 22** and **table 23** for Onetaq PCR. Specific annealing temperatures and elongation times used for

different genotyping protocols are summarised in **table 24**, with primer sequences in **table 25**.

**Table 20:** Reaction components for Q5 PCR

Component	Volume per sample for 25 µl reaction (+/- GC enhancer)	Final concentration
Distilled water	26.5/36.5 µl	-
5x reaction buffer	10 µl	1x
5x GC enhancer	10 µl	1x
10 mM dNTPs	1 µl	200 µM
25 µM primer mix (Fwd+Rev)	1 µl	0.5 µM
Q5 polymerase	0.5 µl	0.02 U/µl
DNA	1 µl	-

**Table 21:** PCR settings for Q5 PCR. Annealing temperature and elongation used for each reaction are listed in **table 24**.

Step	Temperature	Time
Initial denaturation	98°C	30 seconds
30x cycles	98°C <b>50–72°C</b> 72°C	7 seconds 20 seconds <b>20-30 seconds/kb</b>
Final Extension	72°C	3 minutes
Hold	4°C	-

**Table 22:** Reaction components for Onetaq PCR

Component	Volume per sample for 20 $\mu$ l reaction	Final concentration
Distilled water	10 $\mu$ l	-
2x reaction buffer	10 $\mu$ l	1x
25 $\mu$ M primer mix (Fwd+Rev)	0.4 $\mu$ l	0.5 $\mu$ M
DNA	1 $\mu$ l	-

**Table 23:** PCR settings for Onetaq PCR. Annealing temperature and elongation used for each reaction are listed in **table 24**.

Step	Temperature	Time
Initial denaturation	94°C	45 seconds
30-35x cycles	94°C <b>45-68°C</b> 68°C	30 seconds 30 seconds 1 min/kb
Final Extension	68°C	3 minutes
Hold	4°C	-

**Table 24:** Summary of genotyping protocols used for the medaka lines used in this study

	PCR name	Polymerase	Annealing temp.	Extension time	Nr. of cycles	GC enhancer	Primers (see table 25)	Expected products
Venus only	200 bp PCR	OneTaq	51°C	15 sec	35x	-	1+2	200 bp
Her7-Venus	5'integration	Q5	71	30 sec	30X	Yes	3+4	1071 bp
	Full integration	Q5	64°C	3 min	30X	Yes	6+7	1490 bp for wt, 2267 for perfect knock-in
	Het/Hom PCR	Onetaq	57°C	1 min	30X	-	3+5+8	WT locus 267 bp 5'Venus 46 8bp Full locus with Venus 1044 bp
Ctnnb1-Venus	5'integration	Q5	69°C	1 min	30x	No	3+9	1932 bp
	Full integration	Q5	66°C	1.5 min	30x	No	10+11	3728 bp for wildtype, 4505 bp for perfect knock-in
Axin2.-Venus	5'integration	Q5	67°C	30 sec	30X	No	3+12	800 bp
	Full integration	Q5	68°C	40 sec	30X	No	13+14	1276 bp for wildtype, 2053 bp for perfect knock-in
Snai1a-Venus	5'integration	Q5	67°C	30 sec	30X	Yes	3+15	978 bp
	3'integration	Q5	69°C	30 sec	30X	No	16+19	640 bp
	Full integration	Q5	67°C	1 min	30x	No	15+16	1258 bp for wt, 2035 bp for perfect knock-in
Her7 knock-out	Deletion	Onetaq	55°C	36 sec	30x	-	17+18	WT 600 bp, deletion 311

**Table 25:** Primer list for genotyping medaka lines used in this study. Refer to table 24 for genotyping reaction details.

Primer nr.	Primer name	Sequence (5'→ 3')
1	Venus200_F1	CTACAACAGCCACAACGTCT
2	Venus200_R1	GGTCTTTGCTCAGTTTGGAC
3	CV_shortseq_Venus_R	AGAAGTCGTGCTGCTTCATGTGG
4	CV_Her7_seq_F	TAA CCC TGC TCA TGC GGA AAG G
5	CV_her7_shortseq_F	AGAAGTCCAAGGACAGGTTGCG
6	her7_seq_F	CTTAAATCTGGGCCGTGCATATTC
7	her7_seq_R	ACAGCAAAAAGTGAAACATTTGACA
8	CV_her7_het/hom_R	GCTACAGGACAGAGGTTTGAACG
9	CV_ctnnb1_seq_F	TAGCTTATGCAGCCATGTGGC
10	ctnnb1_seq_F	TATTCTGGCCAGAGATGTTCCACAA
11	ctnnb1_seq_R	CCACTAGTTGCTGAAATGCTTCAA
12	axin2_1_seq_F	TTATGAAAATGGAGGCACAGTCCT
13	axin2_seq_F	GATAAGTTTGGAGTCTGGGAACGG
14	axin2_seq_R	CTGCCTGCTGTACAAACCAAGG
15	snai1a_seq_F	AGGTCATTCTCTCATCATTGGAGC
16	snai1a_seq_R	CGAAGGTCATGGCTTCAGCA
17	Her7_Exon1_F	CAAGATCAGGATGAATCGACGAGC
18	Her7_Exon3_R	AAGGTAGCATCCAGCGCAGG
19	Venus_end_F	TCACATGGTCCTGCTGGAGTTCG

## 7.4 Working with medaka embryos

### 7.4.1 Dechorionation of medaka embryos

Dechorionation of embryos was performed using methods described in Kinoshita et al. and Porazinski et al. [31, 168].

The medaka chorion is very tough and consists of two layers that can be removed using a protease solution made from the hatching enzyme naturally produced by the embryos themselves [31]. To allow efficient penetration of the enzyme, it is first necessary to scratch the chorion surface. This can be done using a small sheet of fine waterproof sandpaper

(p2000) placed inside a petri dish. To scratch the chorion, up to 7 embryos were placed on the sandpaper, with most of the water removed, and carefully rolled for one minute, or until the villi surrounding the chorion are scratched off the surface. Rolling too many embryos at once may increase the risk of injuring them. Next, embryos were placed in 20 mg/ml pronase (Roche, 000000010165921001) in 1xERM for 30 minutes (up to 1 hour) at 27°C. To remove excess pronase which could otherwise inactivate the hatching enzyme, embryos were washed 5 times with 1X ERM or PBS. At this stage embryos can be briefly uncovered by medium.

Finally, embryos were transferred to a glass or agarose-coated plastic petri dish before the addition of hatching enzyme. This reduces the chances of embryo collapse after hatching, as they are very fragile outside the chorion. Hatching enzyme was purchased from the Medaka National BioResource Project in Japan (NBRP). As much water as possible was removed, and just enough hatching enzyme was added to cover embryos, tilting the dish to minimize the amount used (usually around 100  $\mu$ l). Embryos were incubated 15 minutes-1 hour at 27°C, depending on enzyme efficiency, which can vary significantly from batch to batch. To monitor the progress, embryos were checked periodically until the chorion was visibly dissolved. After hatching, most of the enzyme was carefully collected for re-use (avoiding that embryos make any contact with air) and 1x BSS pH 8.3 (balanced salt solution, see **section 7.7**) was added immediately. To remove the last traces of hatching enzyme, embryos were washed once in 1xBSS pH 8.3. Dechorionated embryos should only be handled with wide-mouth glass transfer pipettes to avoid embryo collapse.

## 7.4.2 Whole embryo imaging

Imaging of whole embryos was adapted from the Martines-Morales lab protocol, Porazinski et al. [168] and Rembold et al. [39]. This protocol is complicated by the fragility of embryos at the early stages of somitogenesis, they will often collapse. The best stage for whole embryo imaging is the 4-somite stage due to the way embryos balance in mounting media which requires less orientation (and therefore a lower chance of embryo collapse). Younger embryos tend to die or grow in the wrong direction, and older embryos grow too quickly out of focus.

Apart from low throughput, the main drawback of imaging whole medaka embryos is the presence of strong yolk-contractions that appear between iwamatsu stage 14/15 (mid-epiboly) and iwamatsu stage 26 (22 somites, onset of heart beating). These rhythmic contractions (approximately 1 per minute at 25°C, [39]) make time lapse imaging difficult, as

the whole embryo rotates with each contraction. To circumvent this issue, partial inhibition of gap-junctions can be achieved using 3.5 mM n-heptanol added to the imaging medium [39].

To prepare embryos for imaging, dechoriation was carried out as described above. During dechoriation, a 3.5M heptanol stock solution was prepared fresh by mixing DMSO (Merck, 10236276001) and n-heptanol (Sigma, HPLC grade, 72954-1ML-F,) at a 1:1 ratio. 3.5M stock solution was mixed well by vortexing and kept under aluminum foil to protect from light. Immediately before use, 3.5M heptanol stock solution was added 1:1000 to 1xBSS pH 8.3 for a final concentration of 3.5 mM, and vortexed thoroughly. Using buffered salt solution (between pH7.5 and 8.3) is important for consistent results. Disposal of all heptanol solutions should be with non-halogenous liquid waste.

Dechorionated embryos were washed 1-2 times with 1xBSS pH 8.3 before being placed in 1xBSS +3.5mM heptanol using a wide-mouthed glass pipette, and incubated for at least 1h at RT in the dark (under aluminum foil). Meanwhile, mounting medium was prepared. Two options can be used:

1. 0.5% low melting point agarose:  
To make stock aliquots, dissolve 1% low melting point agarose (Biozym, 840101) in 1xBSS, heat up to 70°C, and vortex many times to dissolve. Keep at 4°C in 500 µl aliquots. To use, heat a 1% agarose aliquot to 70°C until it becomes liquid, then keep at 35°C until use. Mix 500 µl 1xBSS with 7mM heptanol (dilute 3.5M stock 1:500), and warm to 35°C. Add the 1xBSS with 7mM heptanol to dissolve the 1% agarose 1:1- to achieve a final concentration of 0.5% agarose with 3.5mM heptanol. Keep at 35°C as little as possible, use immediately. (Note: heptanol evaporates above 35°C).
2. 1% methyl cellulose:  
To make a 2% methyl cellulose stock, heat 1x BSS pH 8.3 to 80°C, add methyl cellulose, and stir at 4°C until dissolved. Keep at room temperature. Measure desired amount of methyl cellulose in an eppendorf by weight (pipetting is difficult). Dissolve 2% methyl cellulose 1:1 with 1xBSS with 7mM heptanol to get a final concentration of 1% methyl cellulose with 3.5mM heptanol. Vortex sideways to properly mix the two solutions. Spin down to remove bubbles.

Using glass pipette, dechorionated embryos were carefully transferred to an eppendorf containing agarose or methyl cellulose. From here embryos were pipetted into 8-well glass bottom dishes (Nunc, Lab-Tek, 155411) filling each well to about 1/4 of the volume agarose or methyl cellulose. This makes it easier to orient the embryos under the stereomicroscope using a pipette tip or hair tool. No more than one embryo was added per well, in case of

embryo collapse which destabilizes the agarose layer and increase the chance of collapse for other embryos in the same well. When filling each well with agarose, care was taken to cover the bottom of the well completely to prevent agarose from detaching and sliding away during imaging (0.5% agarose is not very solid).

When using 1% methyl cellulose, embryos were imaged immediately. When using 0.5% agarose, embryos were left for 5-10 minutes to allow the agarose to solidify, before bringing the plate to the microscope. Straight before imaging, 1xBSS + 3.5mM heptanol was added over the agarose layer to prevent it from drying out. Waiting until the embryos are mounted on the microscope to add the final layer of 1xBSS minimizes the chance of the agarose layer detaching.

### 7.4.3 Culture of medaka PSM explants

To culture PSM explants, embryos were grown to Iwamastu stage 23 (12 somites), and the tough outer chorion was removed using fine sandpaper followed by treatment with pronase and hatching enzyme. Once dechorionated, the tail was dissected by cutting between 2-5 somites away from the unsegmented PSM. Initial cultures of PSM explants were carried out in L15 (Leibovitz) medium, a CO<sub>2</sub>-independent minimal medium supplemented with 20% FCS. While these conditions were sufficient for medaka PSM explants to grow and segment in culture, the high serum concentration required was a concern for reproducible culture conditions, in addition to giving high background fluorescence during imaging. Therefore, Gibco CO<sub>2</sub>-independent medium was used to culture medaka PSM explants in serum-free conditions. Live imaging with a 5-10 minute time resolution of growing, segmenting PSM explants in CO<sub>2</sub>-independent medium can be carried out overnight on a confocal microscope. Using this method, Her7-Venus explants can be imaged for up to 16 hours.

Dissection and culture of medaka PSM explants first requires the removal of the chorion as described above. To better access the PSM, dissection was performed around stage 23 (12-14 somite stage), and dechorionation should therefore start latest at around stage 22 (10 somite stage). Culture medium was prepared using either serum-supplemented or serum-free conditions according to **table 26** and filtered with a 0.22  $\mu$ m filter.

**Table 26:** Components of culture medium for medaka PSM explants

Components	Serum-supplemented	Serum-free
Base media	Leibovitz L15 medium without phenol red (Gibco, 21083027)	CO <sub>2</sub> -independent medium with phenol red* (Gibco, 18045054)
Glucose (45% solution in water, G8769, Sigma)	2mM	2mM
Penicillin-Streptomycin (P4333, Sigma)	1%	1%
BSA (BAC62, Equitech-Bio)	0.1% BSA	0.1% BSA
L-Glutamine (Gibco, 25030 )	-	2mM
Serum (Millipore, ES009-B)	20% FCS	-

\*Medium without phenol red is not commercially available

For dissection, dechorionated embryos were transferred with a glass pipette to a 10 cm plastic petri-dish filled with culture medium (in the case where serum-supplemented media was used for culture, dissection was carried out in culture medium without serum). To make sure embryos were at the right stage for dissection (stage 23-24, 12-14 somites), the appearance of the “body cavity”, a hollow area on the yolk on either side of the head, was used as a landmark. To access the PSM, embryos were first deflated and laid flat by puncturing the yolk. As much as possible of the tissue around the PSM was dissected away, and using forceps to steady the tail on one side, a cut was made with the scalpel about 3-5 somites above the PSM. The dissected PSM was then washed by transferring it to a second 3.5 cm dish filled with culture medium using a P20 filter tip. Finally, tails were placed in a glass bottom 96-well plate filled with 100 µl culture medium per well. Bubbles were removed, and the dish was briefly tilted to encourage tails to drift to the center of the well right before imaging. Tails were placed in straight lines on two rows only to minimize stage movement during imaging.

#### 7.4.4 Temperature perturbation experiments

All temperature perturbation experiments were carried out using embryos from the same cross of a heterozygous F1 from the Her7-Venus2 line (stock number 5147) to wildtype Cab F67 (stock number 5105). Tail explant culture was performed from the 12-somite stage as described above, in serum-free CO<sub>2</sub>-independent medium.

Before start of imaging, tail explants were incubated for at least 30 minutes in the pre-heated microscope incubation chamber to allow equilibration to the correct temperature.

Imaging settings are given in **table 27**. To increase the throughput of these experiments, the time resolution of these experiments was mostly set to 10 minutes.

**Table 27:** Settings for confocal imaging of Her7-Venus2 tail explants

Imaging medium	CO <sub>2</sub> -independent medium (serum-free, see table 26)
Temporal resolution	5 or 10 minutes
Dimensions	512x512 pixels, 16 bit depth (x=707.11um y=707.11um)
Z-stack	3 or 5 confocal stacks, 7 um spacing (z=14 or 28 um)
Laser power	6.5% 514 nm
Objective	Plan-achromat 20x/0.8, zoom 0.6
Pixel dwell	2.55 μs
Averaging	Line, 8x
Gain (514/TL)	1130/276
Pinhole	354 um

## 7.4.5 Skeletal staining

Skeletal staining was adapted from Sakata-Haga et al. [169]. Embryos were grown at 27C until 15 dpf, and anesthetized on ice and immersed in fixative solution (5% formalin (Merck, 1004960700), 5% Triton X-100 (Merck, T8787), 1% potassium hydroxide (KOH) (Merck, 1050330500). Fixation was carried out at RT for 48-72 hours, followed by a wash in dH<sub>2</sub>O. Subsequently, staining solution (0.05% alizarin red S (Sigma A5533), 20% ethylene glycol (Sigma 324558-100ML), 1% KOH;) was added to each sample and incubated 2x15 min at RT on a rolling shaker, cover in foil. Clearing of stained samples was carried out in 20% Tween 20/1% KOH for 1h at RT on a rolling shaker. Finally, clearing solution was replaced with fresh 20% Tween 20, 1% KOH and incubated with shaking overnight at RT. Hatchlings were preserved by going through a graded glycerol series, from 50 to 75 to 100% glycerol in water for 15 minutes each, protected from the light. For imaging, hatchlings were transferred to a dish filled with 100% glycerol for imaging.

## 7.5 Molecular biology

### 7.5.1 General cloning

Unless otherwise specified, cloning was carried out as described below. Primers used for cloning and mutagenesis of homology arms, cloning of ISH probe templates, cloning of gRNAs, HCR probes and genotyping were ordered from Sigma aldrich (scale: 0.025  $\mu$ mole, desalt, dissolved in dH<sub>2</sub>O to 100  $\mu$ M). Amplification of homology arms and ISH probe templates was done using PCR with the Q5 polymerase (NEB, M0491S). Depending on the application, reactions were either separated on a 1-2% agarose/TAE gel (agarose Sigma, A9539) followed by gel extraction with the MinElute gel extraction kit (Qiagen, 28604), or purified using the QIAquick PCR purification kit (Qiagen, 28104).

For subcloning, purified amplicons were a-tailed with taq polymerase (NEB, M0273S) and ligated into the pCRII-TOPO vector using the TOPO-TA cloning kit (ThermoFisher, 450640).

For restriction enzyme digestion, up to 10  $\mu$ g of DNA was mixed with 1  $\mu$ l of restriction enzyme (NEB) with its corresponding buffer in a 50  $\mu$ l reaction volume. The reaction was stopped by adding purple loading dye (6x with EDTA, NEB, B7024S) and purified using the PCR purification kit or separated and extracted on an agarose gel, as described above. Ligation of digested fragments was performed using 40 ng of the vector backbone, with a 3:1 molar ratio of insert:vector and T4 ligase (NEB, M0202S) with fresh 10x ligase buffer (NEB, B0202S, kept in aliquots at -20 °C and thawed at RT to avoid degradation of ATP in the buffer) in a 20  $\mu$ l reaction at 16 °C overnight. After ligation, the reaction was heat inactivated at 65 °C for 10 minutes, and cooled on ice before transformation.

For plasmid amplification of TOPO-plasmids, entry vectors (EV) and donor constructs, DH5 $\alpha$  competent cells (propagated in-house) were transformed by heat shock and cultured on LB-agar plates with selectable markers (100  $\mu$ g/ml ampicillin or 30  $\mu$ g/ml kanamycin) and 35  $\mu$ l X-Gal (20 mg/ml, ThermoFisher R0941) at 37°C. Single colonies were selected and cultured in 5 ml LB-medium supplemented with ampicillin (final concentration 100  $\mu$ g/ml) or kanamycin (final concentration 50  $\mu$ g/ml). To isolate plasmid material, the QIAprep spin Miniprep kit was used (Qiagen, 27106). Sequencing of purified plasmids was carried out using GATC Biotech/Eurofins genomics to verify sequence integrity.

For cDNA production, total RNA from the desired embryonic stage was extracted using the RNeasy mini kit (Qiagen, 74104), followed by reverse transcription using the SuperScriptIII First-Strand Synthesis System (ThermoFisher, 18080-051).

## 7.5.2 Dehydration of medaka embryos for colorimetric *in situ* hybridisation (ISH) or *in situ* hybridisation chain reaction (HCR)

Dehydration was performed according to protocols from the Wittbrodt lab and D. Liedtke. Synchronized wild type medaka embryos were collected and grown to 7-9 somite stage at 27°C. When the desired stage was reached, embryos were fixed in 4% paraformaldehyde (EMS, 15710) diluted in 2x PBS pH 7.5 for 4 h at RT, or overnight at 4°C (up to 3 nights) with rotation. Fixation in paraformaldehyde preserves morphology better than formaldehyde. To remove the chorion, up to 15 fixed embryos were moved to a dish containing 1xPBST see **section 7.7**). This causes the embryos to (temporarily) shrink slightly due to the osmotic difference, so that dechorionation is easier. Using fine sharp forceps (biology nr. 5), the chorion was carefully removed. This is only possible in fixed embryos, when the chorion is brittle. To remove residual fixation solution, embryos were washed 4x5 minutes in PBST, before dehydration in a gradual series of 25%, 50%, 75% and 100% methanol in PBST (5 minutes per wash). Finally, the last methanol wash was replaced with fresh 100% methanol and kept at -20°C for at least one night. Embryos can be stored in tubes at -20°C for a few months, longer incubation may improve probe penetration for weakly staining probes.

## 7.5.3 *In situ* hybridisation (colorimetric)

Colorimetric *in situ* hybridisation was performed based on Winkler lab protocol, D. Liedtke protocol, EMBO workshop manual “Molecular and Genetic Tools for the Analysis of Medaka and Zebrafish Development” (2002), and Aulehla lab protocol. Either one probe with Digoxigenin-UTP labeling, or two probes with Digoxigenin-UTP and Fluoresceine-UTP labeling was used. In the case of two-color hybridisation, detection was performed in two consecutive rounds using Fast Red (for fluorescein-labeled probes) and NBT/BCIP (for DIG-labeled probes). The probe for the gene with the strongest expression was always labeled with Fluoresceine-UTP, as this is a weaker substrate.

**Table 28:** List of primers used for cloning of ISH probes.

Gene	Primer name	Sequence (5'→ 3')	Source	Note
------	-------------	-------------------	--------	------

Venus	324_Venus_cf1	CAAGCTGACCCTGAAGCTGAT	Aulehla lab	Amplified using her7 donor, with modified Venus sequence
	327_Venus_cr2	TAGCTCAGGTAGTGGTTGTC	Aulehla lab	-
her7	her7_ISH_F	TGCAAGATCAGGATGAATCG	Elmasri et al. [57]	Gift from Winkler lab
	her7_ISH_R	GTCTTTGCTCGCTGCTCTCT	Elmasri et al.[57]	Gift from Winkler lab
her1/11	49_her1/11_ISH_F	ATTCTGAAGCCCGTTGTGGA	Elmasri et al.[57]	-
	50_her1/11_ISH_R	AGAACCAGGGTCGCCACATG	Elmasri et al.[57]	-
her5	51_her5_ISH_F	ATGTCCAAACCGCTGATGGAGA	Elmasri et al.[57]	-
	52_her5_ISH_R	CATCCTTATGTTAGAGTCACTGCG	Elmasri et al.[57]	-
myf5	myf5_ISH_F	CTTCCAAGGTGGAGATCCT	Elmasri et al.[57]	Gift from Winkler lab
	myf5_ISH_R	GCGTCAGTGGGTATAACAGC	Elmasri et al.[57]	Gift from Winkler lab
lfng	lfng_ISH_F	GGACAGGACACCGTATGGAC	Elmasri et al.[57]	Gift from Winkler lab
	lfng_ISH_R	GTCGTATTCAACGCCATCT	Elmasri et al.[57]	Gift from Winkler lab
mesp-a	mesp_ISH_F	GCCATGGAGATGTCTTCTG	Elmasri et al.[57]	Gift from Winkler lab
	mesp_ISH_R	GCTCTCTGCTGACCTTGAG	Elmasri et al.[57]	Gift from Winkler lab
snai1a	89_snai1a_ISH_F	TACCTGCCCCACCTCTGAATC	Liedtke et al. [144]	-
	90_snai1a_ISH_R	CTTCACCTCTGCATGGGTCT	Liedtke et al. [144]	-
ctnb1	ctnb1_ISH_F	GTTCAAGACATCGATGGTCAGTATGC	-	-
	ctnb1_ISH_R	AGAATAATCAGCTTGCTCTCCTGG	-	-
Axin2.1	axin2.1_ISH_F	GATTGCAGCACTTTGTCCAGG	-	Gift from Wittbrodt lab

	axin2.1_ISH_R	ACTAGTGATTAGGACCTTGCCC	-	Gift from Wittbrodt lab
Axin2.2	axin2.2_ISH_F	GATTGTGCTCCAGCAGTGG	-	Gift from Wittbrodt lab
	axin2.2_ISH_R	TCCAGGATCTTGCCCTCGTACG	-	Gift from Wittbrodt lab

To make RNA probes, primers were designed to amplify around 500 bp of the coding sequence for each target (primers listed in **table 28**). Amplicons were subcloned into the pCRII-TOPO vector. The integrity of the sequence and insert orientation was verified by sequencing with M13 forward and reverse primers (GATC Biotech/Eurofins genomics).

In preparation for probe synthesis, 10 µg of plasmid template was linearised overnight and purified as described in **section 7.5.1**. *In vitro* transcription of probes was performed with the Riboprobe Combination System (Promega, P1460). Labeling of probes was achieved using 10x DIG RNA labeling mix (Roche, 11277073910) or 10x fluorescein RNA labeling mix (Roche, 11685619910).

After *in vitro* transcription and DNase treatment, probes were purified using the RNeasy mini kit (Qiagen, 74104, as described on page 54 of the kit manual, with elution in 2x25 µl of TE buffer pH 8.0). Concentration of transcribed probes was measured to be between 120-190 ng/µl. Transcribed probes were mixed 1:1 with hybridisation buffer (see **section 7.7**) and stored at -20°C until use.

On the first day of ISH, dehydrated embryos were transferred to a 12-well dish (3 ml volume per well), and re-hydrated using a gradual series of 75%, 50%, 25% methanol in PBST (5 minutes per wash) followed by a 2x5 minute wash in PBST. Next, digestion in proteinase-K solution (10 µg/ml in PBST) was carried out without shaking according to the stage of the embryos, as listed in **table 29**.

**Table 29:** Overview of time required for proteinase-K digestion (from EMBO workshop manual “Molecular and Genetic Tools for the Analysis of Medaka and Zebrafish Development”, 2002). See Iwamatsu [49] for staging.

Iwamastu Stage*	Time of pro-k digestion
1 - 13	1 - 2 min
14 - 16	3 - 4 min
17 - 20	5 min
21 - 24	7 min
25 - 30	10 - 15 min
> 30	> 15 min

To stop the proteinase-K reaction, embryos were quickly rinsed in freshly prepared 2 mg/ml glycine/PBST (Merck, 1042011000) and then washed 2x5 minutes in PBST. Post-fixation was done in 4% formaldehyde, 0.05% glutaraldehyde/PBST for 30 min (Merck 1060092511), before another 2x5 minute wash in PBST.

For the hybridisation reaction, embryos were incubated in hybridisation buffer for 15 minutes at room temperature, and then moved to eppendorf tubes with fresh hybridisation solution for 1 hour at 68°C. During incubation, RNA probes were thawed to 37°C, and 3-8 µl of each probe was added to 300 µl fresh hybridization buffer. Before adding probe solution to the samples, they were denatured for 10 min at 80°C. The hybridisation reaction was performed overnight (at least 16 hours) at 68°C. Post-hybridisation washes were performed using netwells, and are summarised in **table 30**.

**Table 30:** Overview of post-hybridisation washes for ISH

Solution	Time	Temperature
Hybridization solution	30 min	68°C
Solution I	2 x 30 min	68°C
Solution III	2 x 30 min	68°C
Solution III	2 x 60 min	68°C
TBST	3 x 15 min	T F
Blocking solution (10% sheep serum / TBST)	2 hours	T F

Antibody solution (1:2000 in 1% sheep serum/TBST)

Overnight

4°C

Antibodies were pre-absorbed with mouse embryo powder for at least 1 hour before use.

If double staining was desired, anti-fluorescein antibodies (Roche, 11426338910) were added first. After antibody incubation, embryos were equilibrated for 2 x 5 min in 0.1 M TrisCl, pH 8.2/0.1% Tween20. Staining was done using Fast Red tablets (Sigma-Aldrich, F4523) dissolved in 0.1 M TrisCl, pH 8.2, 0.1% Tween 20 and sterile filtered (0.2 µm) to remove particles. Staining solution was added to embryos which were incubated in the dark without shaking for up to 48 hrs, replacing the staining solution several times. Because the fastred stain is weak, usually staining overnight should be sufficient.

Before the addition of the anti-DIG antibody, embryos were washed 3 x 5 min in TBST, followed by incubation on a shaker at RT for 2 x 10 min in 0.1 M glycine/HCl, pH 2.2/0.1% Tween to remove the anti-fluorescein antibody. Lastly, embryos were again washed 4 x 5 min in TBST, or overnight at 4°C. For DIG staining, embryos were equilibrated 3 x 15 min in NTMT (see **section 7.7**) and then stained in 170 µg/ml BCIP, 340 µg/ml NBT/ NTMT. After completed staining, samples were washed several times in TBST, followed by PBST, before fixation in 4% formaldehyde/ PBST.

#### 7.5.4 *In situ* hybridisation chain reaction (HCR)

Three-color *in situ* hybridization chain reaction (HCR) was performed after Choi et al. [150]. In this method, 5 pairs of DNA probes are designed to recognize adjacent sequences on the target mRNA. In addition to the target sequence, these probes are extended with one half of a split initiator sequence. Only when both DNA probes correctly hybridise to their mRNA target, the whole initiator sequence is aligned and can trigger the hybridisation reaction. The hybridisation reaction is mediated by pairs of fluorophore-labeled metastable hairpins (H1 and H2) which contain amplifier sequences that recognize the initiator sequence on the probes. When a whole initiator is recognized by the hairpin amplifier sequence a self-assembly reaction is triggered, resulting in amplification of the fluorescent signal. In this study, up to three mRNA targets were used, requiring three different groups of H1 and H2 hairpins. Each of these groups has a different amplifier sequence and is labeled with a different fluorophore, as summarized in **table 31**. Probe hybridisation buffer, amplification buffer, wash buffer and H1/H2 hairpin solutions were ordered from Molecular Instruments.

**Table 31:** Overview of hairpins used in this study

Amplifier sequence	Fluorophore
B5	Alexa488
B2	Alexa546
B4	Alexa647

Embryos were dehydrated as described above, and kept in 100% methanol at -20°C until use.

HCR probes were designed in five pairs. Each pair consists of an “odd” and “even” probe, each 25 bp, separated by 2 bp between them. Probe design was facilitated by an R script kindly provided by the Steventon lab (Cambridge University). To ensure specificity, probes were blasted against the medaka HdrR genome using ENSEMBL. Oligos (listed in **table 32**) were ordered from Sigma aldrich (scale: 0.025  $\mu$ mole, desalt, dissolved in dH2O to 100  $\mu$ M). For each gene, 2  $\mu$ l of each odd probe were mixed in equal volumes to obtain a 20  $\mu$ M stock. The same was done for the even probes. The 20  $\mu$ M stock was diluted a further 10x (1 part oligos, 9 parts dH2O) to get a 2  $\mu$ M working solution, divided in 10  $\mu$ l aliquots kept at -20°C.

**Table 32:** List of oligos used as HCR probes

Oligo name	Sequence 5'-3'
myf5_B5_Odd_1	ctcactccaatctctataaCCGGTGAGCTCTAGGCTGGAGCCGA
myf5_B5_Even_1	ACCCTGACGTGCTCGTCCTCCTCAGaactaccctacaaatccaat
myf5_B5_Odd_2	ctcactccaatctctataaCTGCAGGCTTTCGATGTACTGGATG
myf5_B5_Even_2	GTTCTCCACCTGCTCCCGCAGCAGCaactaccctacaaatccaat
myf5_B5_Odd_3	ctcactccaatctctataaGGCGGTCAACAATGCTCGACAGGCA

myf5_B5_Even_3	GTCCACCGCTGGACTCCACGGAGGAaactaccctacaaatccaat
myf5_B5_Odd_4	ctcactcccaatctctataaCCAGAGTTCTCAGGAGTGCAGGGCT
myf5_B5_Even_4	CACAGGACGTGGTAGACGGGTCTGgaactaccctacaaatccaat
myf5_B5_Odd_5	ctcactcccaatctctataaGTCGTTCTCACGCAGAATAAGTTCT
myf5_B5_Even_5	TATTGAAGGTTGCCGCACATCCGGCaactaccctacaaatccaat
mespaa_B4_Odd_1	cctcaacctactccaacaaCATGGCGGCTGAAGCTGCAGAGGTC
mespaa_B4_Even_1	CTGAAGGGGAAGCAGAAGGACATCattctcaccatattcgcttc
mespaa_B4_Odd_2	cctcaacctactccaacaaGTGAGATGAAGCTCTGCTGGGCTGC
mespaa_B4_Even_2	AAGCTGGAAGGTGGCCCAGTCTGGCattctcaccatattcgcttc
mespaa_B4_Odd_3	cctcaacctactccaacaaGTTCTGAGGTGATGAAGAGCTTTGG
mespaa_B4_Even_3	GCAGGAGCGACGGATGGAGGCAGGTattctcaccatattcgcttc
mespaa_B4_Odd_4	cctcaacctactccaacaaTGCTCGTTCACGGTGCTGCAGCTCG
mespaa_B4_Even_4	TGGCTGGATTGCTGTGGCGAGGAGCattctcaccatattcgcttc
mespaa_B4_Odd_5	cctcaacctactccaacaaTTCAACTGTCCTGAGAAGATCAC
mespaa_B4_Even_5	G TTCAGAGCAGATGTGGGAGGACAGattctcaccatattcgcttc
msgn1_B2_Even1	cctcgtaaactcctcatcaaaCACTCAGACAGGATTTTCAGCTTCCA
msgn1_B2_Odd1	TCTCCAGAGGGGCTCAGCAGGCATTaaatcatccagtaaaccgcc
msgn1_B2_Even2	cctcgtaaactcctcatcaaaCTCGGGTGAGGAGCACGTGGAATCC
msgn1_B2_Odd2	GTCCCGACGCCTGTTAGGATAGCTCaatcatccagtaaaccgcc

msgn1_B2_Even3	cctcgtaaatcctcatcaaaTTGAAGCCACTTCGCGCTCCGAGAA
msgn1_B2_Odd3	TTTTGGACTTGCTTGATCTTTGCGCaaatcatccagtaaaccgcc
msgn1_B2_Even4	cctcgtaaatcctcatcaaaATCTTCTCCCTCTCACTGGCCTTCA
msgn1_B2_Odd4	AGAGCCTCTGCCAGACTTCTCATCCaaatcatccagtaaaccgcc
msgn1_B2_Even5	cctcgtaaatcctcatcaaaCTGGTTGTAATCCGGTGGAAAGGTAG
msgn1_B2_Odd5	CTGGATCTTGGTCAGGGGCTGGCCTaaatcatccagtaaaccgcc

On the first day of HCR, samples were rehydrated with a series of 75%, 50%, 25% methanol/PBST solutions for 5 minutes each. Finally, embryos were washed 3 x 10 minutes with PBST. To start detection, embryos were pre-hybridised in 500 µl pre-heated probe hybridization buffer for 30 min at 37°C. Meanwhile, probe solution was prepared by the addition of 4 pmol of each probe mixture (2 µl of 2 µM stock) to 500 µl of probe hybridization buffer at 37°C. Pre-hybridisation buffer was replaced with the probe solution, and incubated for 20 hours in a 37°C water bath (to avoid condensation on the lid). As hybridisation solution is quite viscous, replacing the solution is best done by pipetting up and down to make embryos float up, before removing as much liquid as possible.

Excess probe solution was washed away 4 x 15 min using 500 µl of pre-heated probe wash buffer at 37°C, followed by 2 x 5 minute washes with 5x SSCT (see solutions in **section 7.7**) at RT. To start probe amplification, samples were incubated in 500 µl of pre-warmed amplification buffer for 30 min at RT. Meanwhile, 15 pmol (5 µl of 3 µM stock) of each hairpin solution (H1 and H2) was heated to 95°C for 90 seconds, before allowing it to cool at RT in the dark for 30 minutes (hairpins are light sensitive). Cooled H1 and H2 hairpins were added to 500 µl of pre-warmed amplification buffer. Finally, amplification solution was replaced with the hairpin solution, and incubated for 16 hours in the dark at RT.

Excess hairpin solution was removed by washing with 500 µl 5x SSCT at RT for 2x 5min, 2 x 30 min and 1 x 5 min. To label nuclei, 5 µl DAPI 5 mg/ml in DMSO was added to a final concentration of 50 µg/ml. Samples were incubated in DAPI solution for at least one night to ensure proper penetration of the dye.

Before imaging, samples were washed 1x in 5x SSCT, and incubated in 50% glycerol/5xSSCT (Glycerol 100%, 1370282500, Merck) for about 45 minutes, or until embryos had sunk down to the bottom of the tube. From here, embryos were moved to 85% (1040912500, Merck) glycerol, and moved to individual wells of a glass bottom 96 well plate. Embryos soaked in glycerol are easier to orient and sink to the bottom of the well. Imaging of stained samples was carried out in a LSM780 confocal microscope.

## 7.6 Data analysis

### 7.6.1 Image analysis

Confocal imaging datasets were blurred using a gaussian filter ( $\sigma = 4$ ) in FIJI, followed by image registration with the multistackreg plugin (Brad Busse, v1.45, available from <http://bradbusse.net/sciencedownloads.html>). For extraction of raw signal from imaging of Her7-Venus in the posterior tailbud, a 30 pixel wide moving ROI was defined and used as an input for the wavelet analysis (see below). For kymograph generation, the FIJI “Reslice” function was used by drawing a segmented line along the PSM in the direction of wave propagation.

For period gradient analysis, brightfield movies were used to determine when a somite had just formed, and a 20 pixel wide segmented line was manually drawn along the PSM for two consecutively forming somites. This line was used as a ROI to extract period data from period movies generated by the wavelet analysis (see below). For phase gradient analysis, the same ROI was used as for the period gradient extraction, but with with 1 pixel width, as phase information should not be blurred in the space dimension. Extracted phase profiles were unwrapped using the `numpy.unwrap` function. Phase and period profiles were normalized to PSM length.

### 7.6.2 Wavelet analysis

Wavelet analysis (TFAPy) was developed by Gregor Mönke (<https://git.embl.de/moenke/TFAPy>). This tool first detrends the data to remove low frequency trends from the raw signal. The detrended signal is then subjected to a time-resolved frequency analysis by cross-correlating the signal at every time-point to a set of wavelets, which are functions with a defined frequency. This generates a spectrum where for each

timepoint, the wavelets which correlate well with the signal are given a high “power” score. The power is defined as how much more likely this signal is to achieve a high correlation relative to white noise. The maximum power, periods to scan for and the cut off period for the detrending is specified by the user. To extract the period values, the maximum power ridge in the spectrum is detected. The parameters for the wavelet analysis at each temperature are outlined in **table 33**.

**Table 33:** Parameters used for wavelet analysis between 23-37°C

	Initial scan	23°C	27°C	35°C	37°C
Time resolution	10 min or 5 min	10 min	10 min	10 min or 5 min	10 min
Period range to scan for	20-200 min	80-180 min	50-150 min	20-120 min	20-120 min
Nr. periods to scan for	600	600	600	600	600
Cut off period	200 min	180 min	150 min	120 min	120 min
Max power	15	15	15	15	15

### 7.6.3 Statistics

Statistical testing was done using Graphpad Prism software. For comparison of two means, the T-test was used assuming normal distribution, whereas for multiple comparisons, the One-way ANOVA was used. Welch corrections were applied when variance could not be assumed to be equal. p-values > 0.05 were considered non-significant.

## 7.7 Solutions

### **Tricaine solution 0.4%**

400 mg Tricaine methanesulfonate; MS222 (Sigma #E10521)

97.9 ml dH<sub>2</sub>O

2.1 ml 1M Tris HCl pH 9

Adjust to pH 7

Autoclave

Aliquot and store at -20

### **Fin clip buffer (PCR grade reagents!)**

100 ml 2M Tris pH 8.0

5 ml 0.5M EDTA pH 8.0  
15 ml 5M NaCl  
2.5 ml 20% SDS  
H<sub>2</sub>O to 500 ml, sterile filter

Add 50 µl proteinase K (20 mg/ml, frozen stock in dH<sub>2</sub>O) fresh to 1 ml fin clip buffer before use.

### **Embryo rearing medium (ERM)**

Salt solution for raising embryos. Taken from Kinoshita et al. [31].

Prepare a 100x stock with:

100g NaCl  
3 g KCl  
4 g CaCl<sub>2</sub> · 2H<sub>2</sub>O  
16 g MgSO<sub>4</sub> · 7H<sub>2</sub>O

Adjust to 1L with distilled water

Dilute to 1x before use, add 17 ml HEPES pH 7.3-7.5 (adjusted with NaOH).

### **Balanced salt solution (BSS)**

Salt solution for use with dechorionated embryos. Taken from Kinoshita et al. [31]. This solution is different from ERM both in the salt concentration and the pH, and heptanol works much better under these conditions (it is important to use 1xBSS pH 8.3).

Prepare a 20X stock with:

130 g NaCl  
8 g KCl  
4 g CaCl<sub>2</sub> · 2H<sub>2</sub>O  
4 g MgSO<sub>4</sub> · 7H<sub>2</sub>O

Adjust to 1L with Milli-Q water, optionally add 2 mL of Phenol Red 0.5% (Sigma-Aldrich, P0290) and autoclave. Keep 20x stock at 4C for 1 month. Consider removing phenol red if it interferes with imaging. Dilute 20X, adjust pH to 8.3 with filtered 5% NaHCO<sub>3</sub> and sterile filter or autoclave again.

**For *in situ* hybridisation or HCR:**

100ml of Solution I for ISH:

50 ml formamide

25 ml 20x SSC, pH 5.0

5 ml 20% SDS

20 ml dH<sub>2</sub>O

100ml of Solution III for ISH:

50 ml formamide

10 ml 20x SSC, pH 5.0

100ul Tween

40ml dH<sub>2</sub>O

500ml of NTMT for ISH:

10ml 5M NaCl

50ml 1M Tris-HCl, pH 9.5

25ml 1M MgCl<sub>2</sub>

500ul Tween-20

414.5ml dH<sub>2</sub>O

TBST:

1xTBS + 0.1% Tween 20

PBST:

1x PBS (pH 7.3) + 0.1% Tween 20 (Sigma, P1379 )

5x SSCT:

Dilute from 20X Saline Sodium-Citrate (SSC) pH 5.0 to 5x SSC + 0.1% Tween 20

## 8. Appendix

### 8.1 Derivation of a relationship between frequency and $\alpha$ from the Alpha model

From the alpha model, a relationship between frequency  $\omega$  and  $\alpha$  was derived, with the constraint that the critical phase-shift to the reference oscillator is fixed at  $2\pi$  (Takehito Tomita).

The frequency  $\omega$  at time  $t$  can be represented by the following, where the frequency of the reference oscillator is  $\omega_{0R}$ , frequency at time 0 is  $\omega_0$  and the critical frequency where oscillations reach the anterior is  $\omega_c$ .

$$\omega(t) = \omega_{0R} - \varepsilon \alpha e^{\alpha t}$$

$$\omega(0) = \omega_0$$

$$\omega(t_c) = \omega_c$$

This equation can be plotted to show how the exponentially slowing oscillation frequency in a cell changes with time. From the data, we know that the phase shift to the reference oscillator should be close to  $2\pi$ , which in angular velocity is equal to 1. With this constraint, the integral of the difference between the reference oscillator and the intrinsic oscillator can therefore be taken:

$$\int_0^{t_c} (\omega_{0R} - \omega(t)) dt = 1$$

Solving for alpha provides:

$$\alpha = \omega_0 - \omega_c$$

Given that alpha is the difference between the frequency at the posterior and the frequency at the anterior, and that the period is  $\omega^{-1}$ , the difference in period ( $\Delta T$ , in minutes) will be represented by the following:

$$\Delta T = \frac{\alpha}{\omega_0(\omega_0 - \alpha)}$$

$$\Delta T = \frac{\alpha}{\omega_0^2 - \omega_0 \alpha}$$

Interestingly, the results presented here show that regardless of temperature,  $\Delta T$  is a constant ~20 minutes in all conditions except 37°C. Since the  $\omega_0 \alpha$  term is negligibly small:

$$\text{With } \Delta T \text{ constant: } \alpha \sim \frac{1}{\omega_0^2}$$

Therefore,  $\alpha$  is inversely proportional to  $\omega_0^2$ . In other words,  $\alpha$  is proportional to the period.

## 8.2 $Q_{10}$ calculation

$Q_{10}$  value was calculated using the following formula:

$$Q_{10} = \frac{R_2 \frac{10}{T_2 - T_1}}{R_1}$$

Where  $R_2$  and  $R_1$  are the rates (frequency of Her7-Venus2 oscillation in radians or somite size in  $\mu\text{m}$ ) at temperature 1 ( $T_1$ ) or temperature 2 ( $T_2$ ) in celsius.

## 8.3 Abbreviations

bHLH: basic Helix Loop Helix

Bp: Base pair

CRISPR: Clustered Regularly Interspaced Short Palindromic Repeats

CDS: Coding Sequence

Dpf: Days post fertilization

EV: golden gate Entry Vector

FGF: Fibroblast Growth Factor

GFP: Green Fluorescent Protein

HA: Homology Arm

HCR: Hybridisation Chain Reaction

HDR: Homology Directed Repair

ISH: *In-Situ* Hybridisation

NHEJ: Non-Homologous End-Joining

NICD: Notch IntraCellular Domain

sgRNA: single guide RNA

YFP: Yellow Fluorescent Protein

PAM: Protospacer Adjacent Motif

PSM: PreSomitic Mesoderm

PCR: Polymerase Chain Reaction

UTR: UnTranslated Region

RA: Retinoic acid

RE: Restriction enzyme

RT: Room Temperature

# Bibliography

1. Waddington, C.H., *Canalization of development and the inheritance of acquired characters* Nature, 1942: p. 1-3.
2. Hallgrímsson, B., et al., *The developmental-genetics of canalization*. Semin Cell Dev Biol, 2018.
3. Prudic, K.L., et al., *Developmental plasticity in sexual roles of butterfly species drives mutual sexual ornamentation*. Science, 2011. **331**(6013): p. 73-5.
4. Crain, D.A. and L.J. Guillette, Jr., *Reptiles as models of contaminant-induced endocrine disruption*. Anim Reprod Sci, 1998. **53**(1-4): p. 77-86.
5. Hattori, R.S., et al., *Temperature-dependent sex determination in Hd-rR medaka *Oryzias latipes*: gender sensitivity, thermal threshold, critical period, and DMRT1 expression profile*. Sex Dev, 2007. **1**(2): p. 138-46.
6. Twitty, V.C. and J.L. Schwind, *The growth of eyes and limbs transplanted heteroplastically between two species of *Amblystoma**. 1931. **59**(1): p. 61-86.
7. Eder, D., C. Aegerter, and K. Basler, *Forces controlling organ growth and size*. Mech Dev, 2017. **144**(Pt A): p. 53-61.
8. Mirth, C.K. and A.W. Shingleton, *Coordinating Development: How Do Animals Integrate Plastic and Robust Developmental Processes?* Frontiers in cell and developmental biology, 2019. **7**: p. 8.
9. Oliveira, M.M., A.W. Shingleton, and C.K. Mirth, *Coordination of wing and whole-body development at developmental milestones ensures robustness against environmental and physiological perturbations*. PLoS genetics, 2014. **10**(6): p. e1004408.
10. Mirth, C.K. and A.W. Shingleton, *Integrating body and organ size in *Drosophila*: recent advances and outstanding problems*. Front Endocrinol (Lausanne), 2012. **3**: p. 49.
11. Young, R.M., et al., *Compensatory growth renders *Tcf7l1a* dispensable for eye formation despite its requirement in eye field specification*. eLife, 2019. **8**: p. 12792.
12. Cooke, J., *Control of somite number during morphogenesis of a vertebrate, *Xenopus laevis**. Nature, 1975. **254**(5497): p. 196-199.
13. Ishimatsu, K., et al., *Size-reduced embryos reveal a gradient scaling-based mechanism for zebrafish somite formation*. Development (Cambridge, England), 2018. **145**(11): p. dev161257.
14. Flint, O.P. and D.A. Ede, *Facial development in the mouse; a comparison between normal and mutant (amputated) mouse embryos*. Journal of embryology and experimental morphology, 1978. **48**: p. 249-267.
15. Begasse, M.L., et al., *Temperature Dependence of Cell Division Timing Accounts for a Shift in the Thermal Limits of *C. elegans* and *C. briggsae**. Cell Rep, 2015. **10**(5): p. 647-653.
16. Thurston, G. and B. Palcic, *3T3 cell motility in the temperature range 33 degrees C to 39 degrees C*. Cell Motil Cytoskeleton, 1987. **7**(4): p. 361-7.
17. Felix, M.A. and C. Braendle, *The natural history of *Caenorhabditis elegans**. Curr Biol, 2010. **20**(22): p. R965-9.
18. Khokha, M.K., et al., *Techniques and probes for the study of *Xenopus tropicalis* development*. Dev Dyn, 2002. **225**(4): p. 499-510.
19. Kimmel, C.B., et al., *Stages of embryonic development of the zebrafish*. Dev Dyn, 1995. **203**(3): p. 253-310.
20. Kuntz, S.G. and M.B. Eisen, **Drosophila* embryogenesis scales uniformly across temperature in developmentally diverse species*. PLoS genetics, 2014. **10**(4): p. e1004293.

21. Mortzfeld, B.M., et al., *Temperature and insulin signaling regulate body size in Hydra by the Wnt and TGF-beta pathways*. Nature communications, 2019. **10**(1): p. 3257-13.
22. Yamamoto, T.-o., *Medaka (killifish) : biology and strains*. 1975, Tokyo: Keigaku Publishing Company.
23. Shostak, S., *Variation in Hydra's tentacle numbers as a function of temperature* International Journal of Invertebrate Reproduction, 1981. **3**(6): p. 321-331.
24. McDonald, J.M.C., et al., *Plasticity Through Canalization: The Contrasting Effect of Temperature on Trait Size and Growth in Drosophila*. Front Cell Dev Biol, 2018. **6**: p. 156.
25. Westerfield, M., *The zebrafish book : a guide for the laboratory use of zebrafish (Danio rerio)*. 2007.
26. Schröter, C., et al., *Dynamics of zebrafish somitogenesis*. Developmental dynamics : an official publication of the American Association of Anatomists, 2008. **237**(3): p. 545-553.
27. Chen, J., V. Nolte, and C. Schlötterer, *Temperature stress mediates decanalization and dominance of gene expression in Drosophila melanogaster*. PLoS genetics, 2015. **11**(2): p. e1004883.
28. Houchmandzadeh, B., E. Wieschaus, and S. Leibler, *Establishment of developmental precision and proportions in the early Drosophila embryo*. Nature, 2002. **415**(6873): p. 798-802.
29. Anderson, G.A., et al., *Desynchronizing Embryonic Cell Division Waves Reveals the Robustness of Xenopus laevis Development*. CellReports, 2017. **21**(1): p. 37-46.
30. Lucchetta, E.M., et al., *Dynamics of Drosophila embryonic patterning network perturbed in space and time using microfluidics*. Nature, 2005. **434**(7037): p. 1134-1138.
31. Kinoshita, M. and E. Bubenshchikova, *Medaka : biology, management, and experimental protocols*. 2009, Ames, Iowa: Wiley-Blackwell.
32. Wittbrodt, J., A. Shima, and M. Schartl, *Medaka--a model organism from the far East*. Nat Rev Genet, 2002. **3**(1): p. 53-64.
33. Furutani-Seiki, M. and J. Wittbrodt, *Medaka and zebrafish, an evolutionary twin study*. Mech Dev, 2004. **121**(7-8): p. 629-37.
34. Howe, K., et al., *The zebrafish reference genome sequence and its relationship to the human genome*. Nature, 2013. **496**(7446): p. 498-503.
35. Kasahara, M., et al., *The medaka draft genome and insights into vertebrate genome evolution*. Nature, 2007. **447**(7145): p. 714-9.
36. Spivakov, M., et al., *Genomic and Phenotypic Characterization of a Wild Medaka Population: Towards the Establishment of an Isogenic Population Genetic Resource in Fish*. G3-Genes Genomes Genetics, 2014. **4**(3): p. 433-445.
37. Gutierrez-Triana, J.A., et al., *Efficient single-copy HDR by 5' modified long dsDNA donors*. eLife, 2018. **7**: p. 142.
38. Kirchmaier, S., et al., *The Genomic and Genetic Toolbox of the Teleost Medaka (Oryzias latipes)*. Genetics, 2015. **199**(4): p. 905-918.
39. Rembold, M. and J. Wittbrodt, *In vivo time-lapse imaging in medaka--n-heptanol blocks contractile rhythmical movements*. Mech Dev, 2004. **121**(7-8): p. 965-70.
40. Hilgers, L. and J. Schwarzer, *The untapped potential of medaka and its wild relatives*. eLife, 2019. **8**: p. 554.
41. Dhillon, R.S. and M.G. Fox, *Growth-independent effects of temperature on age and size at maturity in Japanese medaka (Oryzias latipes)*. Copeia, 2004(1): p. 37-45.
42. Koger, C.S., S.J. Teh, and D.E. Hinton, *Variations of light and temperature regimes and resulting effects on reproductive parameters in medaka (Oryzias latipes)*. Biol Reprod, 1999. **61**(5): p. 1287-93.
43. Aida, T., *On the Inheritance of Color in a Fresh-Water Fish, APLOCHEILUS LATIPES Temmick and Schlegel, with Special Reference to Sex-Linked Inheritance*. Genetics, 1921. **6**(6): p. 554-73.

44. Minamitani, N. and C.A. Strussmann, *Effect of temperature on the efficiency of feminization of medaka (Oryzias latipes) by hormonal (estradiol) manipulation*. Fish Physiology and Biochemistry, 2003. **28**(1-4): p. 163-164.
45. Sato, T., et al., *Induction of female-to-male sex reversal by high temperature treatment in Medaka, Oryzias latipes*. Zoolog Sci, 2005. **22**(9): p. 985-8.
46. Gomez, C., et al., *Control of segment number in vertebrate embryos*. Nature, 2008. **454**(7202): p. 335-339.
47. Hubaud, A. and O. Pourquie, *Signalling dynamics in vertebrate segmentation*. Nat Rev Mol Cell Biol, 2014. **15**(11): p. 709-21.
48. Christ, B., R. Huang, and M. Scaal, *Amniote somite derivatives*. Developmental dynamics : an official publication of the American Association of Anatomists, 2007. **236**(9): p. 2382-2396.
49. Iwamatsu, T., *Stages of normal development in the medaka Oryzias latipes*. Mech Dev, 2004. **121**(7-8): p. 605-18.
50. Keynes, R.J. and C.D. Stern, *Segmentation in the vertebrate nervous system*. Nature, 1984. **310**(5980): p. 786-789.
51. Takahashi, Y., et al., *Mesp2 initiates somite segmentation through the Notch signalling pathway*. Nature genetics, 2000. **25**(4): p. 390-396.
52. Saga, Y. and H. Takeda, *The making of the somite: molecular events in vertebrate segmentation*. Nature reviews. Genetics, 2001. **2**(11): p. 835-845.
53. Nakajima, Y., et al., *Identification of Epha4 enhancer required for segmental expression and the regulation by Mesp2*. Development (Cambridge, England), 2006. **133**(13): p. 2517-2525.
54. Sawada, A., et al., *Zebrafish Mesp family genes, mesp-a and mesp-b are segmentally expressed in the presomitic mesoderm, and Mesp-b confers the anterior identity to the developing somites*. Development (Cambridge, England), 2000. **127**(8): p. 1691-1702.
55. Durbin, L., et al., *Anteroposterior patterning is required within segments for somite boundary formation in developing zebrafish*. Development (Cambridge, England), 2000. **127**(8): p. 1703-1713.
56. Terasaki, H., et al., *Transgenic analysis of the medaka mesp-b enhancer in somitogenesis*. Development, growth & differentiation, 2006. **48**(3): p. 153-168.
57. Elmasri, H., et al., *her7 and hey1, but not lunatic fringe show dynamic expression during somitogenesis in medaka (Oryzias latipes)*. Gene expression patterns : GEP, 2004. **4**(5): p. 553-559.
58. Cooke, J. and E.C. Zeeman, *A clock and wavefront model for control of the number of repeated structures during animal morphogenesis*. Journal of theoretical biology, 1976. **58**(2): p. 455-476.
59. Goodwin, B.C. and M.H. Cohen, *A phase-shift model for the spatial and temporal organization of developing systems*. J Theor Biol, 1969. **25**(1): p. 49-107.
60. Palmeirim, I., et al., *Avian hairy gene expression identifies a molecular clock linked to vertebrate segmentation and somitogenesis*. Cell, 1997. **91**(5): p. 639-48.
61. Aulehla, A. and R.L. Johnson, *Dynamic expression of lunatic fringe suggests a link between notch signaling and an autonomous cellular oscillator driving somite segmentation*. Dev Biol, 1999. **207**(1): p. 49-61.
62. Li, Y., et al., *Cyclic expression of esr9 gene in Xenopus presomitic mesoderm*. Differentiation; research in biological diversity, 2003. **71**(1): p. 83-89.
63. Holley, S.A., R. Geisler, and C. Nusslein-Volhard, *Control of her1 expression during zebrafish somitogenesis by a delta-dependent oscillator and an independent wavefront activity*. Genes Dev, 2000. **14**(13): p. 1678-90.
64. Oates, A.C. and R.K. Ho, *Hairy/E(spl)-related (Her) genes are central components of the segmentation oscillator and display redundancy with the Delta/Notch signaling pathway in the formation of anterior segmental boundaries in the zebrafish*. Development, 2002. **129**(12): p. 2929-46.

65. Gajewski, M., et al., *Comparative analysis of her genes during fish somitogenesis suggests a mouse/chick-like mode of oscillation in medaka*. *Dev Genes Evol*, 2006. **216**(6): p. 315-32.
66. El-Sherif, E., M. Averof, and S.J. Brown, *A segmentation clock operating in blastoderm and germband stages of Tribolium development*. *Development* (Cambridge, England), 2012. **139**(23): p. 4341-4346.
67. El-Sherif, E., et al., *Caudal regulates the spatiotemporal dynamics of pair-rule waves in Tribolium*. *PLoS genetics*, 2014. **10**(10): p. e1004677.
68. Sarrazin, A.F., A.D. Peel, and M. Averof, *A segmentation clock with two-segment periodicity in insects*. *Science (New York, N.Y.)*, 2012. **336**(6079): p. 338-341.
69. Aulehla, A., et al., *A beta-catenin gradient links the clock and wavefront systems in mouse embryo segmentation*. *Nat Cell Biol*, 2008. **10**(2): p. 186-93.
70. Delaune, E.A., et al., *Single-cell-resolution imaging of the impact of Notch signaling and mitosis on segmentation clock dynamics*. *Dev Cell*, 2012. **23**(5): p. 995-1005.
71. Harima, Y., et al., *Accelerating the Tempo of the Segmentation Clock by Reducing the Number of Introns in the Hes7 Gene*. *CellReports*, 2013. **3**(1): p. 1-7.
72. Lauschke, V.M., et al., *Scaling of embryonic patterning based on phase-gradient encoding*. *Nature*, 2013. **493**(7430): p. 101-5.
73. Matsumiya, M., et al., *ES cell-derived presomitic mesoderm-like tissues for analysis of synchronized oscillations in the segmentation clock*. *Development* (Cambridge, England), 2018. **145**(4): p. dev156836.
74. Shih, N.P., et al., *Dynamics of the slowing segmentation clock reveal alternating two-segment periodicity*. *Development*, 2015. **142**(10): p. 1785-93.
75. Soroldoni, D., et al., *A Doppler effect in embryonic pattern formation*. *Science*, 2014. **345**(6193): p. 222-225.
76. Takashima, Y., et al., *Intronic delay is essential for oscillatory expression in the segmentation clock*. *Proceedings of the National Academy of Sciences of the United States of America*, 2011. **108**(8): p. 3300-3305.
77. Tsairis, C.D. and A. Aulehla, *Self-Organization of Embryonic Genetic Oscillators into Spatiotemporal Wave Patterns*. *Cell*, 2016. **164**(4): p. 656-67.
78. Bone, R.A., et al., *Spatiotemporal oscillations of Notch1, Dll1 and NICD are coordinated across the mouse PSM*. *Development* (Cambridge, England), 2014. **141**(24): p. 4806-4816.
79. Geffers, I., et al., *Divergent functions and distinct localization of the Notch ligands DLL1 and DLL3 in vivo*. *The Journal of cell biology*, 2007. **178**(3): p. 465-476.
80. Kopan, R. and M.X.G. Ilagan, *The canonical Notch signaling pathway: unfolding the activation mechanism*. *Cell*, 2009. **137**(2): p. 216-233.
81. Kovall, R.A., et al., *The Canonical Notch Signaling Pathway: Structural and Biochemical Insights into Shape, Sugar, and Force*. *Developmental cell*, 2017. **41**(3): p. 228-241.
82. Dale, J.K., et al., *Periodic notch inhibition by lunatic fringe underlies the chick segmentation clock*. *Nature*, 2003. **421**(6920): p. 275-278.
83. Prince, V.E., et al., *Zebrafish lunatic fringe demarcates segmental boundaries*. *Mech Dev*, 2001. **105**(1-2): p. 175-80.
84. Huppert, S.S., et al., *Analysis of Notch function in presomitic mesoderm suggests a gamma-secretase-independent role for presenilins in somite differentiation*. *Developmental cell*, 2005. **8**(5): p. 677-688.
85. Jiang, Y.J., et al., *Notch signalling and the synchronization of the somite segmentation clock*. *Nature*, 2000. **408**(6811): p. 475-479.
86. Krol, A.J., et al., *Evolutionary plasticity of segmentation clock networks*. *Development* (Cambridge, England), 2011. **138**(13): p. 2783-2792.
87. Kageyama, R., T. Ohtsuka, and T. Kobayashi, *The Hes gene family: repressors and oscillators that orchestrate embryogenesis*. *Development*, 2007. **134**(7): p. 1243-1251.

88. Bessho, Y., et al., *Periodic repression by the bHLH factor Hes7 is an essential mechanism for the somite segmentation clock*. *Genes & Development*, 2003. **17**(12): p. 1451-1456.
89. Bessho, Y., et al., *Dynamic expression and essential functions of Hes7 in somite segmentation*. *Genes Dev*, 2001. **15**(20): p. 2642-7.
90. Jouve, C., et al., *Notch signalling is required for cyclic expression of the hairy-like gene HES1 in the presomitic mesoderm*. *Development*, 2000. **127**(7): p. 1421-9.
91. Dunwoodie, S.L., et al., *Axial skeletal defects caused by mutation in the spondylocostal dysplasia/pudgy gene Dll3 are associated with disruption of the segmentation clock within the presomitic mesoderm*. *Development (Cambridge, England)*, 2002. **129**(7): p. 1795-1806.
92. Ferjentsik, Z., et al., *Notch is a critical component of the mouse somitogenesis oscillator and is essential for the formation of the somites*. *PLoS genetics*, 2009. **5**(9): p. e1000662.
93. Henry, C.A., et al., *Two linked hairy/Enhancer of split-related zebrafish genes, her1 and her7, function together to refine alternating somite boundaries*. *Development*, 2002. **129**(15): p. 3693-704.
94. Sieger, D., D. Tautz, and M. Gajewski, *her11 is involved in the somitogenesis clock in zebrafish*. *Dev Genes Evol*, 2004. **214**(8): p. 393-406.
95. Trofka, A., et al., *The Her7 node modulates the network topology of the zebrafish segmentation clock via sequestration of the Hes6 hub*. *Development*, 2012. **139**(5): p. 940-7.
96. Choorapoikayil, S., et al., *Analysis of her1 and her7 mutants reveals a spatio temporal separation of the somite clock module*. *PloS one*, 2012. **7**(6): p. e39073.
97. Giudicelli, F., et al., *Setting the tempo in development: an investigation of the zebrafish somite clock mechanism*. *PLoS Biol*, 2007. **5**(6): p. e150.
98. Shankaran, S.S., et al., *Completing the set of h/E(spl) cyclic genes in zebrafish: her12 and her15 reveal novel modes of expression and contribute to the segmentation clock*. *Dev Biol*, 2007. **304**(2): p. 615-32.
99. Bessho, Y., et al., *Hes7: a bHLH-type repressor gene regulated by Notch and expressed in the presomitic mesoderm*. *Genes Cells*, 2001. **6**(2): p. 175-85.
100. Elmasri, H., et al., *Mutations affecting somite formation in the Medaka (Oryzias latipes)*. *Mech Dev*, 2004. **121**(7-8): p. 659-71.
101. Sieger, D., et al., *her1 and her13.2 are jointly required for somitic border specification along the entire axis of the fish embryo*. *Developmental biology*, 2006. **293**(1): p. 242-251.
102. Kim, W., et al., *The period of the somite segmentation clock is sensitive to Notch activity*. *Mol Biol Cell*, 2011. **22**(18): p. 3541-9.
103. Lewis, J., *Autoinhibition with transcriptional delay: a simple mechanism for the zebrafish somitogenesis oscillator*. *Current biology : CB*, 2003. **13**(16): p. 1398-1408.
104. Monk, N.A.M., *Oscillatory expression of Hes1, p53, and NF-kappaB driven by transcriptional time delays*. *Current biology : CB*, 2003. **13**(16): p. 1409-1413.
105. Kawamura, A., et al., *Zebrafish hairy/enhancer of split protein links FGF signaling to cyclic gene expression in the periodic segmentation of somites*. *Genes & development*, 2005. **19**(10): p. 1156-1161.
106. Schröter, C. and A.C. Oates, *Segment number and axial identity in a segmentation clock period mutant*. *Current biology : CB*, 2010. **20**(14): p. 1254-1258.
107. Bajard, L., et al., *Wnt-regulated dynamics of positional information in zebrafish somitogenesis*. *Development*, 2014. **141**(6): p. 1381-91.
108. Dubrulle, J., M.J. McGrew, and O. Pourquie, *FGF signaling controls somite boundary position and regulates segmentation clock control of spatiotemporal Hox gene activation*. *Cell*, 2001. **106**(2): p. 219-232.
109. Dubrulle, J. and O. Pourquie, *fgf8 mRNA decay establishes a gradient that couples axial elongation to patterning in the vertebrate embryo*. *Nature*, 2004. **427**(6973): p. 419-422.

110. Sawada, A., et al., *Fgf/MAPK signalling is a crucial positional cue in somite boundary formation*. Development (Cambridge, England), 2001. **128**(23): p. 4873-4880.
111. Morimoto, M., et al., *The Mesp2 transcription factor establishes segmental borders by suppressing Notch activity*. Nature, 2005. **435**(7040): p. 354-359.
112. Rossant, J., et al., *Expression of a retinoic acid response element-hsplacZ transgene defines specific domains of transcriptional activity during mouse embryogenesis*. Genes Dev, 1991. **5**(8): p. 1333-44.
113. Shimozono, S., et al., *Visualization of an endogenous retinoic acid gradient across embryonic development*. Nature, 2013. **496**(7445): p. 363-6.
114. Diez del Corral, R., et al., *Opposing FGF and retinoid pathways control ventral neural pattern, neuronal differentiation, and segmentation during body axis extension*. Neuron, 2003. **40**(1): p. 65-79.
115. Moreno, T.A. and C. Kintner, *Regulation of segmental patterning by retinoic acid signaling during Xenopus somitogenesis*. Dev Cell, 2004. **6**(2): p. 205-18.
116. Vermot, J., et al., *Retinoic acid controls the bilateral symmetry of somite formation in the mouse embryo*. Science (New York, N.Y.), 2005. **308**(5721): p. 563-566.
117. Vermot, J. and O. Pourquie, *Retinoic acid coordinates somitogenesis and left-right patterning in vertebrate embryos*. Nature, 2005. **435**(7039): p. 215-20.
118. Bienz, M., *beta-Catenin: a pivot between cell adhesion and Wnt signalling*. Current biology : CB, 2005. **15**(2): p. R64-7.
119. MacDonald, B.T., K. Tamai, and X. He, *Wnt/beta-catenin signaling: components, mechanisms, and diseases*. Developmental cell, 2009. **17**(1): p. 9-26.
120. Niehrs, C., *On growth and form: a Cartesian coordinate system of Wnt and BMP signaling specifies bilaterian body axes*. Development, 2010. **137**(6): p. 845-57.
121. Aulehla, A., et al., *Wnt3a plays a major role in the segmentation clock controlling somitogenesis*. Dev Cell, 2003. **4**(3): p. 395-406.
122. Delfini, M.C., et al., *Control of the segmentation process by graded MAPK/ERK activation in the chick embryo*. Proc Natl Acad Sci U S A, 2005. **102**(32): p. 11343-8.
123. Oginuma, M., et al., *Mesp2 and Tbx6 cooperatively create periodic patterns coupled with the clock machinery during mouse somitogenesis*. Development, 2008. **135**(15): p. 2555-62.
124. Dequéant, M.-L., et al., *A Complex Oscillating Network of Signaling Genes Underlies the Mouse Segmentation Clock*. Science, 2006. **314**(5805): p. 1595-1598.
125. Hayashi, S., et al., *Sprouty4, an FGF inhibitor, displays cyclic gene expression under the control of the notch segmentation clock in the mouse PSM*. PloS one, 2009. **4**(5): p. e5603.
126. Ishikawa, A., et al., *Mouse Nkd1, a Wnt antagonist, exhibits oscillatory gene expression in the PSM under the control of Notch signaling*. Mechanisms of Development, 2004. **121**(12): p. 1443-1453.
127. Niwa, Y., et al., *The initiation and propagation of Hes7 oscillation are cooperatively regulated by Fgf and notch signaling in the somite segmentation clock*. Developmental cell, 2007. **13**(2): p. 298-304.
128. Niwa, Y., et al., *Different types of oscillations in Notch and Fgf signaling regulate the spatiotemporal periodicity of somitogenesis*. Genes & development, 2011. **25**(11): p. 1115-1120.
129. Dale, J.K., et al., *Oscillations of the snail genes in the presomitic mesoderm coordinate segmental patterning and morphogenesis in vertebrate somitogenesis*. Developmental cell, 2006. **10**(3): p. 355-366.
130. Hirata, H., et al., *Instability of Hes7 protein is crucial for the somite segmentation clock*. Nature genetics, 2004. **36**(7): p. 750-754.
131. Evrard, Y.A., et al., *lunatic fringe is an essential mediator of somite segmentation and patterning*. Nature, 1998. **394**(6691): p. 377-81.
132. Zhang, N. and T. Gridley, *Defects in somite formation in lunatic fringe-deficient mice*. Nature, 1998. **394**(6691): p. 374-377.

133. Voon, D.C., et al., *Use of mRNA- and protein-destabilizing elements to develop a highly responsive reporter system*. Nucleic acids research, 2005. **33**(3): p. e27-e27.
134. Soroldoni, D. and A.C. Oates, *Live transgenic reporters of the vertebrate embryo's Segmentation Clock*. Curr Opin Genet Dev, 2011. **21**(5): p. 600-5.
135. Masamizu, Y., et al., *Real-time imaging of the somite segmentation clock: revelation of unstable oscillators in the individual presomitic mesoderm cells*. Proceedings of the National Academy of Sciences of the United States of America, 2006. **103**(5): p. 1313-1318.
136. Li, X., et al., *Generation of destabilized green fluorescent protein as a transcription reporter*. J Biol Chem, 1998. **273**(52): p. 34970-5.
137. Sonnen, K.F., et al., *Modulation of Phase Shift between Wnt and Notch Signaling Oscillations Controls Mesoderm Segmentation*. Cell, 2018. **172**(5): p. 1079-1090 e12.
138. Hubaud, A., et al., *Excitable Dynamics and Yap-Dependent Mechanical Cues Drive the Segmentation Clock*. Cell, 2017. **171**(3): p. 668-682 e11.
139. Ozbudak, E.M. and J. Lewis, *Notch signalling synchronizes the zebrafish segmentation clock but is not needed to create somite boundaries*. PLoS Genet, 2008. **4**(2): p. e15.
140. Webb, A.B., et al., *Persistence, period and precision of autonomous cellular oscillators from the zebrafish segmentation clock*. eLife, 2016: p. 1-17.
141. Pikovsky, A., M. Rosenblum, and J.r. Kurths, *Synchronization : a universal concept in nonlinear sciences*. 2003, Cambridge: Cambridge University Press.
142. Galceran, J., et al., *LEF1-mediated regulation of Delta-like1 links Wnt and Notch signaling in somitogenesis*. Genes Dev, 2004. **18**(22): p. 2718-23.
143. Hofmann, M., et al., *WNT signaling, in synergy with T/TBX6, controls Notch signaling by regulating Dll1 expression in the presomitic mesoderm of mouse embryos*. Genes Dev, 2004. **18**(22): p. 2712-7.
144. Liedtke, D., I. Erhard, and M. Scharfl, *snail gene expression in the medaka, Oryzias latipes*. Gene Expr Patterns, 2011. **11**(3-4): p. 181-9.
145. Nagai, T., et al., *A variant of yellow fluorescent protein with fast and efficient maturation for cell-biological applications*. Nat Biotechnol, 2002. **20**(1): p. 87-90.
146. Coutelle, O., et al., *Hedgehog signalling is required for maintenance of myf5 and myoD expression and timely terminal differentiation in zebrafish adaxial myogenesis*. Developmental biology, 2001. **236**(1): p. 136-150.
147. Carvalho, L. and C.-P. Heisenberg, *The yolk syncytial layer in early zebrafish development*. Trends in cell biology, 2010. **20**(10): p. 586-592.
148. Carvalho, L., et al., *Control of convergent yolk syncytial layer nuclear movement in zebrafish*. Development (Cambridge, England), 2009. **136**(8): p. 1305-1315.
149. Blanco, M.J., et al., *Snail1a and Snail1b cooperate in the anterior migration of the axial mesendoderm in the zebrafish embryo*. Development, 2007. **134**(22): p. 4073-81.
150. Choi, H.M.T., et al., *Third-generation in situ hybridization chain reaction: multiplexed, quantitative, sensitive, versatile, robust*. Development, 2018. **145**(12).
151. Kurosawa, G., et al., *Temperature-amplitude coupling for stable biological rhythms at different temperatures*. PLoS computational biology, 2017. **13**(6): p. e1005501.
152. Ruby, N.F., D.E. Burns, and H.C. Heller, *Circadian rhythms in the suprachiasmatic nucleus are temperature-compensated and phase-shifted by heat pulses in vitro*. The Journal of neuroscience : the official journal of the Society for Neuroscience, 1999. **19**(19): p. 8630-8636.
153. Sfakianakis, D.G., I. Leris, and M. Kentouri, *Effect of developmental temperature on swimming performance of zebrafish (Danio rerio) juveniles*. Environmental Biology of Fishes, 2011. **90**(4): p. 421-427.
154. Sfakianakis, D.G., et al., *The effect of rearing temperature on body shape and meristic characters in zebrafish (Danio rerio) juveniles*. Environmental Biology of Fishes, 2011. **92**(2): p. 197-205.

155. Kidd, P.B., M.W. Young, and E.D. Siggia, *Temperature compensation and temperature sensation in the circadian clock*. Proc Natl Acad Sci U S A, 2015. **112**(46): p. E6284-92.
156. Isojima, Y., et al., *CKlepsilon/delta-dependent phosphorylation is a temperature-insensitive, period-determining process in the mammalian circadian clock*. Proceedings of the National Academy of Sciences of the United States of America, 2009. **106**(37): p. 15744-15749.
157. Gajewski, M., et al., *Anterior and posterior waves of cyclic her1 gene expression are differentially regulated in the presomitic mesoderm of zebrafish*. Development (Cambridge, England), 2003. **130**(18): p. 4269-4278.
158. Koyano-Nakagawa, N., et al., *Hes6 acts in a positive feedback loop with the neurogenins to promote neuronal differentiation*. Development (Cambridge, England), 2000. **127**(19): p. 4203-4216.
159. Sonnen, K.F. and A. Aulehla, *Dynamic signal encoding--from cells to organisms*. Semin Cell Dev Biol, 2014. **34**: p. 91-8.
160. Huppert, S.S., et al., *Embryonic lethality in mice homozygous for a processing-deficient allele of Notch1*. Nature, 2000. **405**(6789): p. 966-970.
161. Naruse, K., et al., *Medaka genomics: a bridge between mutant phenotype and gene function*. Mechanisms of Development, 2004. **121**(7-8): p. 619-628.
162. Johnston, I., V. Vieira, and M. Abercromby, *Temperature and myogenesis in embryos of the Atlantic herring Clupea harengus*. The Journal of experimental biology, 1995. **198**(Pt 6): p. 1389-1403.
163. Jinek, M., et al., *A programmable dual-RNA-guided DNA endonuclease in adaptive bacterial immunity*. Science, 2012. **337**(6096): p. 816-21.
164. Hsu, P.D., et al., *DNA targeting specificity of RNA-guided Cas9 nucleases*. Nat Biotechnol, 2013. **31**(9): p. 827-32.
165. Stemmer, M., et al., *CCTop: An Intuitive, Flexible and Reliable CRISPR/Cas9 Target Prediction Tool*. PLoS One, 2015. **10**(4): p. e0124633.
166. Hwang, W.Y., et al., *Efficient genome editing in zebrafish using a CRISPR-Cas system*. Nat Biotechnol, 2013. **31**(3): p. 227-9.
167. Kirchmaier, S., K. Lust, and J. Wittbrodt, *Golden GATEway cloning--a combinatorial approach to generate fusion and recombination constructs*. PloS one, 2013. **8**(10): p. e76117.
168. Porazinski, S.R., H. Wang, and M. Furutani-Seiki, *Dechoriation of medaka embryos and cell transplantation for the generation of chimeras*. J Vis Exp, 2010(46).
169. Sakata-Haga, H., et al., *A rapid and nondestructive protocol for whole-mount bone staining of small fish and Xenopus*. Sci Rep, 2018. **8**(1): p. 7453.